Vanadium Oxide Anions Clusters: Their Abundances, Structures and Reactions with SO_2

A Thesis
Presented to
The Academic Faculty

by

Richard B. Wyrwas, Jr.

In Partial Fulfillment
of the Requirements for the Degree
Doctor of Philosophy in Chemistry

Georgia Institute of Technology
November 2004

Vanadium Oxide Anion Clusters: Their Abundances, Structures, and Reaction with SO_2

Approved:

Robert L. Whetten, Chairman
School of Chemistry

Mostafa A. El-Sayed
School of Chemistry

Paul H. Wine
School of Chemistry

C. David Sherrill
School of Chemistry

Phillip N. First
School of Physics

Approval Date: November 10, 2004

DEDICATED TO THE MEMORY OF

ALVERDA MARIE WYRWAS

ACKNOWLEDGEMENT

I now find myself now at the end of a part of a great journey that started so many years ago when I was five years old. I only have a few fragments of memories of that first day I left home to go to school. The days between my first, and my approaching last day of school have been filled with nearly all of my memories. Alone I wouldn't have been able to do all I set out to do, nor would it have been the same if everything came easily. Now, I would like to take a few moments and thank those who have helped make this possible.

I would like to thank my thesis committee for their time they took to read my thesis and meet with me on important matters. I would especially like to thank Phil First. In my first years as a graduate student Prof. First was my co-advisor and taught me a great deal about STM and vacuum technology. Phil, it has been great! There are so many fond memories from "First Lab" that I will carry with me forever and some I would love to forget quickly - but won't.

Certainly, I do not think any of this would have been possible with out my advisor Rob Whetten. He not only gave me the 'scientific independence' to explore my own ideas, but he encouraged them. I will say you have made me think every inch of the way, if not about science then about every other thing from my work ethic in lab to the price of coffee beans. I have learned so much from you in the past few years, I couldn't even

begin to put it all down now. You taught me coffee is a must; and Burritos can be eaten with your hands and a fork simultaneously. You have given all of me some great one-liners and a new outlook on life as a whole. You have listened to my outlandish ideas and my awful, sometimes pointless, stories, laughed at and encouraged my horrible jokes, and just put up with me for the past couple of years…and I thank you.

I would like to thank my parents for bringing me into this world, of course. But I know that I would have failed long, long ago if it weren't for my dad. Without him, I may be the manager of a Western Pennsylvanian gas station today. He never let me quit anything until it was over. No matter how much I protested I learned to see something through to the end. He taught me it gets tough and that is *why* I do it. It's also the same reason why not many others do. With this attitude toward things, I have found that it *does* get tough and nearly impossible, but give it time and push on and it will get better.

Although I may have never considered graduate school, I think college was always part of my plan for the future when I was young. My dad played a big part in all of that and when it was time to go he came through for me. And I went. And here I am. So, dad this one's for you.

My brother, Rock, and my sister, Erica, have also been a part of my college experience and my life. I can't think of what things would be like with out you two. Just when you think nothing bad will happen - it happens to us. We have been though floods, break-downs, fights, break ins, fits, break outs, and plenty of laughs. Thanks for being there when I needed someone to blabber with on my rides home or when I needed reminded of the odds *we* overcame and what *we* have accomplished.

I could continue with family for the *next* 200 pages, so I will stop here. I do want to thank Chris and Shanae who have been great to have around. My uncle Ray, all my cousins in South Carolina, the US Army, and Pennsylvania, including the Conrads- Thanks for all you have done to help me along the way as well as your words of encouragement.

I would like to thank my "sixth committee member" Professor Andrew Leavitt. I met Andy a few years ago when he worked in our lab as a visiting professor from the State University of West Georgia. He is always up for coffee and quick with the jokes. I will come up with an *appropriate* nick-name for you yet, but for now just cherish the memories of the machine shop at 7AM and the hours that followed that neither of us will ever get back!

I had a chance to read back through some of the acknowledgements written by other Whetten group members and they all include a similar theme when it comes to the Whetten group: coffee, burritos(or 'cubans'), beers, and notes on napkins. I must concur. I think this group would not function adequately, if at all, with out coffee. It would sound like a bad rough pump! I have seen it happen to those who have finished before me and it will surely continue, but coffee is the life force that gets you out of here during those final months! Burritos (or currently 'Taco Tuesdays') are the fuel, and who needs a white-board when there are plenty of napkins around. No matter what kind of day it is - good or not so good, a beer is the best way to end it! Best of luck to the Whetten lab members past, present and future, and thanks for all the things everyone has done to help me do things I have done.

TABLE OF CONTENTS

LIST OF FIGURES

LIST OF TABLES

CHAPTER I

INTRODUCTION

1.1 Introduction.

Transition-metal and transition-metal-oxide clusters have received much attention due to their catalytic nature.[1-4] The usefulness of specific compounds is most often attained due to their size, electronic structure, and geometry and has attracted many researchers to a new frontier in catalysis and nanoscience. The study of the gas-surface interactions has been of particular interest to many scientists for practical and fundamental reasons.[1]

Certain transition-metal oxides have received much attention due to their usefulness both as catalysts and catalytic supports. Their use as cost effective catalyst in oxidation-reduction processes has been widely studied.[3] Understanding the role a transition metal oxide plays has been the goal of many researchers. Understanding the specific qualities a certain metal provides a catalytic system may help researchers design catalysts that are more efficient and selective.

Vanadium oxide has gained much attention as a catalyst over the past few years. The low oxidation potential of the vanadium atom, as well as the ability to easily adapt its

bonding structure, give the metal unique catalytic properties. The most common starting form used is vanadium pentoxide, V_2O_5. In this form, the vanadium is maximally oxidized in its +5 oxidation state. The metal can also exist in a +4 oxidation state as VO_2 or in the +3 or +2 states as V_2O_3 or VO. An interesting series of mixed valent compounds, V_nO_{2n-1}, lie between the V_2O_3 (n=2) and VO_2 ($n \rightarrow \infty$) composition. Most commonly it prepared found as V_2O_5, VO_2 or V_2O_3.

As a catalyst, V_2O_5 has been used in unsupported and supported forms. Its use in sulfur dioxide oxidation has been widely studied[5-8] and well known[2,3]. The catalytic oxidation of SO_2 to SO_3 is a key step in the production of sulfuric acid, as shown here:

$$SO_2 + O_2 \rightarrow SO_3 \ (+ H_2O \rightarrow H_2SO_4)$$

Sulfuric acid is the most abundant industrially produced compound each year.[9] The cost effective V_2O_5-based catalyst has replaced platinum based catalysts. Optimal production of SO_3 is achieved at elevated temperature, with maximum efficiency achieved near 600K in a layered reactor. However, industrial reactors are usually operated at higher temperatures (700-870 K), which extends the life of the catalyst. The actual mechanism for catalysis been determined to involve two cycles: the oxidation of SO_2 to SO_3 and the re-oxidation of the vanadium catalyst. On the molecular level, several attempts have been made to explain the process and identify critical steps. However, the topic is not without debate.[10,11] Based on the discussions found in the literature,[2,3,5-8,10-13] the following catalytic cycle has been illustrated to help discuss the process:

The process begins with two proximal vanadium atoms in the +5 oxidation state. In the first step SO_2 adsorption yields the sulfito-complex, when the SO_2 molecule is inserted into the V-O-V bridged oxygen. As shown below, this process is quite

favorable. It is at this point that elevated temperatures may assist in transfer of a oxide bridge; this has been designated as an auto-redox step. The oxide vacancy now puts the vanadium atoms into a +4 oxidation state and the sulfur is +6 in the sulfato-complex, which desorbs the SO_2. The addition of an oxygen molecule, at the vacancy yields a (very reactive) peroxo group. The peroxo group can react freely and quickly with a second SO_2 to form sulfate, which releases the second SO_3 and the cycle is complete.

A principle objective of this dissertation research is to explore each the step in Figure 1-1. Measurements have be made on individual clusters and their interactions with SO_2. Further theoretical studies using density functional methods have been performed to verify discrete cluster complexes.

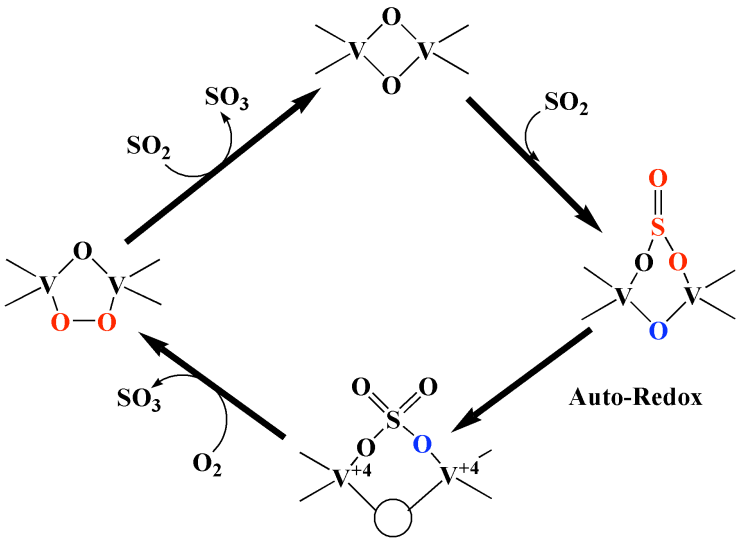

Figure 1-1. Catalytic cycle of SO_2 oxidation.

The use of clusters to model surface interaction such as those just described has been a useful activity.[1,14-16] The ability to model molecule-surface interaction with clusters opens many new avenues of approach to study this phenomena. One such

avenue is the use of theoretical techniques to guide surface studies. Witko and co-workers first employed this avenue to model surface structures and the effect on catalytic behavior of vanadium oxides.[17] As the study of cluster chemistry and surface science grow together, it has become apparent that the geometric and electronic structures play distinct roles in the systems that are being studied.[18]

Castleman and co-workers have contributed a great deal of research toward the understanding of the catalytic behavior of group-V metal oxides, mainly vanadium oxides, toward organic molecules. First, the structure and formation of the cluster of vanadium oxide, niobium oxide and tantalum oxide were studied via collision induced dissociation (CID). It was found that the anionic clusters preferentially yielded a MO_3^- fragment and neutral fragments as MO_2, MO_3 and M_2O_5. The cation clusters favored the same neutral products but MO_2^+ and $M_3O_7^+$. Reactions with hydrocarbon molecules, such as ethane and ethylene, resulted in oxygen-transfer reactions.[18-20] The actions have been characterized by cluster size, charge, and composition.[18] However, they found a lack of reactivity for the anionic clusters in their experiments.

Early experiments by Rudnyi and co-workers[21] on the equilibrium vapor of V_2O_5 showed stable formation of anions of vanadium oxide of clusters up to $V_4O_{10}^-$. These anion clusters of vanadium oxide have been shown to be reactive toward certain molecules. Dinca et al.[22] has shown that the anion clusters interact with organic esters and reactivity decreases rapidly as the clusters size increases.

Neutral vanadium oxide clusters in the +4 and +5 oxidation state are more difficult to study, because their ionization potential is very high. Ionization of these clusters is not accomplished with out risk of destroying the cluster. Advances in

ionization techniques via frequency mixing to yield high energy photons for ionization, have given investigators the tools to study such neutral clusters.[23] Foltin and co-workers[23] studied the growth dynamics of these clusters in a laser vaporization source found the laser fluence played a distinct role in the composition.

More fundamental methods of research have been employed to study the basic properties of these materials.[24-27] Photoelectron spectroscopy performed by L.S. Wang and co-workers has shown an increasing electron affinity for the anion molecules of vanadium oxide as the number of oxygen atoms in the molecule is increased. The interactions of single vanadium atoms with oxygen have been shown to occur at low temperature to form simple mono-vanadium oxide compounds.[28]

In the solution phase, vanadium oxides can condense to form large polyanionic clusters known as Polyoxometallates (POMs). POMs have a been found to have many useful chemical and catalytic properties.[29] Homogeneous POMs containing vanadium have been identified, but more interesting is heterogeneous POMs that contain vanadium atoms have been found to have unique properties that are attributed to the vanadium atom. POMs have been employed in many catalytic processes, mostly as redox catalysts and as polyacids.[29-32] POMs have been shown to form spontaneously in solution and be sensitive to pH.[33,34] Polyanionic clusters of vanadium oxide, $V \leq 16$, can be formed that have very versatile redox properties.[30] Highly ordered symmetric structures have been determined in many studies. For example, a ring structure was derived from a single crystal of $V_3O_9^{3-}$,[35] as well as a closed cage for $V_5O_{14}^{3-}$.[36] Also larger polyanions have been isolated including $V_4O_{12}^{4-}$ and $V_{12}O_{32}^{4-}$.[37,38]

The recent reports by Vyboischikov and Sauer, predict that the V_2O_5 composition will yield highly cohesive structures in the form of high symmetry cages.[39,40] An earlier report by the same authors dealt with the smaller cluster anions and neutral equivalents, $V \leq 4$.[40] The geometric structures were calculated along with electronic affinities. In comparison to experimental electron affinities determined by photoelectron spectroscopy,[24,25] the calculations are in agreement. Aside from other details of structure, formation and electronic stability, the work demonstrated only slight geometric variances between the anionic and neutral species. Even at low nuclearity, $V_3O_8^-$ and V_3O_8 form closed ring structures. Overall, the resulting calculations corresponded well to the experimental data available on the species calculated. The theoretical approach, B3LYP with a TZV(P) basis set, was found to be a reliable method to use for computations on this metal oxide system.

From the research discussed above some important questions remain unanswered pertaining to vanadium oxide clusters. Larger $(V_2O_5)_n$ clusters (n = 4 to 12) form closed-cage structures that have extremely high cohesion, analogous to the well known carbon-fullerenes or metal-carbide clusters. Can the predicted high cohesion & coalescence-resistance be verified? How inert are they interact in ordinary atmospheres that contain O_2, H_2O and so on? Can any observed reactivity patterns be explained? What approach will succeed in isolating them in macroscopic quantities?

1.2 Scope of this thesis.

The primary method of the work presented here is to probe clusters systems using high-pressure flow reactor techniques. The pulsed inert-gas flow reactor and time-of-

flight mass spectrometer discussed in Chapter II have great advantages and a broad applicability. As a pulsed flow-reactor, the amount of material consumed is low. Each gas pulse is only a fraction of what would be used in a continuous flow system.[41] The interaction between the clusters produced and the reactant gas occurs on a very short timescale, <200 μs, but the total pressure achieved in the flow reactor and partial pressure of the reactant gas is much higher. Thus, the short time scale in combination with the high partial pressure of reactants gives measurable reactions. The flow reactor pressures can be increased to nearly 400 mbar, which is comparable to atmospheric pressure in the upper atmosphere.[42] However, this experimental apparatus is not limited to chemical reactivities of atmospheric relevance. Physical techniques such as photoelectron detachment and surface-collision dissociation can be employed to gain structural and electronic information about the systems studied as well. With the uncanny ability of the source to produce high yields of both negative and positive charge as well as neutral clusters, a long list of possible systems can be studied.

Three main cluster systems are presented. The majority of the work reported here concerns vanadium oxide cluster anions. Chapter III discusses the production of the vanadium oxide anion cluster system. The ability to control the oxidation state of the clusters has proven to be essential. (Pure vanadium clusters anion have proved to be very difficult to produce in the system, but completely oxidized clusters have been remarkably easy to produce.) In Chapter IV, the reactions of vanadium oxide anions with SO_2 and O_2 are studied over a range of conditions. The relationship of the average oxidation state and the reactivity of the cluster is made as well as the relation of reactivity to size. The experiments in Chapter IV lead to the studies discussed in Chapter V. Monovanadium

oxide complexes discussed in Chapter V were small enough to model by quantum-chemical calculations, and thereby produced some wonderful insights into the nature of the chemical interactions that are described in Chapter IV.

The studies described in Chapter VI involving carbon cluster anions and the interactions with SO_2 proved to be some of the most challenging work to interpret. Mass coincidence products in the mass spectrum hindered the assignment of the processes involved. After careful analysis of the natural isotope abundances, and significantly enhancing resolution capabilities of the mass spectrometer, the results were made clear and quite interesting. A final set of experiments that are still in progress and briefly discussed in Chapter VII, describe the interactions of sodium chloride clusters with atmospheric gases such as H_2O and SO_2. The sodium chloride system has been highly studied in surface science and in atmospheric chemistry.

Finally, Part II of this thesis incorporates early work on the electronic structure of small metal nanoparticles. Chapter VIII deals with low energy transitions that can be observed in metal nanoparticles. Until recent improvement in experimental techniques these low lying transitions were undetectable. Since the emergence of more advanced techniques and improved detection methods, the long predicted transitions are now observable. The final chapter discussed some ideal contributions to the study of encapsulated nanocrystals. Chapter IX gives a brief overview of a study that involved imagining of immobilized gold thiol nanoparticle systems.

CHAPTER II

INSTRUMENTATION AND TECHNIQUES

2.1 Introduction.

The use of a pulsed-laser ablation cluster source has proven to be an effective way to produce and study gas-phase cluster species.[4,43-47] This technique is not the only method to produce gas phase clusters; other clusters can also be produced by electronic arc, laser desorption, or sputtering techniques.[48] The ideas behind all these techniques are a "top-down" approach. This would involve starting with a bulk piece of material or one component and physically breaking it down into simple clusters. Ideally, any material would be able to produce clusters, but this approach is limited as not all clusters can be readily produced from this method.

This technique does have many benefits. It is, in fact, applicable to a wide range of materials and changing the source to another to produce another cluster system can be done quickly and easily. The versatility of source in reality is limited by other factors: (1) The ability of the material itself to be efficiently ablated and form simple clusters. (2) Even more fundamental is the shape of the target material. In the design discussed in section 2.2, the ablation target must be a rod with a diameter of about 0.125" (3mm). The

overall length of the rod must be at least 1”(25mm). If the target rod is a metal, a rod of ample length and purity may be readily available from most chemical supply companies. For those metals that are not it may be possible to machine a material into the specified dimensions. Other soft metals, such as sodium or potassium are not ideal for machining, and more clever techniques can be employed to create a target. In some cases, target materials may only be sold as fine powders. The powder can be pressed in a mold to form a target rod. Most often, this is not trivial and may be impossible, however modifications can be made.

Beyond the limitations of the target rod are the timings of the gas pulse and laser pulse - this will be discussed in more detail in section 2.2. The arrival of the buffer in relation to the arrival of the laser pulse is critical. Also the laser fluence and size of the buffer gas pulse is significant as well. With a given target material, effective experimental settings can be found to produce clusters that include laser fluence, an optimal gas pulse, and time synchronization in relation to each.

During the laser ablation of the target rod, the atoms are not only separated from each other but may be separated from their electrons as well. In the region, a type of plasma is formed that consists of atoms of a variety charges. This range of charge states is preserved after cluster formation resulting in charged clusters. The clusters are positive, negative and neutral. If one is interested in studying the charged clusters, mass spectrometry is a convenient and common the method used to detect and characterize clusters. Various types of mass spectrometry have emerged, each unique in its own way. Time-of-Flight mass spectrometry (TOF-MS) provides ample resolution and the ability to capture an entire mass range simultaneously. This way each gas pulse of clusters often

referred to as a *shot* can be recorded. The mass spectrum is collected as an average signal recorded for a given number of shots. The time-of-flight mass spectrometry is discussed in more detail in section 2.3.

2.2 Pulsed He Flow Reactor.

The pulsed helium flow reactor and acceleration region of the time-of-flight mass spectrometer is mounted inside a 1-foot cubic vacuum chamber that is pumped by an 8" turbo molecular pump, Pfeiffer-Balzers TPU-520 (pump speed 520 l/s). Under static conditions, the base pressure of the chamber is about 4 x 10^{-7} torr (5x10^{-10} bar). Under experimental conditions the chamber operates at a time-averaged pressure between 1.0 x 10^{-5} to 6.0 x 10^{-5} torr (1.33 x10^{-8} to 8 x10^{-7} bar).

2.2.1 Source Region.

The vaporization block, Figure 2-1 (B), is made from stainless steel. It contains the sample or target rod that is less than 0.125" in diameter. The target rod is inserted though a 0.125" diameter channel and is perpendicular to a 1mm channel though which a laser pulse is focused. Above the target rod is pulsed gas valve, General Valve Series 9, is attached. The valve delivers a gas pulse through a 2mm channel, which is orthogonal to both the laser channel and target rod. The gas channel is also offset to allow the gas pulse to flow along the surface of the target rod and into a larger 3mm channel. The vaporization block is attached to what has become known as the expansion piece, which is a 2mm in diameter channel, 0.5" in length that connects the vaporization block to the flow tube reactor.

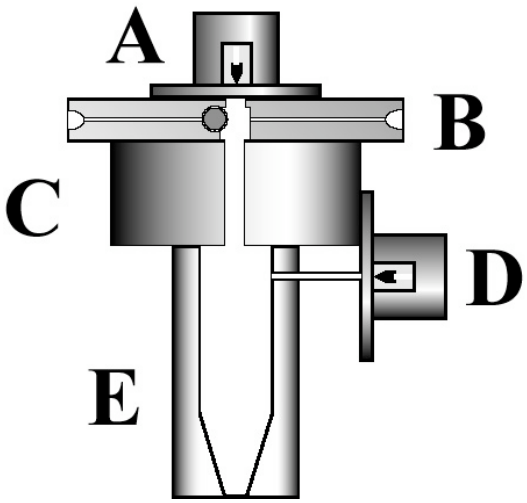

Figure 2-1. Pulsed He cluster source with flow reactor. A) The primary pulsed-gas valve, in which room-temperature He is normally used a buffer gas, here seeded with a known amount of oxygen. (B) The vaporization block and vaporization region, in which the vanadium oxide clusters are formed by laser ablation of a vanadium rod in the presence of O_2 and cooled in a He flow-stream provided by (A). (C) The thermalization region. (D) The secondary pulsed-gas valve, where room-temperature reactant: He mixtures can be added into (E) a 2.5 cm reaction region.

Using a motor and a rotary feed through, the target rod is rotated and translated using a setscrew, (1/4-80). This continually provides a fresh surface for laser ablation and prevents complete non-uniform wear of the rod. Using a Stanford delay generator (Stanford Research Systems DG535), the gas pulse delivered from the pulsed valve is synchronized to arrive at the target at the same time as the laser pulse. During an experiment the timing of the laser in relation to the gas pulse can be changed to find the ideal conditions for producing clusters. Predicting the delay timings based on mechanical and electronic delays within the instruments used is not an entirely accurate approach to determine ideal timings for cluster production. Fine tuning of the delay timings is performed routinely. This is discussed in more detail in section 2.2.3.

The gas delivered from the valve is usually an inert gas such as helium. Other inert gases like nitrogen, argon or neon can be used, but cluster growth in some systems favors the use of helium for several reasons. The laser pulse provides the energy to the ablated surface atoms. The gas pulse acts as a buffer gas that is used to remove the heat-of-formation by the newly clusters. The lighter helium atoms more efficient at transporting this excess heat. This increased efficiency of helium to remove this heat is valuable in some clusters systems to aid cluster growth. The gas also acts as a carrier gas to direct the entrained clusters though the series of channels to the flow reactor and then to the mass spectrometer.

The expansion of the gas channel in the source from 2mm before the target rod to 3mm just after the target rod assists in the cooling of the growing clusters by an adiabatic expansion of the gas. This 3mm channel has been referred to by some in literature as the "waiting room."[48,49] It is in this region that all cluster growth is completed. Once the clusters enter the 2mm channel of the expansion piece, cluster growth is terminated and the temperature of the buffer gas and clusters is equilibrated to the wall of the channel. The reference to this piece being the "expansion piece," although the actual channel is of uniform diameter and no expansion occurs. This can probably be traced back to earlier versions of this experiment. In variations of this design,[49] the channel through the expansion region can be conical in shape and diverge to diameter of the flow tube reactor. The gas pulse and clusters exit the expansion region directly into the flow tube reactor. The *expansion piece* in all reality is the *thermalization region*.

2.2.2 The Flow Tube Reactor.

The flow tube reactor (FTR), Figure 2-1 (D), is the region in which reactant gases are added to the clusters. In this region the cluster pulse is overlapped with a second gas pulse - typically the FTR is 1-1.5" (25 to 40 mm) long. The top portion has a diameter of 4-6 mm with an exit hole of 2-3mm. The walls inside the reactor are tapered starting roughly at 0.3" from the exit of the reactor. The dimensions of the FTR can be varied to change reaction time and reaction pressure. A more detailed discussion of the FTR is discussed in section 2.3.3. Heating and cooling devices are appended to raise and lower the temperature of the flow tube.

2.2.3 Pressure and Dynamics.

The pulsed gas valves are designed to deliver a uniform gas pulse. The length or duration of the pulse can be controlled by the control electronics in 1 μs increments. Normally, a 1 μs increment is not a notable increment. Increments of 5-10 μs provide notable changes in the experiment.

Without a fast internal pressure gauge,[50] the instantaneous pressure inside the vaporization source and the flow tube reactor (FTR) cannot be precisely measured. In turn, the partial pressures of reactant gases are indeterminable as well. The total pressure and partial pressures can only be calculated. We have measured that the gas valve, under typical operating conditions at a repetition rate of 7 Hz and raising the chamber pressure 3.0×10^{-5} torr, delivers 0.2 scc (at STP) of gas per pulse. An upper bound on the total pressure in the FTR can be estimated by equation 1.1:

$$P_{total} \leq P_{Stag} \frac{V_{displaced}}{V_{reactor}} \quad (2.1)$$

Where P_{stag} is the pressure of gas behind the valve, $V_{displaced}$ is volume of the gas pulse delivered, 30 mm^3 at STP, and $V_{reactor}$ is the volume of the FTR. The stagnation pressure of the main gas valve is 100 psig (7 bar) and 20-40 psig for the reaction valve. Three reactors are used: A 1" stainless steel reactor, 1" brass reactor, and a 1.5" brass reactor all having different dimensions. A 1"stainless steel reactor is 1 inch in length with a 6mm channel in diameter that tapers to an exit hole of 3mm in diameter. The volume has been measured to be 0.700 cc. A 1" brass reactor also measuring 1 inch in length has a 4mm channel that tapers to a 2mm exit hole. The volume has been determined to be 0.400cc. The 1.5" brass reactor is the same as the 1"brass reactor, but with a length of 1.5 inches. The volume has been determined to be 0.560cc. Equation 2.1 estimates the pressure as though the reactor is sealed and the gas is injected completely into the reactor. In essence, this is calculation an upper limit of the pressure. Table 1 provides a summary of the FTRs, geometries and calculated pressure.

Table 2-1. Flow tube reactor types.

Reactor	Length (mm)	Channel Diameter (mm)	Exit Diameter (mm)	Pressure (mbar)
1" Stainless Steel	25.4	6	3	219
1" Brass	25.4	4	2	383
1.5" Brass	43.3	4	2	274

For simplicity, the determination of the total pressure neglects gas flow dynamics. It can be easily argued that the gas is flowing out of the reactor as gas is flowing into the reactor, but at a slower rate as the exit hole is smaller than the entrance aperture. One point that should be made about estimating the pressure in this way is the error involved. The difference between the calculated pressure from equation 1.1 and the actual pressure may be different for each reactor. It may be argued that the error in the pressure may scale with the ratio of entrance to exit hole diameter, in which case the difference in actual pressure and calculated pressure would be the same for each reactor. With out an accurate method of measuring the pressure of the reactor, the actual pressure can not be determined.

The brass reactors have an entrance opening of 4mm in diameter with a 2mm diameter exit. The stainless steel reactor has a 6mm entrance with a 3mm exit. The main difference in the reactors, other than the volume, is the exit hole. The rate at which the gas exits the reactor for the 2mm hole will be 2/3 slower than the 3mm hole. Not only does this change the residence time of the clusters, but it also changes the total pressure. There will be less error in the total pressure calculation from equation 1.1 for the reactors with the 2mm exit hole than the reactor with the 3mm exit. This only makes sense since these reactors are more like the sealed reactor model used to calculate the total pressure.

The partial pressure of the reactant gas is simply the mole fraction of the total gas pressure:

$$P_{react} = \chi_{reactant} P_{total} \tag{2.2}$$

Where χ is the mole-fraction of the reactant mixture and calculated as follows:

$$\chi = (\%\ \text{of Reactant added down stream}) \left(\frac{\Delta \bar{P}_{chamber}}{\bar{P}_{chamber}} \right) \left(\frac{\tau_{main}}{\tau_{reaction}} \right) \qquad (2.3)$$

In equation 2.3, the percentage of the reactant gas in the mixture downstream is used in relation to the ratio of the change in average chamber pressure and the gas pulse widths from the main and reactant valves. The ratio of τ_{main} to $\tau_{reactant}$ is roughly 0.2. From this it can be determined how much reactant gas is added down stream and therefore an estimate of its partial pressure in the flow tube reactor can be made.

2.2.4. Timings.

As stated above the inherent delay of the system electronics for the pulsed valve and the laser must be taken into consideration. In order to compensate, a delay pulse generator is used (Stanford Research Systems Model DG 535).

Aside from an electrical delay, there is also a mechanical delay in the pulsed valve. The time it takes for the valve to mechanically open is an issue as well. In order to estimate how long a delay elapses, the use of a fast ionization gauge (Beam Dynamics, Inc.) to measure the intensity of the pulse at a given location. This location was chosen to be the region between the exit of the FTR and the mass spectrometer.

The Continuum Nd:YAG laser used has a delay of about 300 μs. This takes into account a charge-fire sequence for each laser pulse. Figure 2-2 shows a timing sequence using a Nd:YAG laser as the ablation laser.

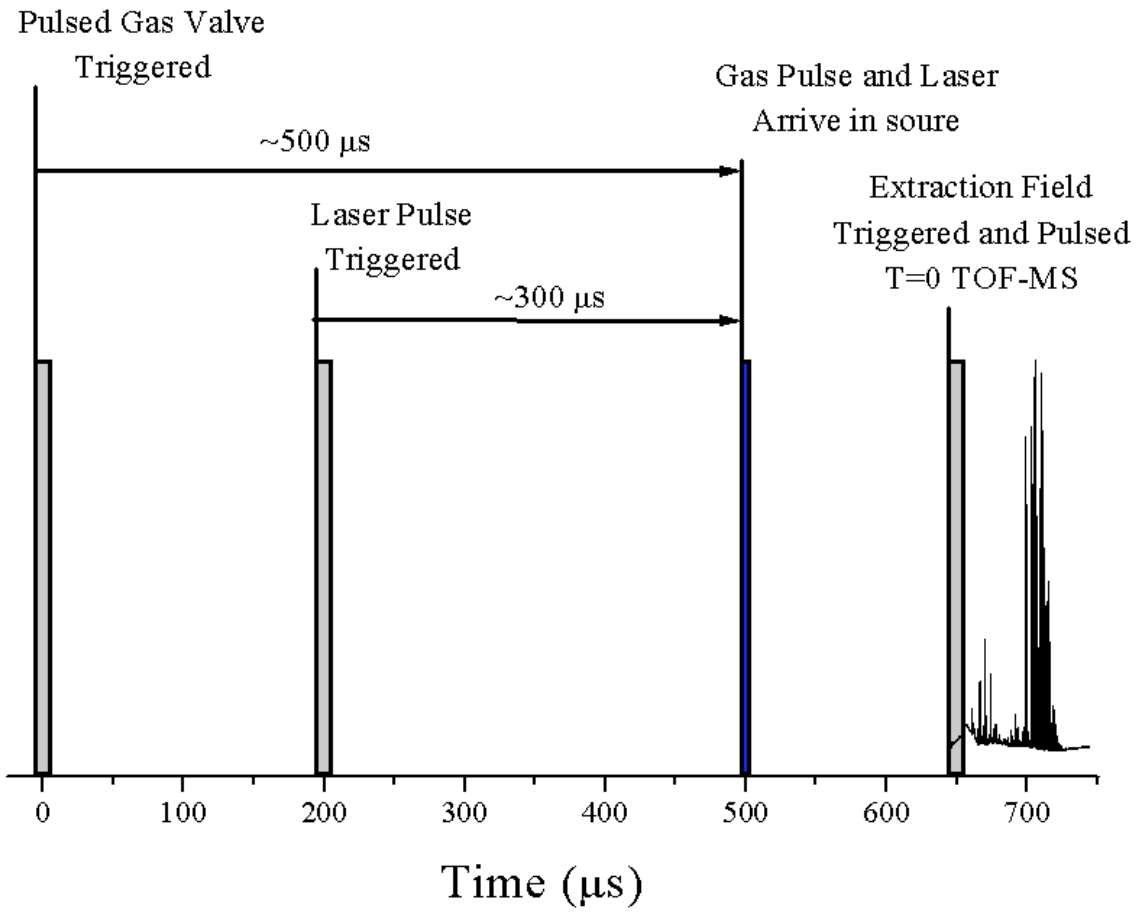

Figure 2-2. Timing sequence for pulsed helium flow reactor and time of flight mass spectrometer. Electronic and mechanical delays within the pulsed valve and Nd:YAG laser requires a pre-trigger for each in order to synchronize the two pulses. A delay generator delivers a TTL pulse as signified by the gray peaks. The first triggering pulse, at t = 0, triggers the pulsed gas valve. There is roughly a 500 μs delay within the electronics and valve mechanism before the gas pulse is delivered. The second TTL pulse triggers the Nd:YAG laser that has a 300 μs electronic delay. The gas pulse from the gas valve and laser pulse arrive simultaneously in the source region at the target rod. From that point, signified by the blue peak, the clusters move in to the extraction region of the mass spectrometer. There is only a 70 ns delay for the fast high voltage switch. The TTL pulse that triggers the high voltage pulse, also is used for the T_0 for the time-of-flight mass spectrometer. A raw mass spectrum is displayed at the end of the timing sequence.

Electronic and mechanical delays within the pulsed valve and Nd:YAG laser requires a pre-trigger for each in order to synchronize the two pulses. A delay generator delivers a TTL pulse as signified by the gray peaks. The first triggering pulse, at t = 0, triggers the pulsed gas valve. There is roughly a 500 μs delay with in the electronics and valve mechanism before the gas pulse is delivered. The second TTL pulse triggers the Nd:YAG laser that has a 300 μs electronic delay. The gas pulse from the gas valve and laser pulse arrive simultaneously in the source region at the target rod. From that point, signified by the blue peak, the clusters move in to the extraction region of the mass spectrometer. There is only a 70 ns delay for the fast high voltage switch. The TTL pulse that triggers the high voltage pulse, is also used as the T_0 for the time-of-flight mass spectrometer. A raw mass spectrum is displayed at the end of the timing sequence.

2.2.5. Instrumental Design Modifications.

The outer diameter of the thermalization region requires a narrow capillary tube from the secondary gas valve to the flow tube reactor to deliver the gas pulse. This causes the reaction gas pulse to be long in time and small in amplitude. Reducing the diameter of the thermalization region, allow the gas valve to be attached directly to the flow tube reactor. Figure 2-3 shows a flow reactor with a reduced thermalization region.

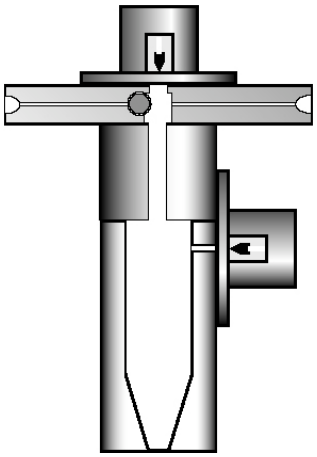

Figure 2-3. Pulsed flow tube reactor with a modified thermalization region.

2.3 Time-of-Flight Mass Spectrometer.

A schematic showing the time-of-flight mass spectrometer mounted inside two vacuum chambers is shown in Figure 2-4. The vacuum chambers are designated as the source chamber and detection chamber. The source chamber contains the pulsed source, the ion extraction region, and an ion deflecting plate. The pressure in the source chamber reaches 5 $x10^{-7}$ torr. The detection chamber contains the micro channel plate detector and a set of two stage reflecting plates. The vacuum level of the detection chamber can reach as low as $5x10^{-10}$ torr when the gate valve between the chambers is closed. When the gate valve is open, the pressure is typically ~5 $x10^{-8}$ torr. With the gas valves in the main chamber pulsing, the pressure in the detection chamber will spike with each gas pulse. In order to minimize the amount of gas that scatters between the chambers, a custom-made aluminum gasket was designed. The gasket has a standard outer diameter of 1.9" and a much smaller inner diameter of 0.5". This restriction does not inhibit the flight path of

the ions during their flight to the detector. The electrical feed-throughs are standard MHV and SHV feed-throughs.

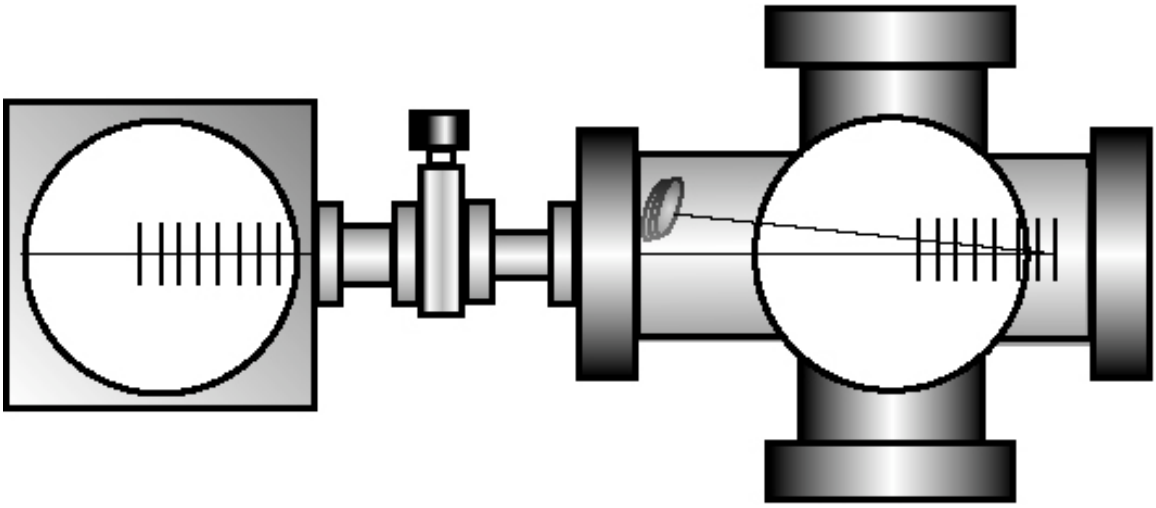

Figure 2-4. Time-of-flight mass spectrometer separated between two differentially pumped vacuum chambers.

2.3.1 Ion Extraction Region.

The ion extraction region of the time-of-flight mass spectrometer is a pulsed two-stage extraction region.[51] The ions are extracted orthogonal to the direction which they exit the FTR. The high voltage pulse is normally set to ≤ ±5kV and provided by a fast high voltage switch (Behlke HTS 81). The size of the high voltage pulse is determined based on the mass range of the cluster ions.

Before the ions beams are measured in the mass spectrometer, a skimmer collimates the pulse of clusters by removing the outer edges of the beam. The skimmer is located between the exit of the FTR and the extraction region and is attached directly to

the extraction plate apparatus. The skimmer is nothing more than two plates mounted at 30º with a narrow distance between them that ultimately defines the beam width. The width of the beam can be adjusted to allow more or less clusters to make it to the mass spectrometer. A narrow beam width will provide greater resolution in the mass spectrum.

Beam width does not ultimately determine the resolution of the mass spectrum. The extraction region is divided into two regions, one region of higher voltage and one region of lower voltage. This division helps compensate for the width of the beam. This is commonly referred to as space focusing. The concept is as follows: If the beam is collimated to a width, d, then it is easy to accept that two ions of the same mass could be accelerated from each side of the beam. Ultimately, each would have different kinetic energies since each ion spends two different times in the acceleration region. Therefore, each have different velocities and the concept behind time-of-flight mass spectrometry breaks down. A two-stage acceleration region compensates for this by minimizing the difference in kinetic energy.

The differences in the velocities are proportional to the accelerating field and can be reduced. By dividing the field into two different fields, one can be certain each ion is given a majority for the accelerating potential. For example, for a -2000V accelerating field, could be divided into two fields, as shown in Figure 2-5 and 2-6. If two ions of the same mass and charge enter the acceleration region are separated by some distance, then particles obtain two different kinetic energies. The difference in the kinetic energy is based on the magnitude of the acceleration field. For a single linear field (ΔV_1) the difference is great than a two stage field(ΔV_2).

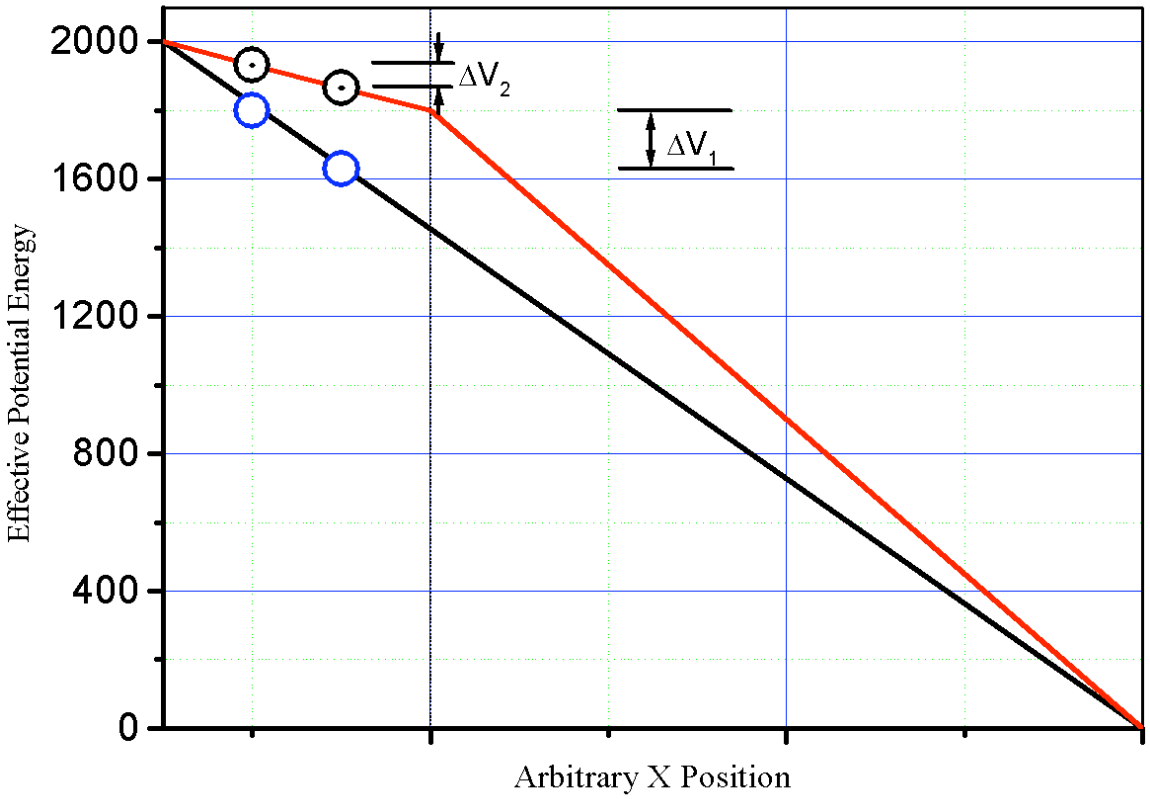

Figure 2-5. A plot of the kinetic energy achieved based on the starting point of the ion in the extraction region of the mass spectrometer.

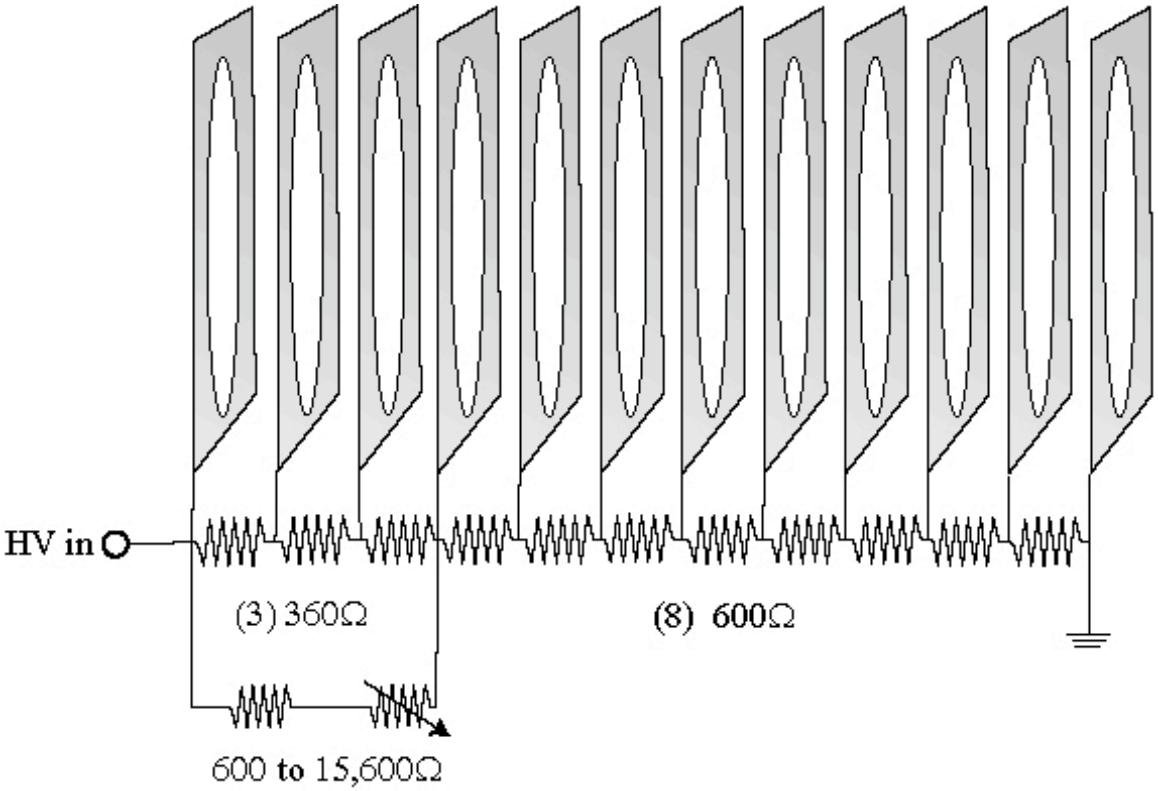

Figure 2-6. The acceleration/extraction region of the time-of-flight mass spectrometer.

2.3.2 Space Focusing and Resolution.[52,53]

The concept of a time-of-flight mass spectrometer (TOF-MS) is based kinetic energy. If two particles of two different masses are given the same kinetic energy, each particle will have a different velocity proportional to its mass. Therefore, the flight time for a particle with a mass m_1 will be different than a particle with mass m_2 over some distance L.

Equation 1.1 defines the force applied to a particle with charge q_0 by an electric field $\vec{E}$ defined in equation 1.2.

$$\vec{F}_E = q_0 \vec{E} \tag{2.1}$$

$$\vec{E} = \frac{V_{acc}}{d^2} \hat{d} \tag{2.2}$$

Where V_{acc} is the voltage of the accelerating field. The distance away from the electric field is defined as d and ε_0 is the permittivity of free space. From this we define the potential, U, of a particle with charge q_0 to be $U = -q_0 \vec{E}\, d$, where d is the distance from the electric field. This can be rewritten as

$$U = \frac{V_{acc}}{d} \tag{2.3}$$

when substituting for the electric field and assuming a singly ionized particle. It is important to note, d can not be zero. If so, there would be no electric field applied to the particle. Since there is nothing to hold the ions at its location, d, the potential is then converted to kinetic energy, $\frac{1}{2} mv^2$.

In theory the acceleration region of a TOF-MS gives a uniform kinetic energy to all ions. This assumes that all particles are accelerated from the same point in space and start with a velocity of zero. In practice, this is not always the case. The ionization processes most often yield a spatial distribution among the particles as well as a velocity vector as shown in Figure 2-5. The difference in spatial separation will in turn effect the resolution in the mass spectrum.

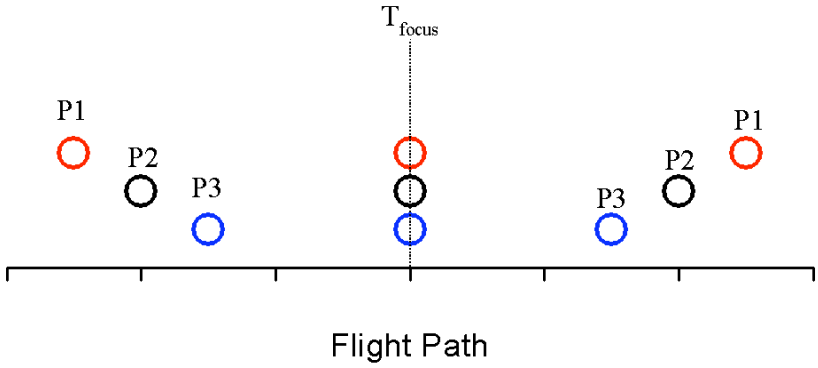

Scheme 1

Scheme 1 diagrams the effect observed when ions of the same mass are accelerated from different distances from the acceleration field. If the particles are separated by some distance, Δd, then each a difference in kinetic energy will result from the difference in potential. Additionally, the flight times of each will be different. This is recognizable when d_1 and d_2 are substituted into equation 1.3. For the case where $d_1 < d_2$, particle P_1 will have a greater potential than P_2. Here the particle P_1, when set into motion, has a greater velocity, but is some distance behind P_2. If P_1 and P_2 are allowed to travel a long enough distance, P_1 will pass P_2 as shown in Scheme 1. The point at which the ions pass each other is referred to as the focusing plane (T_{focus}). By varying the ratio between the tow fields in the acceleration region, the focus plane can be set so that it is at the detector for any given mass. However, the ions that are heavier and lighter than the focused mass will begin to be spread out upon arrival at the detector. Thus, space focusing will *not* provide ultimate resolution for all masses observed in the mass spectrum.

2.3.3 Ion Optics.

The ion beam can be steered and focused much like a beam of light. Electrostatic plates and rings are used instead of prism and lenses. Typically, an isolated plate or ring is given a static potential. The most common type is a simple deflection plate. A deflection plate is a solid, uniform stainless steel plate. Most often accompanying the plate will be a ground plate opposite of it. The ions that are accelerated in the extraction region have a velocity from the motion exiting the FTR. A small deflection plate is used to readjust the trajectory to the ions. Since ions of different masses will then have different momentums, the deflection voltage applied will not redirect all the ions back on target.

A reflectron, as shown in Figure 2-7, is another form of ion optic that is has several benefits. It can reflect an ion beam like a mirror, either back on itself or back along another path. The reflectron is very similar to the extraction region in the fact that it is back into two stages. The first stage is usually of high potential and removes most of the kinetic energy of the ions. This initial slow down adds to the time an ion spends in the reflectron. The longer second stage allows more time for mass separation. The reflectron can also be used to improve resolution. Since the ions of a given mass have an energy distribution, lowering the total potential of the reflectron will allow ions on higher energy to penetrate the reflectron and not be reflected. In a sense, the reflectron acts as a kinetic energy gate to help reduce the energy spread that is unavoidably obtained in the acceleration region.

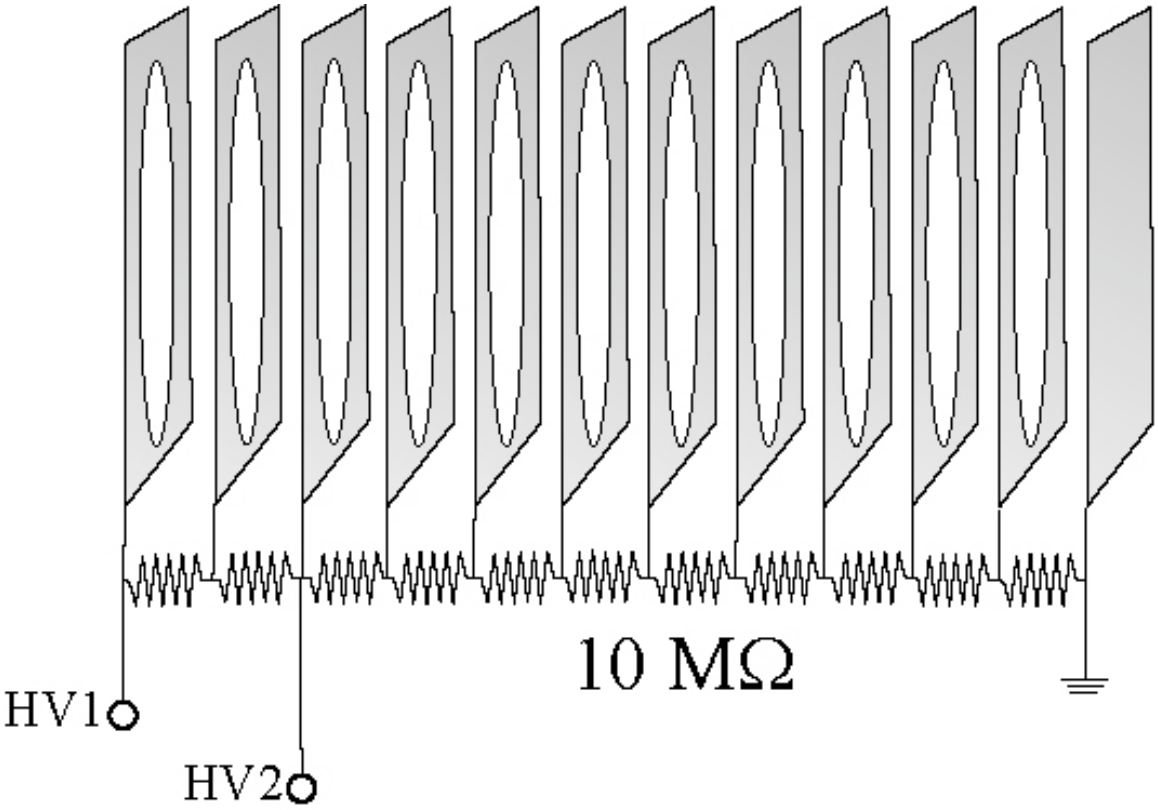

Figure 2-7. Two stage mass reflector.

2.3.4 Ion Detector.

The detector, as shown in Figure 2-8, is a set of stacked micro channel plates. The micro channel plates act as electron multipliers to amplify the ion signal. In the micro channel plate detector used the micro channel plates are floated using HV1 and HV2. The electrons then cascade through the channels in the plates and then are collected by the anode. The detector can be set up to detect positive or negative ions.

The signal from the anode is amplified using a 100 MHz fast video amplifier, Comlinear Corporation, CLC501AJP. The amplified signal is then recorded using a Leroy 9304M, 175 MHz digital storage oscilloscope. Each time-based spectrum is then

averaged with other spectra up to 1000 shots. The average spectrum is then digitized and recorded by a PC using a USB-GPIB interface.

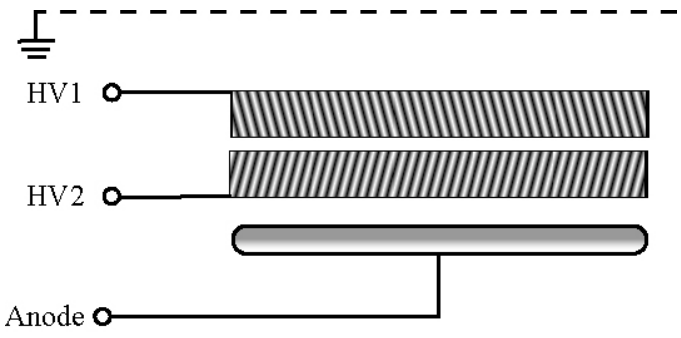

Figure 2-8. Schematic of the Microchannel Plate detector. The multiplication of the electrons is base on the voltage difference between HV1 and HV2. The amplified electrons are then collected by the anode.

CHAPTER III

OXIDATION-STATE TUNING OF VANADIUM OXIDE ANIONS

This chapter discusses various properties of vanadium oxide anions displayed in the mass spectrum. The composition and some structural components will be discussed as well as the ability to control the oxidation of the metal atoms. The repeating pattern and other disparities are included.

3.1 Introduction.

Vanadium oxide clusters, both neutral and ionic, have been of growing interest for applications over the past decade and are of interest in their own right. As a bulk catalyst, V_2O_5 has been found to be useful in many oxidation reactions, including the oxidation of SO_2 to SO_3. In the aqueous phase, polyanionic clusters of vanadium oxide, $V \leq 16$, can be formed that have very versatile redox properties.[30] Formation of stable neutral or near-neutral species has been observed only in the gas phase. Ion-molecule reactions, initially studied as a method to understand the interaction with bulk defect sites, have yielded interesting results.[18,22,54] The reactivities of these clusters have been found to be promising with respect to catalytic processes. But, further research is needed

before these molecules can be used for any practical purposes. First and foremost, a means of synthesis and isolation is needed as well as structural verification.

Theoretical studies have predicted the structures of the neutral di-vanadium pentoxide clusters $(V_2O_5)_n$ to take on a closed-cage structure. (The details of these predictions is discussed below.) Caged structures, such as C_{60}, C_{70}, and other fullerenes, have gained much attention in the past. Aside from these molecules, it has been long predicted that the fullerenes would only be the first of many materials with layered bulk structures to form highly stable cage structures.[55] This behavior is observed again in the boron nitride clusters and then again in the work on vanadium sulfide by Tenne and co-workers.[56] Castleman and co-workers have predicted the structure for Ti_8C_{12}, and other highly stable M_8C_{12} clusters, to form a highly stable cage with T_h symmetry.[57]

3.1.1 Theoretical Predictions & Considerations.

The recent reports by Vyboischikov and Sauer, published in 2000 and 2001, predict that the V_2O_5 composition will yield ultra stable structures in the form of high symmetry cages.[39,40] The early report dealt with the smaller cluster anions and neutral equivalents, $V \leq 4$. The geometric structures were calculated along with electronic affinities. In comparison to experimental electron affinities determined by photoelectron spectroscopy[24,25], the calculations are generally agreeable. Aside from other details of structure, formation and electronic stability, the work demonstrated only slight geometric variances between the anionic and neutral species. Even at low nuclearity, $V_3O_8^-$ and V_3O_8 form closed ring structures. Previously, a ring structure was derived from a single crystal of $V_3O_9^{3-}$.[35] Overall, the resulting calculations corresponded well to the

experimental data available on the species calculated. The theoretical approach, B3LYP or BP86 with a TZV(P) basis set, was found to be a reliable method to use for computations on this metal oxide system.

The latter report focuses on larger vanadium oxide clusters of a V_2O_5 stoichiometry. Consideration was given to each structure beginning with V_4O_{10} and continuing on with a $(V_2O_5)_N$ stoichiometry for N = 2, 3, 4, 5, 8, 10, 12. Figure 3-1 shows the predicted heat of formation of these neutral vanadium oxide clusters, with respect to the bulk form, i.e. the energy of the bulk V_2O_5 is taken to be 0 kJ/mole. As can be seen from Figure 3-1, V_4O_{10} is only ~40kJ/mole above the bulk, and the larger cages converge quickly toward the bulk limit. As a reference, the heat of formation of C_{60} from graphite is about 38 kJ/mole of carbon atoms.[58-61] It can easily be seen that the majority of the clusters are found to be well below that of C_{60} relative to the corresponding bulk forms. A similar decrease is observed for fullerenes larger fullerenes and has been blamed for the coalescence of C_{60} into C_{120}.[62]

The final structures, as mentioned before, are symmetric cage structures. Each of these cage correspond to a three dimensional geometric shape. For example, the clusters V_4O_{10}, V_6O_{15} and V_8O_{20} have structures that best resemble a tetrahedral, tri-prism and cube, respectively. Figure 3-2 gives a depiction of the low energy structures for V_4O_{10}, V_6O_{15} and V_8O_{20} as well as those for $V_{10}O_{25}$, $V_{16}O_{40}$ and $V_{20}O_{50}$. To more easily visualize these geometric structures, one should consider the vanadyl units (V=O) to be at the apexes of the polyhedron with a oxygen atom bridging the vanadyl units (V-O-V) on the edges. They are much like C_{60} in the way that it has a carbon atom at each of the vertices of a truncated icosahedron. It has been proposed by Boldyrev and Simons[63] that

heterogeneous ionic molecules will form a polyhedron cage structure, as long as neighboring atoms are of alternate charge meaning only certain polyhedra are acceptable to form cages. The polyhedron is defined by the location of the vanadium atoms in this case as mentioned earlier. Therefore, this rule is obeyed nicely by the vanadium oxide cage-clusters. Although a metal to metal bond is not forbidden, it is not necessary to have one and the absence of such a bond makes these clusters even more unique.

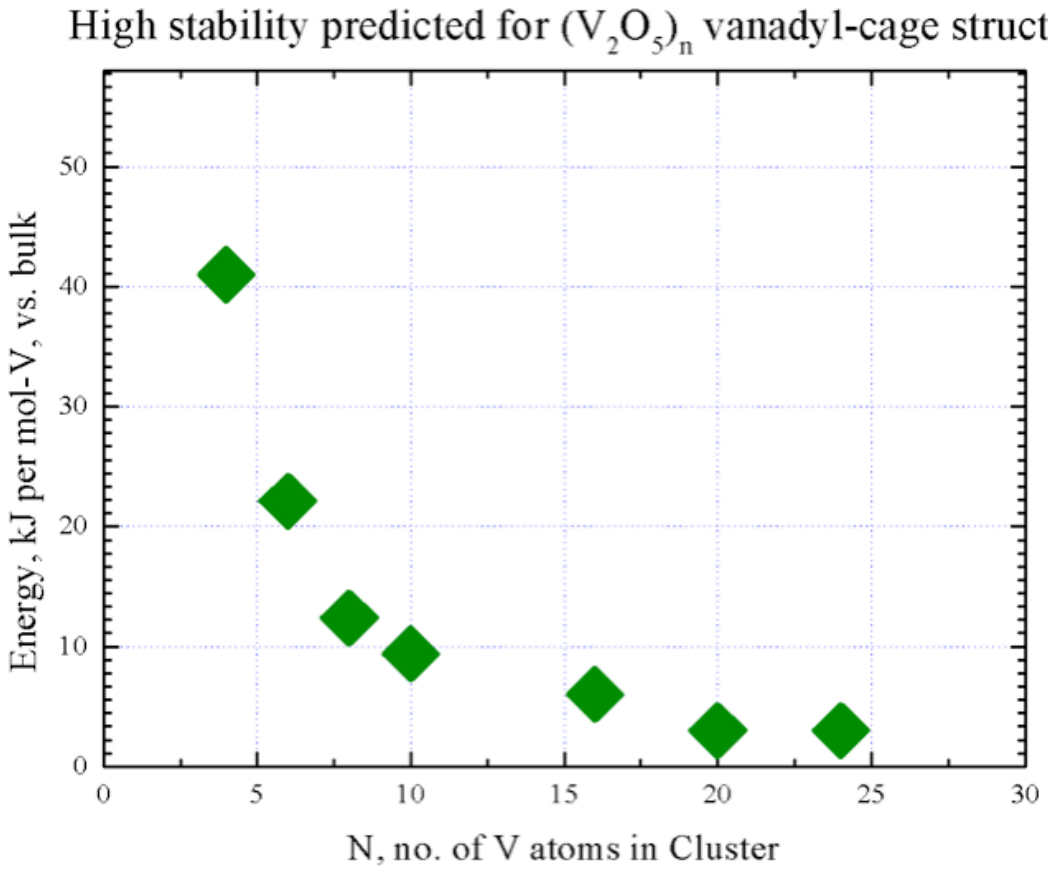

Figure 3-1. Computed energies for $(V_2O_5)_N$ clusters relative to bulk V_2O_5. The calculations were performed by Vyboischikov and Sauer using B3LYP calculations and an all electron TZV-Ahlrich's basis set. The reference at 0 kJ/mol. refers to the bulk vanadium pentoxide. The high stability can be understood by comparison to that of C_{60}, which is approximately 35 kJ mol^{-1} above graphite. Of the clusters represented here, all are well below the 35 kJ mol^{-1} standard with the exception of V_4O_{10}.

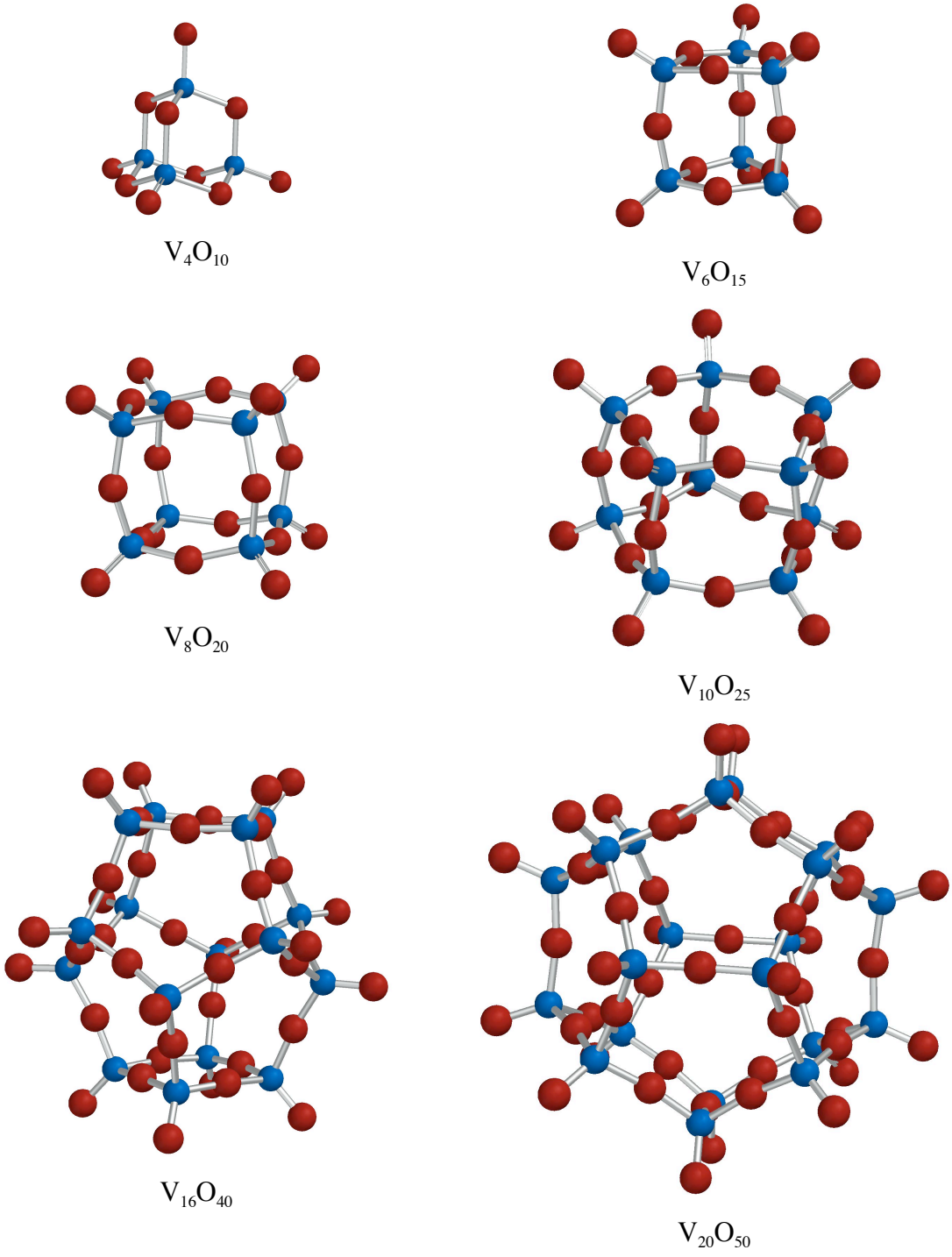

Figure 3-2. Representations of the structures predicted by Vyboischikov and Sauer.

3.1.2 Experimental Considerations.

As energetically favorable as these molecules have been predicted to be, they have yet to be collected from the vapor phase or synthesized via wet chemical methods. The formation of caged clusters is prevalent in polyanionic structures. Polyoxovanadates have been synthesized and have been shown to resemble cage structures. Reports by Day, et al. (1989) describe a half-cage structure for $V_{12}O_{34}^{4-}$. The structure resembles that of a bowl and strongly resembles a cage structure that has terminated growth. Day and co-workers (1989) also reported a closed-cage structure for that of $V_5O_{14}^{3-}$. Figure 3-3 shows a DFT calculated structure for $V_5O_{14}^{3-}$. A brief review of structures formed, including cages, half cages and rings, by polyvanadates can be found in Klemperer et al.[64]

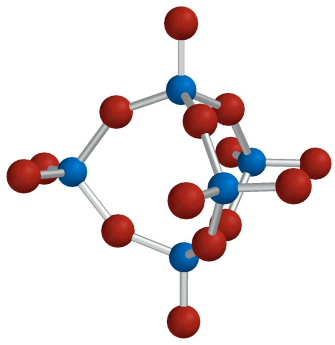

$V_5O_{14}^{3-}$

Figure 3-3. The structure of $V_5O_{14}^{3-}$ as determined by Day and co-workers (1989).

However, not all polyoxovanadates are predicted to be cages. A small series of four polyoxovanadates have been observed, each of which decrease in charge and increase in nuclearity. [29] The series includes the polyanions $[V_6O_{19}]^{8-}$ [65] and $[V_{10}O_{28}]^{6-}$. The third species has been reported by Hou et al. as $V_{13}O_{34}^{3-}$.[29] The structure was

characterized to be composed of distorted VO_6 octahedral units that are in a compact configuration with T_d symmetry. The fourth member of the series is predicted by the authors to be a neutral species, $V_{16}O_{40}$. The structure of $V_{16}O_{40}$ is not predicted to be a cage, but to be a solid tetrahedral comprised of similar octahedral vanadium oxide units. Without a structural reference, one may be mislead in thinking the vanadium takes on a chemically forbidden oxidation. It should be made clear that the internal oxygen atoms are shared between vanadium atoms and are shown to be coordinated to up to 6 vanadium atoms. This compact structure has more complex vanadium and oxygen atoms, mainly oxygen atoms, than the cage structures predicted by Vyboischikov. The 3-fold and 6-fold coordinated oxygen atoms, though absurd on a molecular level, are described and accepted in the polyvanadate cages and rings discussed by Klemperer[64] and throughout the polyoxometallate field.[66]

3.2 Experimental.

Vanadium oxide cluster anions were produced by laser ablation techniques. A pure vanadium target rod (99.9% purity) was purchased with a diameter of 0.25" from Alfa Aesar. The rod had to be machined on a lathe to a diameter of 0.125" and a length of 2.5". The rod was translated and rotated using a 1/4-80 set screw turned by a 1 to 1/3 rpm reversible motor. Once the rod turns to one extreme, the direction is reversed. No data points were collected at the turn around points of the rod. This technique is used to continually give a fresh surface for ablation and eliminates hot spots on the rod that can affect cluster growth. Rotating of the rod is also important to prevent destruction of the rod by drilling holes through the diameter. Keeping a uniform surface for ablation will

also help keep cluster production stable through out the experiment. Figure 3-4 depicts the cluster source and flow tube reactor.

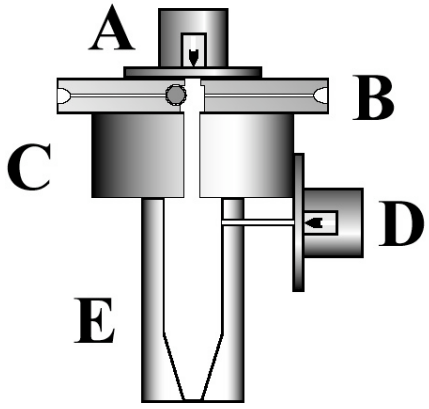

Figure 3-4. Cluster ion source and pulsed helium flow reactor. A- Primary pulsed gas valve. B- Source block containing metal target rod. C- Thermalization region. D- Secondary or reactor pulsed valve. E- Flow tube reactor.

Ablation was done using a focused Nd:YAG laser. The third harmonic was separated using a Pellin Bocca prism. The fundamental and second harmonic beams were blocked. The third harmonic was aligned through a conical lens with a focal length of 20cm. The lens was mounted on an adjustable stage with a micrometer to make fine adjustments. An iris was placed in the beam path so the intensity of the laser could be adjusted. An optical stanchion was also inserted to hold quartz plates and screens for more crude attenuation of the beam.

Oxygen- helium gas mixtures were prepared as the buffer gas. A seeded buffer gas is not uncommon. Seeding the buffer gas is a particularly easy way to assure saturation of a reactant gas that may be added down stream. The gas mixtures were prepared by evacuating a large lecture bottle, 2.5 liters, over night. For a 10% (v/v)

mixture, the evacuated cylinder was then filled with 25 psi (10 psig) of oxygen and then filled to 250 psi (235 psig) of helium. The mixture was then allowed to mix overnight. The gas handling apparatus used to measure out gas pressure was custom built using components from Matheson Tri-Gas. The apparatus is comprised of a leak valve, pressure gauge, and two quick connect fittings. The arrangement of the components is as shown in Scheme 1. The components are connected using Teflon tubing and Swagelock components. The apparatus is kept extremely clean. Between each use it is vacuum pumped and then purged with UHP helium. Any contaminants or impurities, especially humidity, may be reflected in the mass spectrum. It is important that the order each gas is added is consistent for each gas mixture prepared. Gas flow will be different for a seed gas that is added to a cylinder at vacuum versus a cylinder at some pressure just above vacuum.

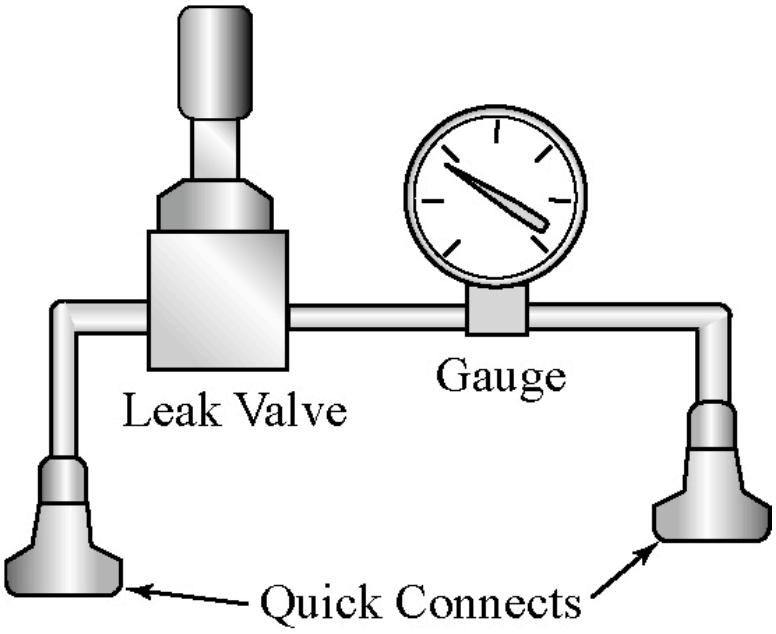

Scheme 1. Gas mixing apparatus.

Complete mixing is essential. If the mixture is not completely mixed, signal becomes unstable due to the velocities at which the carrier travels through the vacuum region between the FTR and the mass spectrometer. Although the production of clusters is not stopped, the timing to initiate the extraction pulse changes irregularly. When the gases are completely mixed, signal and timings remain consistent throughout the experiments.

Initially, the composition of the clusters does not reflect the composition of the carrier gas. Several passes over the rod must be made with the laser to condition the rod. The idea is to remove a few layers of surface atoms and any other impurity that may have some how contaminated the rod. Rod conditioning is also important in that it will result in a consistent ablation target. This conditioning allows also for the gas valve to warm up and prevent any uncommon behavior. Also, any gas separation that may occur when connecting the buffer gas cylinder can be cleared from the line.

In order to understand the rule of the oxygen in cluster production, the percentage of oxygen in the buffer gas was changed. Although more efficient, but rather tedious, making separate oxygen mixtures would be a convenient way to determine the affect. An even similar approach would be to start with high oxygen content and switch to pure helium and record the mass spectra as the gas composition changes. This oxygen-purge technique has provided interesting results, but it is not capable of producing stable enough conditions to perform reliable experiments.

This method did however provide useful information about the vanadium oxide clusters formed in the vaporization source. Although much work has been published on

the topic of cluster growth and cluster composition, slight differences from experiment to experiment leave room for exploration and can provide a new interpretation on a subject.

3.3 Results and Discussion.

Vanadium oxide anions clusters are relatively easy to produce in relation to producing vanadium cluster anions. The mass spectra in Figure 3-5 show the abundances of $V_XO_Y^-$ clusters over a wide mass range. The mass spectra were generated by using a gas mixture an oxygen-helium gas mixture of 10% oxygen as the carrier gas. It can be observed that the peaks at high mass are much broader that the peaks at lower mass. This loss of resolution is not uncommon at higher mass and should be expected. Since the mass to time-of-flight (TOF) conversion is quadratic ($\text{mass} \propto t^2$), the number of time data points making up a peak corresponding to a mass m_1 will be less for all mass peaks greater than m_1. In order to increase the resolution higher mass peaks, the mass spectrometer settings will need to be adjusted. In return, resolution at low mass will be lost. Regardless of resolution, the amplitude of the peaks displayed in Figure 3-2 for mass above 2000 amu, does not accurately represent the ion abundance for each cluster.

Another character worth commenting on is the shape of the mass spectrum. In comparison of the two separate mass spectra in Figure 3-5, it can be observed that mass peaks around 1000 amu appear to be weak in each spectrum. From this one may conclude that the ion abundances of a cluster like $V_{13}O_{33}^-$ at 1191 amu may have only a small existence in clusters created. This conclusion is incorrect. In fact, each of the clusters all appear with nearly equal intensity respectively to each other. This is easily observed in the experiments. However, the dependency on a deflecting voltage creates

this illusion in the mass spectrum. With out multiplying the observed intensities by a scaling function, the true intensities are lost in all mass spectra displaying a wide mass range. Nevertheless, this discrepancy in the true intensity and observed intensity may not have any adverse effect on comparison of peaks in a small mass range (with in 100 amu.) The loss of intensities on either side of a centralized mass peak correlates approximately as follows:

$$I_{OBS}(m) = I_{True}(m)\, e^{\frac{-(m-m_o)}{2\sigma^2}} \qquad (1)$$

Where, m is the mass, m_o is the mass about which the distribution is centered and σ is half of the width of the distribution.

The mass spectra in Figure 3-5 clearly display a distinct pattern. Upon further inspection, a five fold repeat pattern emerges. Figure 3-6 clearly distinguishes this pattern. As the mass increases, more peaks may be added to pattern, but the five fundamental peaks remain the most intense. The peaks in Figure 3-6 are labeled A-E and are assigned masses and molecular formulas. Peaks A and B contain an odd number of vanadium atoms, while peaks C through E contain an even number. Table 1 gives the masses and molecular formulas for lowest set of peaks in Figure 3-6. Table 1 summarizes the repeat pattern by giving a general formula. The key property of the formula is the close resemblance to vanadia, V_2O_5. With the stoichiometry of vanadia, the vanadium atoms are in the +5 oxidation state. Given this fact, the only explanation of the clusters containing more than 5N oxygen atoms and an electron is that the non-bridging oxygen atoms are not O^{2-}. Instead these oxygen atoms exist as peroxides and superoxides. This conclusion is arrived by balancing the charges with the anion.

Assigning each vanadium atom a +5 charge and the sum of the oxygen charges would need to be 5N+1 to achieve a net negative charge.

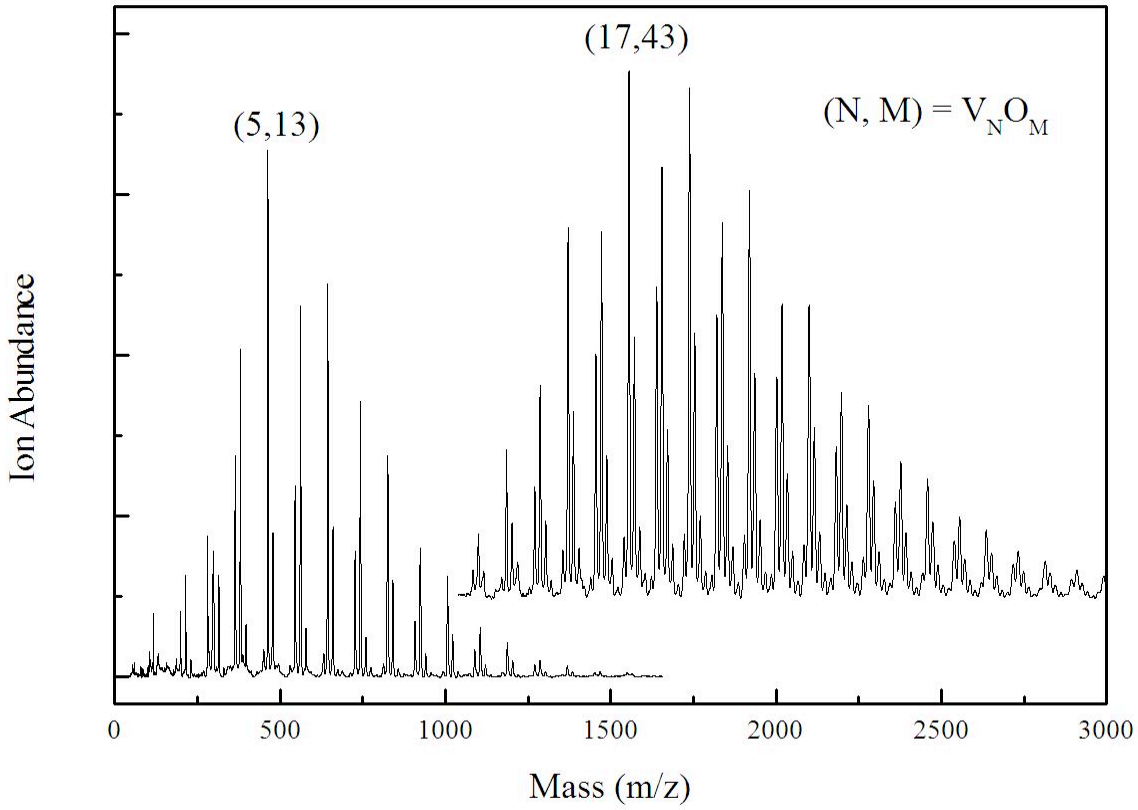

Figure 3-5. Mass spectra of vanadium oxide anions produced by laser ablation. The annotation (N, M) is used to represent the formula $V_N O_M^-$.

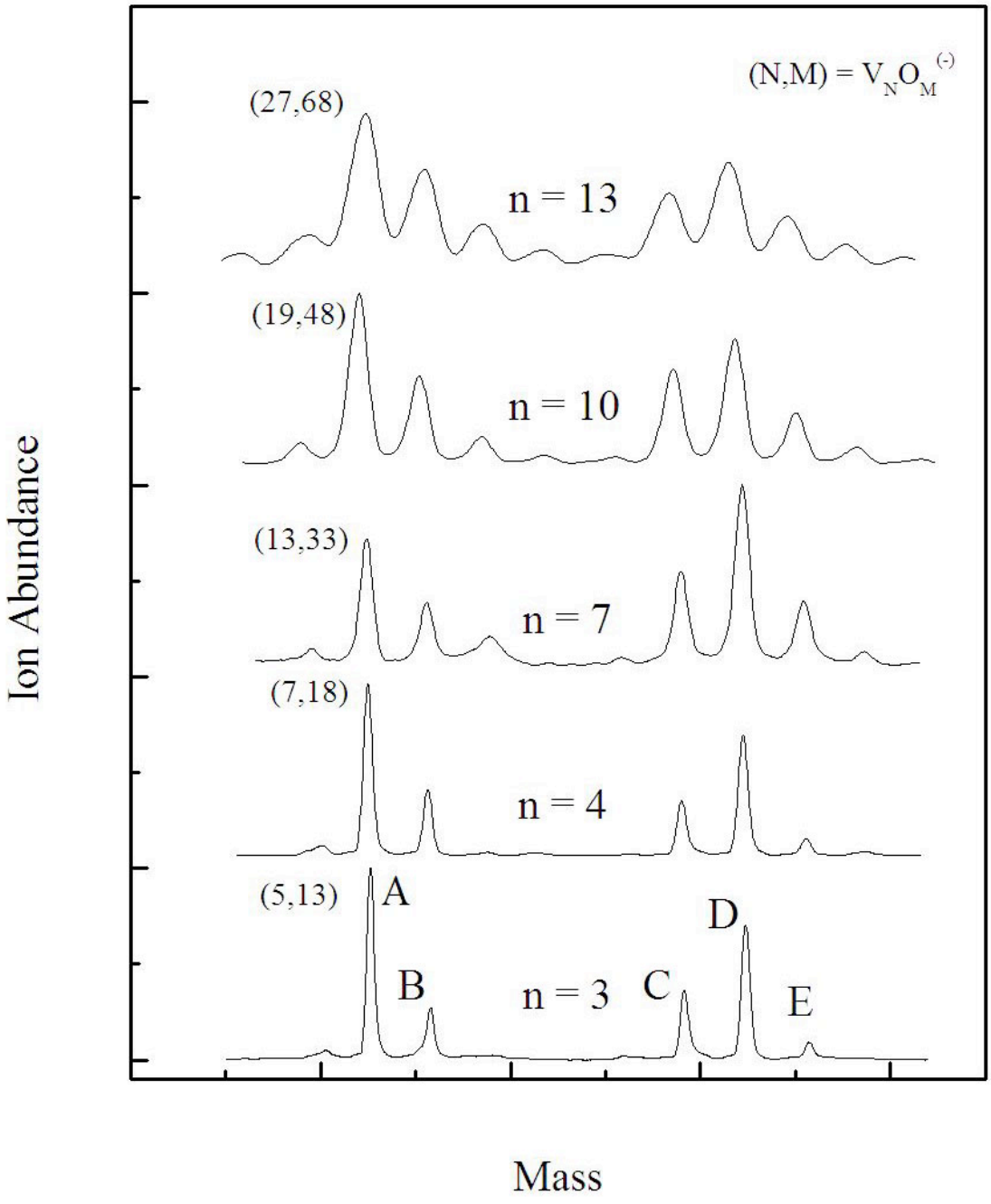

Figure 3-6. Repeating pattern observed in vanadium oxide anion mass spectrum. The stoichiometry for each peak can be calculated from the formula given in Table 1.

Table 3-1. Summary of peaks that arise in the $(V_2O_5)_N^-$ mass spectrum.

Peak	Formula	Example n = 3	Molecular Addition to A	Mass (amu)	Defect Assignment
A	$V_{2n-1}O_{5n-2}$	$V_5O_{13}^{(-)}$		463	None
B	$V_{2n-1}O_{5n-1}$	$V_5O_{14}^{(-)}$	+O	479	Peroxo, $O_2^{(2-)}$
C	$V_{2n}O_{5n}$	$V_6O_{15}^{(-)}$	$+VO_2$	546	d^1 center
D	$V_{2n}O_{5n+1}$	$V_6O_{16}^{(-)}$	$+VO_3$	562	d^1 and Peroxo,[a]
E	$V_{2n}O_{5n+2}$	$V_6O_{17}^{(-)}$	$+VO_4$	578	Superoxo, $O_2^{(-)}$

Peak A, $V_5O_{13}^-$ at 463 amu, and similarly assigned clusters are the only defect free clusters. In the case of $V_5O_{13}^-$, 5 vanadium atoms at +5 and 13 oxygen atoms at -2 yield a negative charge. The other peaks do not work out so nicely. Peak B corresponds to the addition of an oxygen atom to peak A, $V_5O_{14}^-$. The consequence of assigning all oxygen atoms a -2 charge results in the cluster taking a -3 charge. A way to make up the two electrons is assign a peroxide group, O_2^{2-}, to the cluster. This satisfies the net negative charge and preserves all rules pertaining to electron counting. Since the peroxo form is not as favored as the oxide form of oxygen, this would explain the decrease in the abundance of this peak.

The series of clusters that contain an even number of vanadium atoms, peaks C, D, and E, can be described as the addition of VO_2 and VO_3 to the base peak A. The addition of these units to the base peak is consistent with the low-mass results of Castleman and co-workers.[49] Peak C has a formula that is an exact multiple of V_2O_5. The assignment of an electron to the d orbitals (d^1) of the vanadium atoms is the most logical. Computational results for $V_4O_{10}^-$ from ref. [[40]], shows a d-orbital delocalized about the

metal atoms of the tetrahedral structure. This explanation is accepted and is adapted to explain the residence of the extra electron all cluster following the $V_{2N}O_{5N}^-$ formula. Peak D would be the result of the addition of an oxygen to peak C or the addition of a VO_3 unit to peak A. Assigned defects in this cluster are a d^1 electron and peroxo unit. Peaks of type E that are very low in intensity may reasonably contain a superoxo unit. This unit is expected to be very reactive, which may account for the low intensity observed in the mass spectrum.

This Scheme holds up with one exception. The exception is at $V_3O_9^-$. This cluster has unique properties. The inset in Figure 3-7 shows an expansion of the clusters. The center set of peak are roughly $V_3O_9^-$ with $V_3O_8^-$ to the left and $V_3O_{10}^-$ to the right. The $V_3O_9^{3-}$ cluster has gained some attention in the solution phase[35] and for good reason. In the gas phase it shows a very high affinity for hydrogen as apparent in the mass spectrum with peaks showing up at 297, 298 and 299 amu. Under condition where a trace amount of water is present in the vaporization region, all of the vanadium oxide clusters show similar multi-hydrogen additions. Under what would be considered very clean conditions, $V_3O_9^-$ shows the addition of hydrogen. Not only do these $V_3O_X^-$ clusters absorb any trace amount of water, but they also break the repeat pattern described earlier. In this cluster vaporization source, it very difficult to eliminate all peaks corresponding to $V_3O_9H^-$ and $V_3O_9H_2^-$. This cluster has a very uncanny ability to adsorb water molecules or free hydrogen atoms during formation.

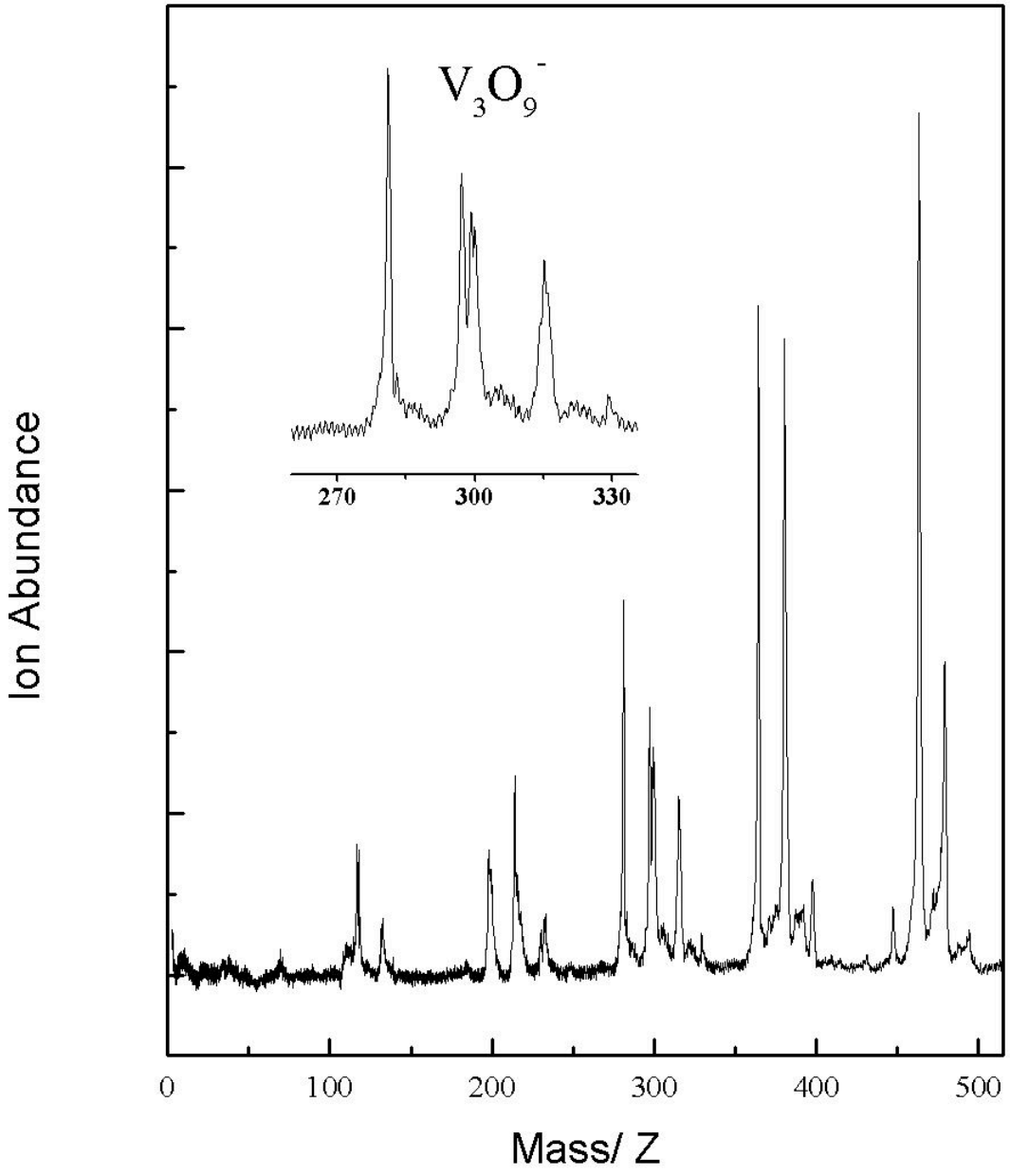

Figure 3-7. Mass spectra of Vanadium Oxide anion. The inset shows a peak splitting of $V_3O_9^-$. The peaks are one amu spacing indicating an strong affinity for water or free hydrogen.

For anions with less than three vanadium atoms, collecting hydrogen atoms, hydroxides, or water molecules is not uncommon. For the mass spectrum show in Figure 3-7, all clusters $V_XO_Y^-$, where $X \leq 3$, the display the addition of such units. In the condensed phase, these clusters all are defined to be polyanions with either charge balancing ligands or hydrogen atoms. The idiosyncrasy of this particular group of clusters is no coincidence. The strange behavior can be attributed to a structural transition point. From DFT calculations performed by Vyboischikov et al.[40], $V_3O_8^-$ is the first cluster to form a closed structure. For VO_X^- and $V_2O_X^-$, ring formation is quite difficult and maybe sterically impossible. The $V_3O_8^-$ can form a stable chain structure with in 0.5 eV higher energy than the ring; both structures were found to be minima. Nevertheless, this cluster marks a transition point from which the conversion from chains to rings occurs.

The robust spectrum shown in Figure 3-5 is practically impervious to reactant gases. Addition of CO, CO_2, H_2O, and O_2 in the FTR, gave no result. The amount of these gases where raised to the point where the all peaks in the mass spectrum were diminished and still no reaction could be detected. This result was very strange. By the theory presented above there should be ample defects in the clusters, mostly reactive forms of oxygen that should have reacted with the gases present.

To better understand the rule of the oxygen, the amount of oxygen seeded in the carrier gas was reduced. An initial reduction from 10% to 2% showed no sign of change to the mass spectrum up to 1000 amu. To expedite the investigation, the oxygen helium mixture would be switched to a pure helium mixture during the experiment. The idea is the oxygen-helium mixture still resides in the gas line leading the pulsed valve, but this

gas would eventually be completely consumed. The transition from a mixture to the pure helium would include a sampling of dilutions in one experiment. Figure 3-8 shows the results from the oxygen-purged experiment. Very rapid change in the mass spectrum takes place. The number of shots taken per each mass spectrum is only about 300. The mass spectra were saved as fast as they could be collected. The time elapsed for the transition from the bottom to top was about 15 minutes at 7 Hz. There is about a 10 to 15 second lag between spectra while the previous spectrum was being saved.

The experiment yielded some very interesting information. The first is that the production of clusters is not completely ceased with an oxygen poor carrier gas. Instead, many changes occur. The first and most obvious is the introduction of new clusters that appear in between the already existing clusters. These clusters turn out to have the same number of vanadium atoms as the clusters sets to the right, but have fewer oxygen atoms. If the metal atoms in the clusters described in Figures 3-5 through 3-7 are in a fully oxidized +5 oxidation state, then the new intermediate clusters formed contain partially oxidized metal atoms.

As the carrier gas becomes more oxygen deficient, so do the clusters that are formed. Toward the end of the data set collected, there isn't a sufficient amount of oxygen present to fully oxidize the clusters as they were at the bottom of the experiment. Guide lines have been drawn into Figure 3-8 to track two fully oxidized clusters $V_4O_{11}^-$ (380 amu) and $V_5O_{13}^-$ (463 amu).

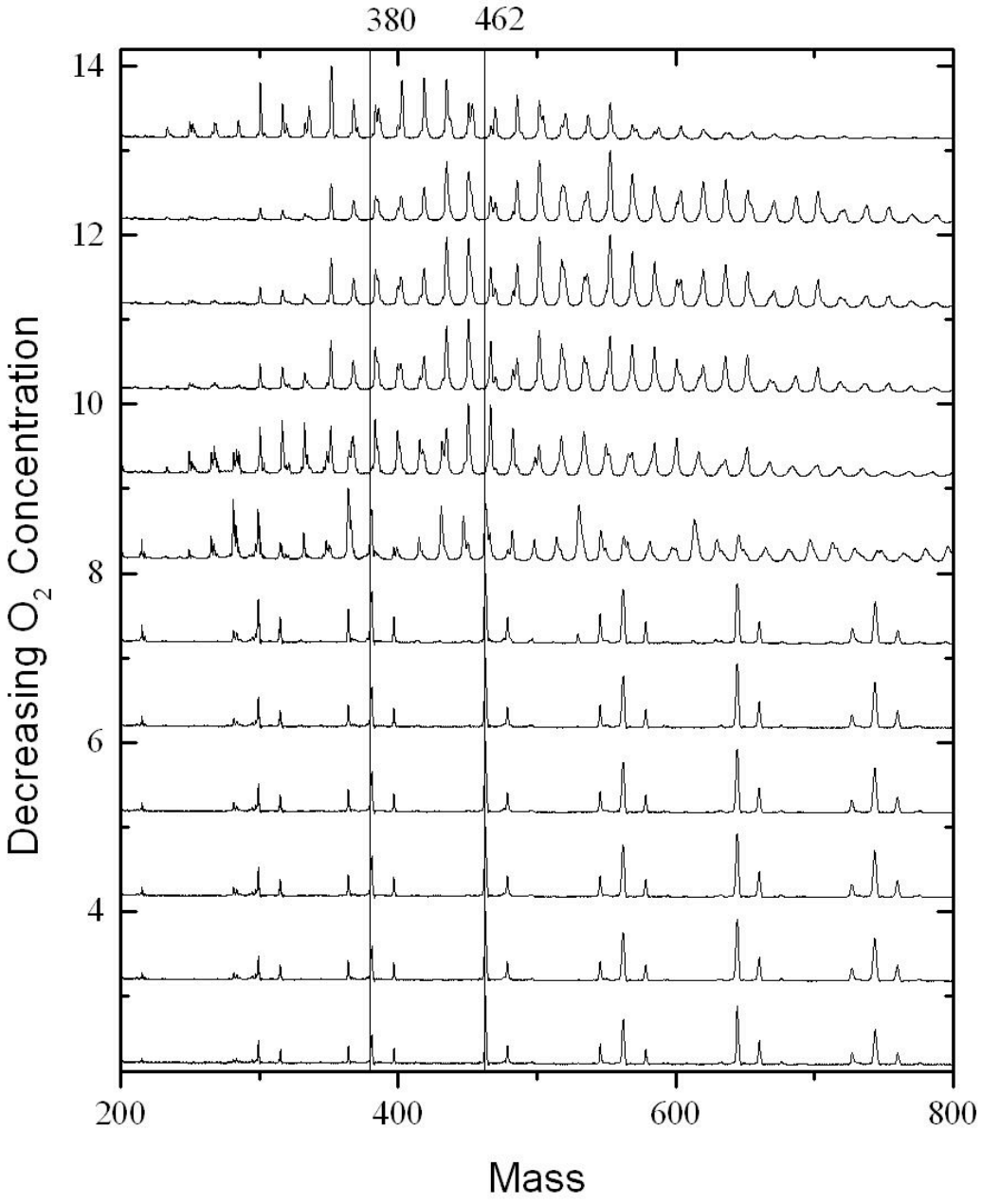

Figure 3-8. Result from *in situ* purging of oxygen in the buffer gas. Beginning with a 10% mixture of O_2:He in the bottom mass spectrum, pure helium is introduced into the gas line behind the main valve. As a result the oxygen content is slowly diminished and composition of the clusters are changed as reflected by the upper mass spectra. For reference, the grid lines at 380 amu and 462 amu are placed to trace the disappearance of the clusters $V_4O_{11}^-$ and $V_5O_{13}^-$, respectively.

The production of these reduced clusters calls for a need to compare clusters of various cluster compositions. Fully oxidized clusters such as clusters $V_4O_{11}^-$ and $V_5O_{13}^-$ could be different due to the oxidation states of the oxygen atoms they possessed. Now in the case of these new stoichiometries, it may be assumed there is no reason for an oxygen atom to take on another oxidation state than O^{2-}. In order to conserve charge and account for all electrons, the vanadium atom must now take on an oxidation state other than +5. Further analysis of this conclusion leads to another crossroad in the fact that a cluster could account for the alternate oxidation state via a combination of oxidation states. For example, $V_5O_{12}^-$ can have several acceptable oxidation states for the vanadium atoms. It could have 4 metal atoms in the +5 state and one in a +3 state. Another possibility is to have 3 in the +5 state and 2 in a +4 state. With out performing spectroscopic studied or some quantum calculations, the determination of the individual oxidation states may not be able to be determined. To solve this dilemma, the cluster may be referred to have an average oxidation state defined as:

$$Z = \frac{2(\text{number of oxygens}) - 1}{(\text{number of metal atoms})}$$

The ability of the clusters to take on other oxidation states, leaves the opportunity to study a wide range of clusters. When the clusters become too oxygen deficient, clusters which differ by one vanadium atom and 3 oxygen atoms appear close to each other in the mass spectrum. The inset in Figure 3-9, shows such a near overlap. The

clusters are separated by 3 amu and should be easily distinguish from one another with sufficient resolution.

Figure 3-9 demonstrate the ability to tune the oxidation states of the clusters by controlling the amount of oxygen present. This technique has allowed experiments to continue in new directions and provide interesting results as will be discussed in the following chapters.

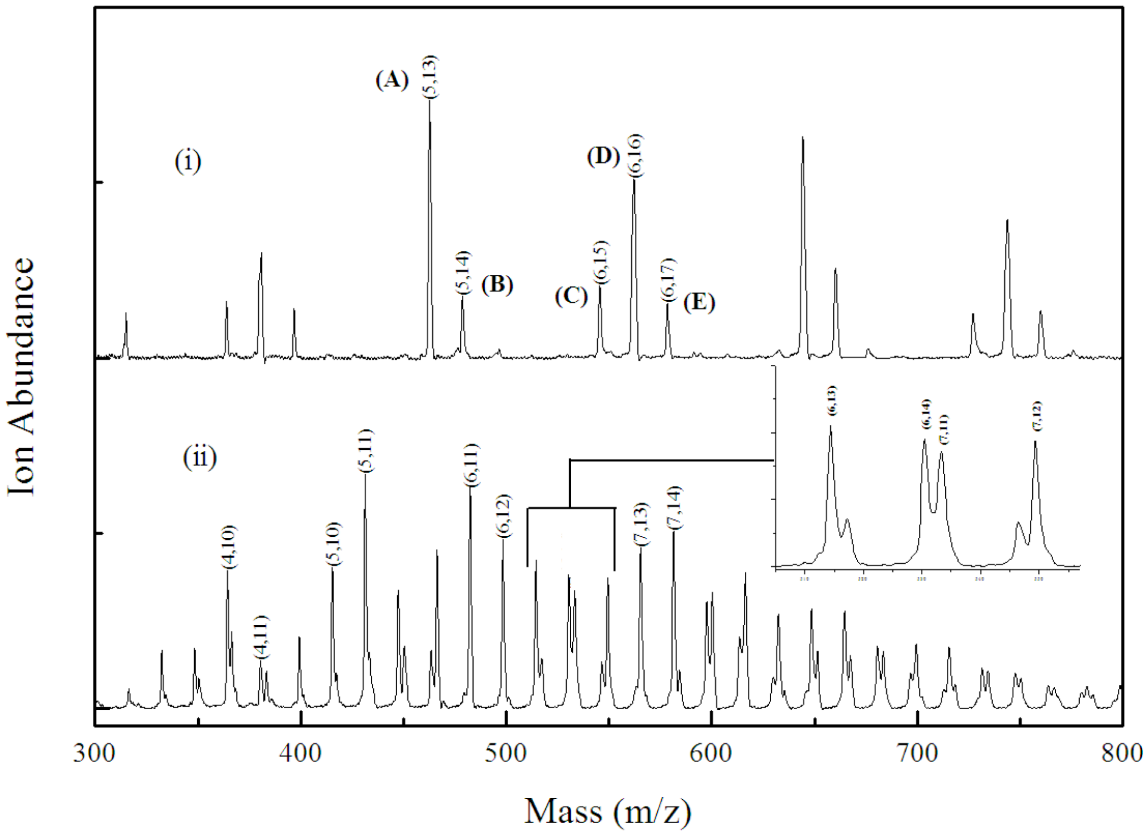

Figure 3-9. Oxidation state tuned vanadium oxide anion clusters. Mass spectrum(i) is collected with high oxygen content in the carrier gas and the metal atoms of the clusters achieve maximum +5 oxidation state. Mass spectrum (ii) is the result from a much lower oxygen content in the carrier gas, less than 0.1%. The fully oxidized clusters are nearly depleted and oxygen poor clusters are produced.

The production of vanadium oxide anions can be produced in carrier gases other than helium. The use of argon or nitrogen would provide different conditions in which the clusters are studied. Ultimately a goal would be to make the carrier gas and the environment nearly the same composition as the atmosphere by introducing humidity and heterogeneous gases. Figure 3-10 shows the production of the vanadium oxide clusters using an oxygen-argon mixture. Since the velocity of the argon gas is slower than that of helium in the vacuum region between the exit of the flow tube and mass spectrometer, the velocity of the clusters is also slower. Because of this difference in velocity, the correction field need to redirect the clusters toward the detector is less and in turn a wide mass range of clusters is observed.

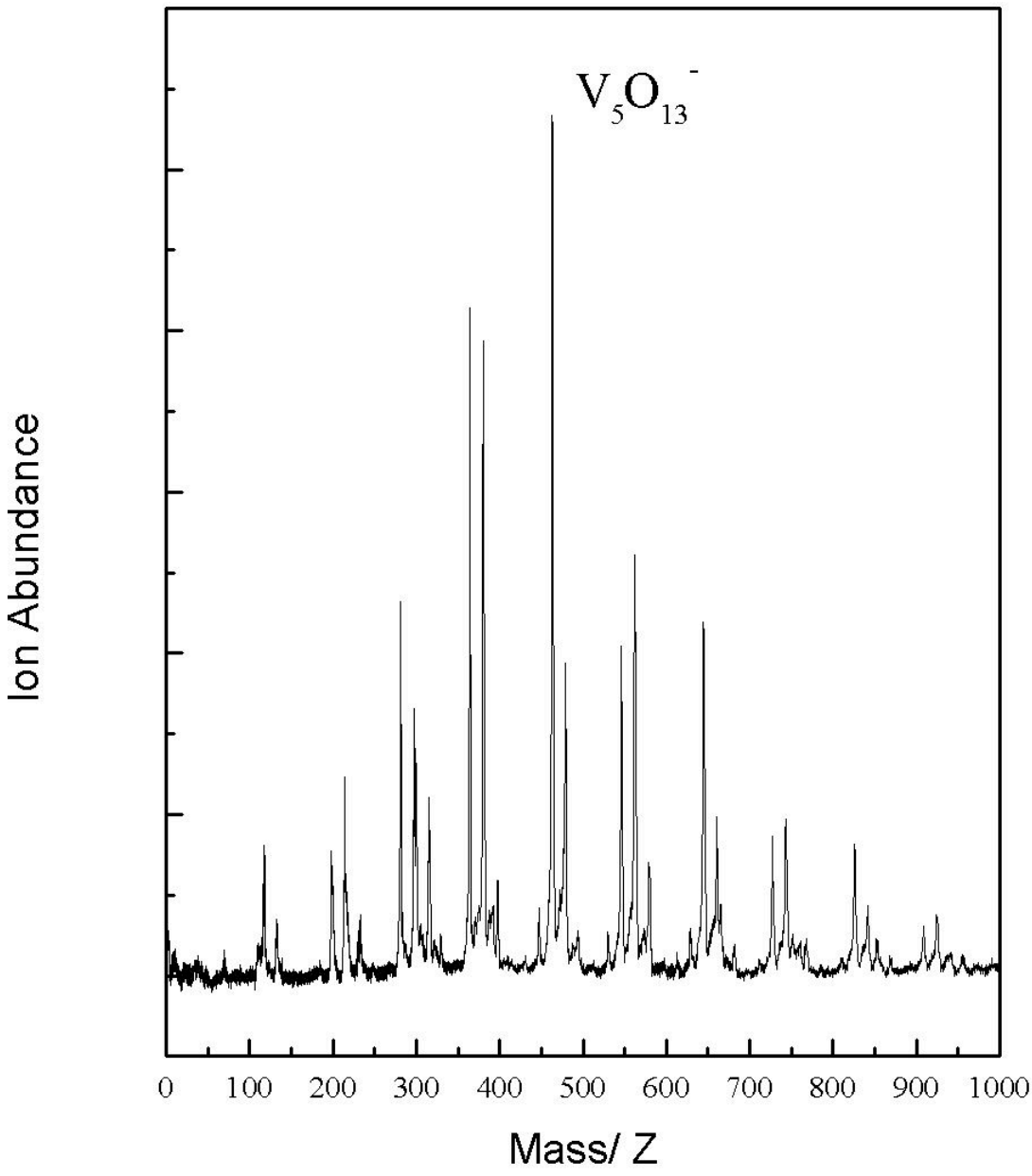

Figure 3-10. Vanadium oxide anions cluster produced using an Ar:O_2 mixture.

CHAPTER IV

REACTIONS OF VANADIUM OXIDE ANION CLUSTERS WITH SO_2

4.1 Introduction.

Based on theoretical calculations,[39,40] the vanadium oxide anion spectrum can be divided into two groups: open chain clusters and closed caged clusters. Chain clusters in the low mass region are VO_x^-, $V_2O_x^-$ and $V_3O_x^-$. The high mass region contains the cage clusters beginning with the first of the caged clusters of $V_4O_x^-$. The clusters can be used as models for surface sites on bulk catalysts and their individual chemical interactions could be studied.[18] The high mass region may also be thought of as individual molecules and used as models for polyoxometalates.[66] All of the cluster anions produced are very stable, both geometrically and electro-structurally. By controlling the amount of oxygen present during cluster production, the average oxidation state of the cluster can be controlled. The composition of the clusters can be readily tuned according to the needs of the experiment. The reduction of oxygen in the buffer gas yields an increased oxidation number of the metal atoms by reducing the number of oxygen atoms in the clusters. If the stoichiometry becomes too metal rich, metal-metal bonds may begin to form. There is no reason to believe the removal of one or two oxygen atoms will

denature the cluster with respect to its fully oxidized form. It is therefore assumed the clusters still maintain a structure similar to those calculated for the fully oxidized clusters. With out an extensive experimental study coupled to theoretical calculations investigating the structure of the clusters, there can be no indication whether this assumption holds true. There is good reason to believe this is the case based on previous experimental and theoretical studies.

4.2 Experimental.

The experimental apparatus is as described in Chapter 2. For the following experiments the helium buffer gas was seeded with oxygen. For example, a helium-oxygen gas mixture was prepared that contained 90 kPa of oxygen with a total pressure of 1800 kPa. According to Dalton's Law, the partial pressure of oxygen, P_{O2}, is calculated to be 0.5% of the total pressure. Unless otherwise specified, the composition of the buffer gas used for the experiments in these experiments is 0.5% oxygen in helium. Similar mixtures of reactant gases were prepared in this fashion. The reactant gases, however, were of a much higher partial pressure, up to 20% in helium. In this case, the use of a below-atmospheric pressure gauge is not necessary and the pressure of the reactant gas was measured using a standard gas regulator. This also avoided any accidental contamination of other gas mixtures. For a 10% mixture of SO_2, 25 psi (10 psig) would be added to an evacuated cylinder. The cylinder would then be filled with helium to a total pressure of 250 psi (235 psig) and allowed to mix overnight.

Reactions were studied as a function of the partial pressure of the SO_2 in the reactor. For such experiments, the partial pressure of the reactant gas was controlled by the amount of reactant gas added in the reactor down stream. The amount is managed by

adjusting the reaction valve pulse duration, which varies the partial pressure of SO_2 in the reactor. This was easily managed using the valve control electronics and recording the change in the chamber pressure. The valve duration can be controlled in 1 μs intervals. Typically, 5 to 10 μs are effective time intervals. The increased partial pressure is then calculated by the increase of the average chamber pressure. The increments can accurately be measured to $1x10^{-6}$ torr and are limited by the ionization pressure gauge. Lower pressure increments can be acquired by firing only the reaction valve, but this practice leads to back streaming of the reactant gas into the vaporization region. Measurements of this type were done at the end of an experiment to prevent contamination.

As discussed in chapter 2, three different flow tube reactors (FTR) have been used in the experiments. Each reactor has specific dimensions. The different dimensions provide a range of reactor pressures and reaction times. The variation in these parameters provides useful information about the particular system. The lack of precise measurement of the FTR's total pressure results in only calculated pressures resulting in approximate and limited results.

4.3 Experimental Results.

4.3.1 Range of Conditions Explored.

The interaction of VO_x-cluster anions with rare gases have been performed at different partial pressures $\{P_{O_2}, P_{SO_2}\}$ and total pressures, P. The partial pressure was varied up to almost 4 mbar while the total pressures investigated were between 200 mbar

to 400 mbar. The distinct results from each these experiments are presented in the following sections.

4.3.2 Highest P_{SO_2} Conditions Explored: Saturation Compositions

The cluster anions in the reference spectrum in Figure 4-1c were produced under fully oxidizing conditions, >5% oxygen in the carrier gas. The clusters have an average oxidation state (Z) of +5 for the metal centers except for $V_4O_{10}^-$ and $V_6O_{15}^-$. Cluster anions with Z = +5 produce very strong, stable mass spectra as discussed in Chapter III. The five-fold repeating pattern persists throughout the spectrum, as evidence of the highly ordered cluster system. However, as interesting and easy as this mass spectrum is to produce, it is hardly affected when exposed to reactive gases such as CO, CO_2, H_2O, O_2, and SO_2 in the 25-mm stainless steel reactor. The robust spectrum is preserved and only minimal ion-molecule scattering effects are observed when these reactants are added to the flow tube reactor FTR. There are no detectable adsorption peaks in the resulting mass spectra.

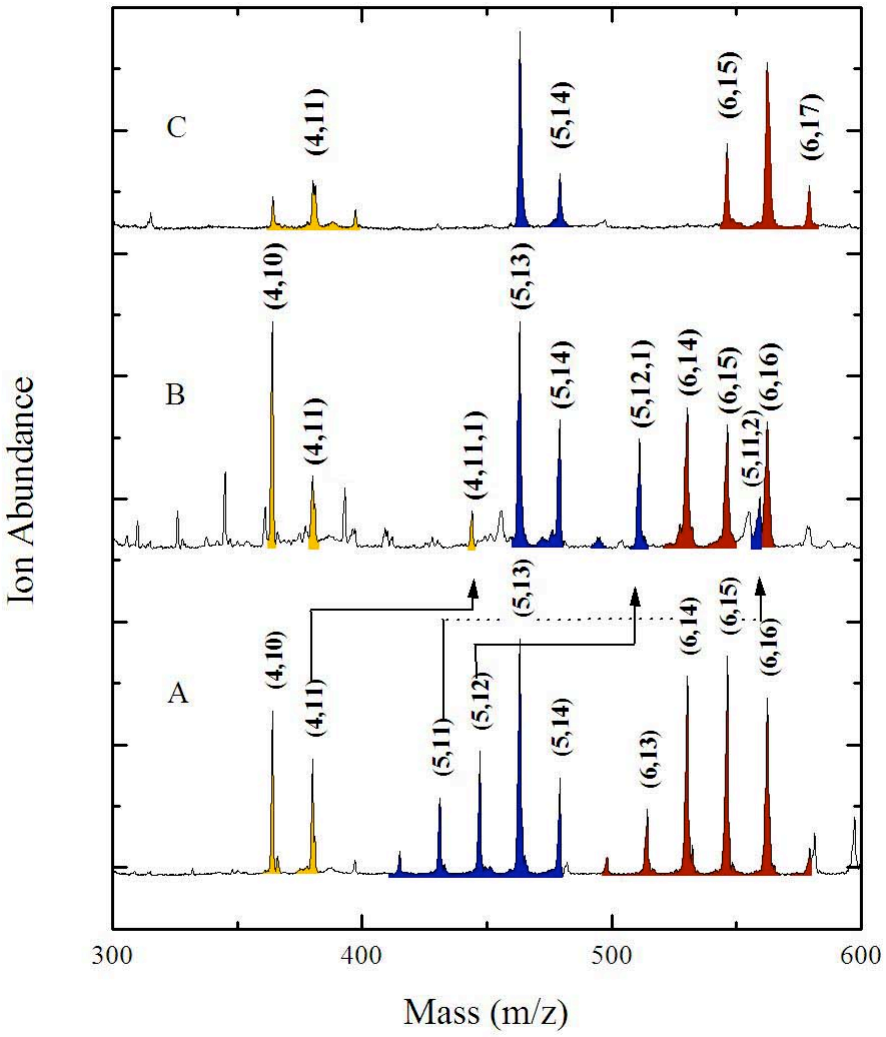

Figure 4-1. Spectrum A shows a vanadium oxide anion spectrum produced with 0.5% O_2:He. The cluster peaks are labeled as (m,n,p), corresponding to $V_mO_n(SO_2)_p^-$. Spectrum B is an example of the result that found after reacting the clusters in spectrum A with SO_2. It is notable that the fully oxidized clusters, as shown in spectrum C, do not adsorb SO_2.

Spectrum A in Figure 4-1 shows the composition of the vanadium oxide anions using a 0.5% O_2:He mixture as the buffer gas. When comparing the clusters in spectrum A to the clusters in spectrum C, which is produced by using a higher percentage of oxygen in the buffer gas, less than fully oxidized clusters can be identified. The formation of the fully oxidized clusters $V_4O^-_{10,11}$, $V_5O^-_{13,14}$, and $V_6O^-_{15,16,17}$, as well as less than fully oxidized clusters $V_5O^-_{10,11,12}$ and $V_6O^-_{13,14}$, provides a mixed mass spectrum of an unreactive species with a species that is found to be reactive.

The addition of SO_2 in the FTR produced notable adsorption reactions to the reduced clusters. Spectrum B shows the mass spectrum when of 10% SO_2 in helium is added downstream. It is easily observed that the fully oxidized clusters do not react as they are still present in spectrum B. The manner in which the SO_2 adds to the reduced clusters is quite interesting.

$$V_5O^-_{10}\ (415) + SO_2 \longrightarrow V_5O_{10}(SO_2)^-\ (479) \xrightarrow{SO_2} V_5O_{10}(SO_2)^-_2\ (543)$$
$$V_5O^-_{11}\ (431) + SO_2 \longrightarrow V_5O_{11}(SO_2)^-\ (495) \xrightarrow{SO_2} V_5O_{11}(SO_2)^-_2\ (559)$$
$$V_5O^-_{12}\ (447) + SO_2 \longrightarrow V_5O_{12}(SO_2)^-\ (511) \xrightarrow{SO_2} V_5O_{12}(SO_2)^-_2\ (575)$$

Scheme 1

Scheme 1 summarizes the interaction of $V_5O^-_{10,11,12}$ cluster with SO_2. The three processes displayed in this Scheme can be identified from Figure 4-1 B. However, From Figure 4-1 alone, the first reaction, $V_5O^-_{10}$ with SO_2, is not so unambiguous. The product $V_5O_{10}SO^-_2$ happens to have the same mass, 479, as $V_5O^-_{14}$. This type of mass coincidence can be expected since the mass of SO_2 is 64 amu, equivalent to four oxygen atoms. But

this phenomenon can be reconciled with other observations. First is there is a notable decrease or disappearance of the peak at 415 amu that corresponds to $V_5O_{10}^-$. The second observation is the significant increase in the intensity of the peak at 479 in relation to the peak at 463, $V_5O_{13}^-$. Quantitatively, the increase is nearly equal to the intensity of the $V_5O_{10}^-$ peak in spectrum A. The absence of a second product peak at 543, corresponding to $V_5O_{10}(SO_2)_2^-$, suggests that the second absorption step does not occur in this experiment.

The reactions of $V_5O_{11}^-$ and $V_5O_{12}^-$ with SO_2 are also observed to go to completion during the experiments. The mass spectra show the reactions occur as shown in Scheme 1. In the case of $V_5O_{12}^-$ only one SO_2 is adsorbed, whereas $V_5O_{11}^-$ is observed to adsorb a second SO_2. These correspond to the saturation compositions and are interpreted in the discussion.

4.3.3 Reactivity at Intermediate P_{O_2}.

Careful examination of the mass spectra taken unreduced P_{O_2} conditions show that fully oxidized clusters have detectable reactivity. The high resolution mass spectrum in Figure 4-2 shows peaks that correspond to SO_2 on $V_5O_{13}^-$ and $V_5O_{14}^-$. The peaks are very weak in comparison to the other peaks in the mass spectrum. Also, the secondary addition of SO_2 to $V_5O_{11}^-$ can also be seen labeled as $\gamma_{5,11}$. If all other reaction processes are disregarded, it can easily be agreed upon that rate of adsorption to $V_5O_{13}^-$ and $V_5O_{14}^-$ is much slower than the rate of adsorption to that of $V_5O_{12}^-$.

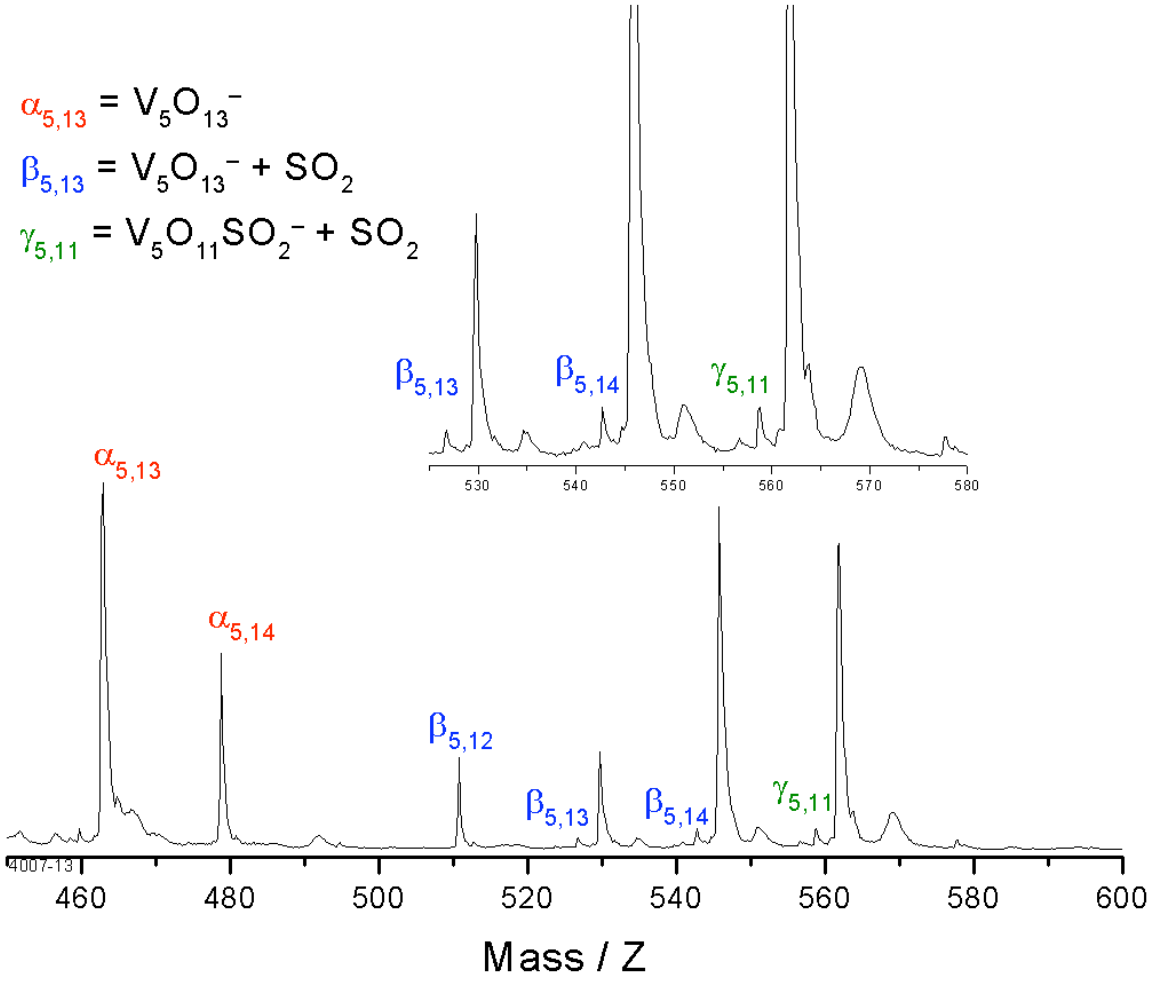

Figure 4-2. High resolution mass spectrum of $V_5O_x^-$ clusters after reaction with SO_2. The notation $\alpha_{m,n}$ correspond to the number of vanadium and oxygen atoms assigned to the cluster. For example, $\alpha_{5,13}$ stands for $V_5O_{13}^-$. Likewise, $\beta_{5,13}$ corresponds to the assignment of an SO_2 adsorbed to that cluster. Although not as reactive, the inset shows the weak product peak produced by the adsorption of SO_2 by the fully oxidized $V_5O_{13}^-$ and $V_5O_{14}^-$ as well as a peak attributed to the adsorption of a second SO_2. The clusters are produced with a 1.2% O_2 carrier gas mixture, su that the (5,11) and (5,12) have greatly reduced abundances as compared to Figure 4-1A-B.

Accompanying reactivity of the reduced clusters, new reactivity is found in the sudden activation of $V_4O_{11}^-$, cf. Figure 1A-B. This effect can also be observed in the high-resolution mass spectra displayed in Figure 4-3. While it is not at all surprising that $V_4O_{11}^-$ adsorbs an SO_2 molecule (see discussion), the interesting point is that adsorption is not observable until the percentage of oxygen in the carrier gas is reduced. The adsorption reaction has never been observed when the percentage of oxygen in the carrier gas is above 5% (O_2:He). Yet, when the percentage is reduced, weaker adsorption peaks can be observed for larger clusters as well. The bottom spectrum in Figure 4-4 shows higher mass clusters beginning at $V_4O_{10}^-$ and the results of the interaction with SO_2 (top). Two distinct observations can be made. First is that very weak adsorption peaks, β, can be observed and may be assigned as to imply all clusters adsorb SO_2. With the exception of $V_5O_{12}^-$, none of the clusters are completely converted to product, under these conditions. The second is the reversal in abundances for the clusters that contain an even number of vanadium atoms. Peaks that correspond to $(V_2O_5)_N^-$ are of greater intensity in top spectrum with respect to the clusters that are of $(V_2O_5)_NO^-$ stoichiometry. In the reference spectrum (bottom), $(V_2O_5)_NO^-$ is the more intense peak. The clusters that contain an odd number of vanadium atoms do not display this effect.

The intensity reversal of the $(V_2O_5)_N^-$ and $(V_2O_5)_NO^-$ peaks can only partially be accounted for by the process

$$(V_2O_5)_NO^- + SO_2 \longrightarrow (V_2O_5)_NSO_3^- ,$$

which is interpreted below as a peroxo to sulfato conversion. To fully account for the reversal. On needs a subsequent process (SO_3 elimination, See Below.)

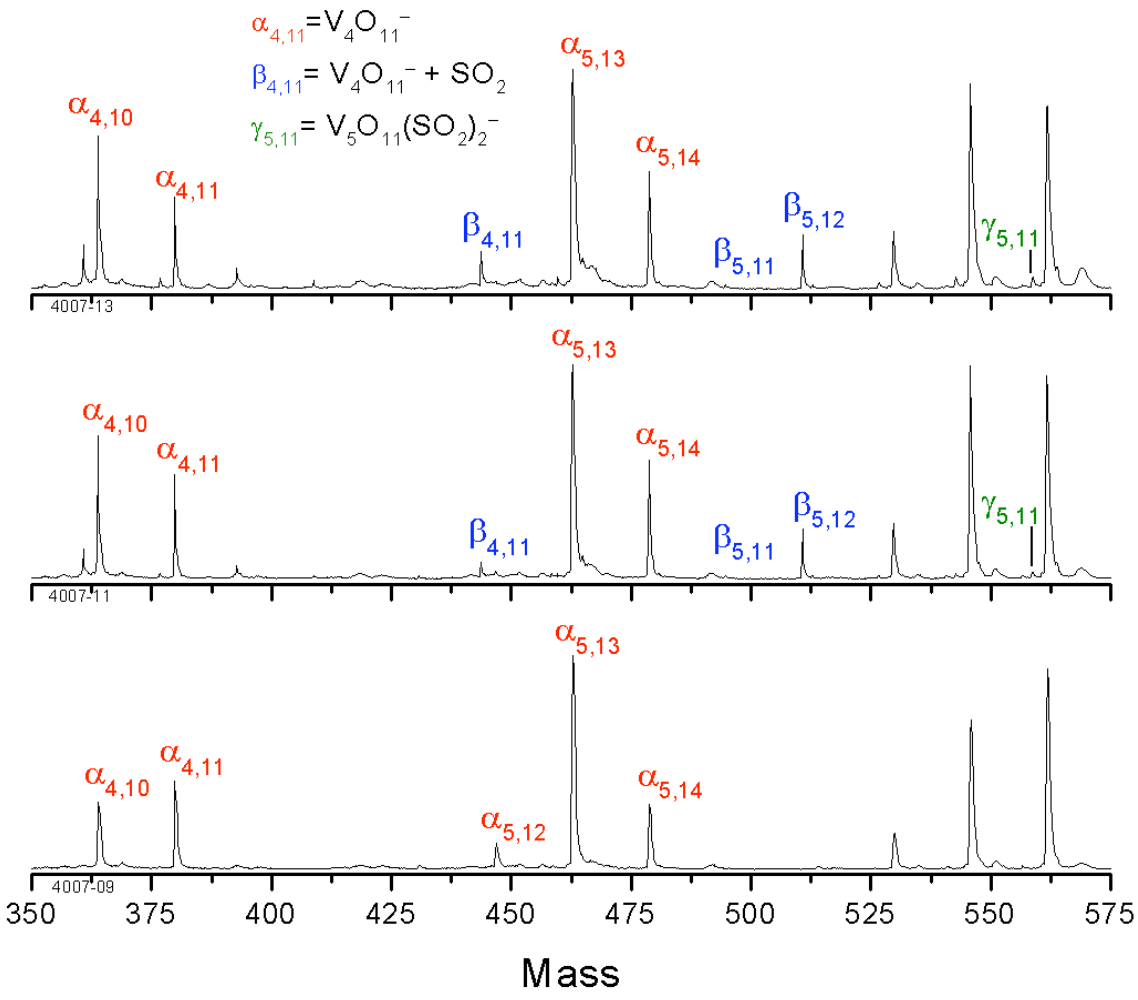

Figure 4-3. The reference and reacted spectra for the $V_4O_X^-$ and $V_5O_X^-$ clusters. A peak corresponding to the addition of SO_2 to $V_4O_{11}^-$ is noted by $\beta_{4,11}$. The change in intensities of $V_4O_{10}^-$ and $V_4O_{11}^-$ relative to each other is also observed when SO_2 is added (middle) and then the amount of SO_2 increased (top). The fully oxidized clusters $V_5O_{13}^-$ and $V_5O_{14}^-$ react very slowly with SO_2. The anions $V_5O_{11}^-$ and $V_5O_{12}^-$ are shown to react very quickly upon addition of SO_2 compared to the clusters that contain all fully oxidized vanadium atoms.

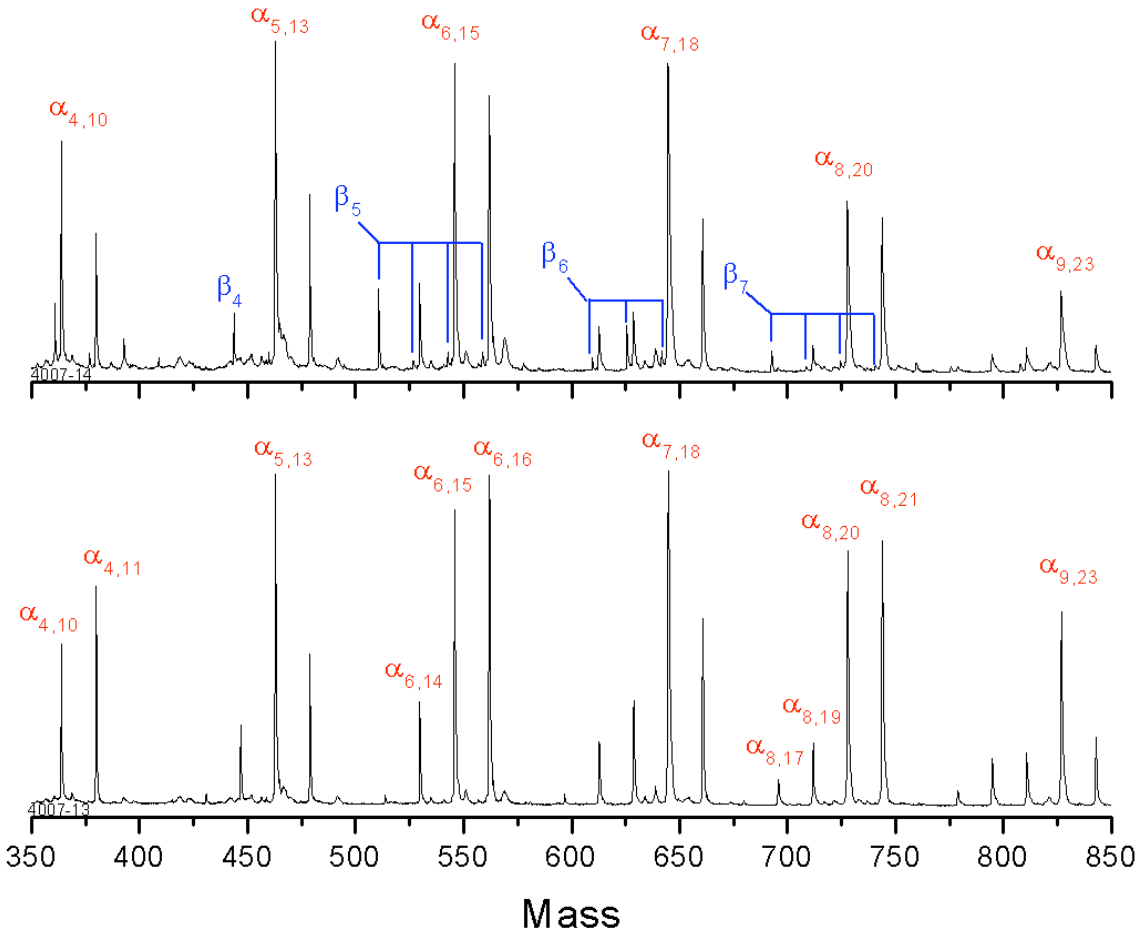

Figure 4-4. The mass spectrum of larger vanadium oxide anions. The anions are predicted be closed cage structures and very stable. The weak adsorption products for the fully oxidized clusters attest to this prediction. The Greek symbol, α, marks the unreacted clusters beginning at $V_4O_{10}^-$ and end with $V_9O_{23}^-$. The β_x signifies adsorption products where the subscript x signifies the number of vanadium atoms attributed to the peak.

Monovanadates. In contrast to the larger clusters, the reactivity of smaller clusters shows a behavior that is not as dependent on the oxidation state of the metal atoms of the cluster or oxygen content. The monovanadium oxide anions may hardly qualify as a cluster, but more as an anionic molecule. A single vanadium atom bonded to 3, 4, or 5 oxygen atoms can be detected having a single negative charge. Unlike the poly-vanadium oxide anions, monovanadium oxide anions composed of less than three oxygen atoms are not easily obtained. A reduction in the amount of oxygen content in the carrier gas does not yield anions that are oxidized less than VO_3^-, i.e. VO^- or VO_2^-. Instead only a shift in abundance to VO_3^- and loss of over the oxidized anions VO_4^- and VO_5^- is observed. This phenomena could be the direct result of a highly reactive VO^- or VO_2^- species. The laser ablation technique used to produced the clusters could provide ample time for these reduced species to interact with free molecular oxygen or other vanadium oxide molecules formed and are not detected by the mass spectrometer.

Figure 4-5 shows the results of the monovanadium oxide anions VO_3^-, VO_4^- and VO_5^- when interacted with SO_2. The bottom mass spectrum in Figure 4-5 shows the cluster abundances before addition of SO_2 to the flow tube reactor. The designation $\alpha_{m,n}$ denotes the formula for $V_mO_n^-$, i.e. $\alpha_{1,3}$ represents VO_3^-. The middle mass spectrum shows result when SO_2 is introduced into the flow tube reactor. The result when the amount of SO_2 is increased can be observed in the top mass spectrum.

It is easily observed that the anions VO_3^-, VO_4^- and VO_5^- all one adsorb SO_2 to generate as new anions VO_5S^-, VO_6S^- and VO_7S^-, labeled as $\beta_{1,3}$, $\beta_{1,4}$ and $\beta_{1,5}$, respectively. The adsorption reaction goes nearly to completion in the top mass spectrum

for all monovanadium oxide clusters. (The emergence of the $\beta_{1,3\text{-}5}$ peaks are verified by the ^{34}S isotope at +2 amu.)

Although additional measures were taken to remove water from the experiments shown in Figure 4-5 a trace amount of water is associated with VO_3^-. The peak is distinguished with an '*' and labeled as $\alpha^*_{1,3}$. The intensity of this anion is depleted as the amount SO_2 is increased downstream. The rate at which it is decreased is much less than that of the bare clusters, $\alpha_{1,3\text{-}5}$. Although a notable depletion is observed, a product peak is not observed. Similar peaks can be observed for $\alpha_{1,5}$ and do not appear to adsorb SO_2. Instead, it may be reasonable to assume the associated H_2O molecule is lost as a result of the adsorption. A more thorough investigation is discussed later in this chapter and again in Chapter V.

Divanadates. It is common to see the clusters ranging from $V_2O_5^-$ to $V_2O_7^-$ under nearly all oxygen percentages as shown in Figure 4-6. The $V_2O_X^-$ clusters with X< 5, such as $V_2O_3^-$ and $V_2O_4^-$, only appear with a drastic reduction in oxygen content. The reactivity of these clusters follows the trend for all other clusters in which the reactivity increases with a lower average oxidation state, Z, and the reaction goes toward completion with an increase in SO_2 partial pressure. As the composition of the vanadium oxide anions is changed by increasing the number of vanadium and oxygen atoms, the reactivity is noticeably changed.

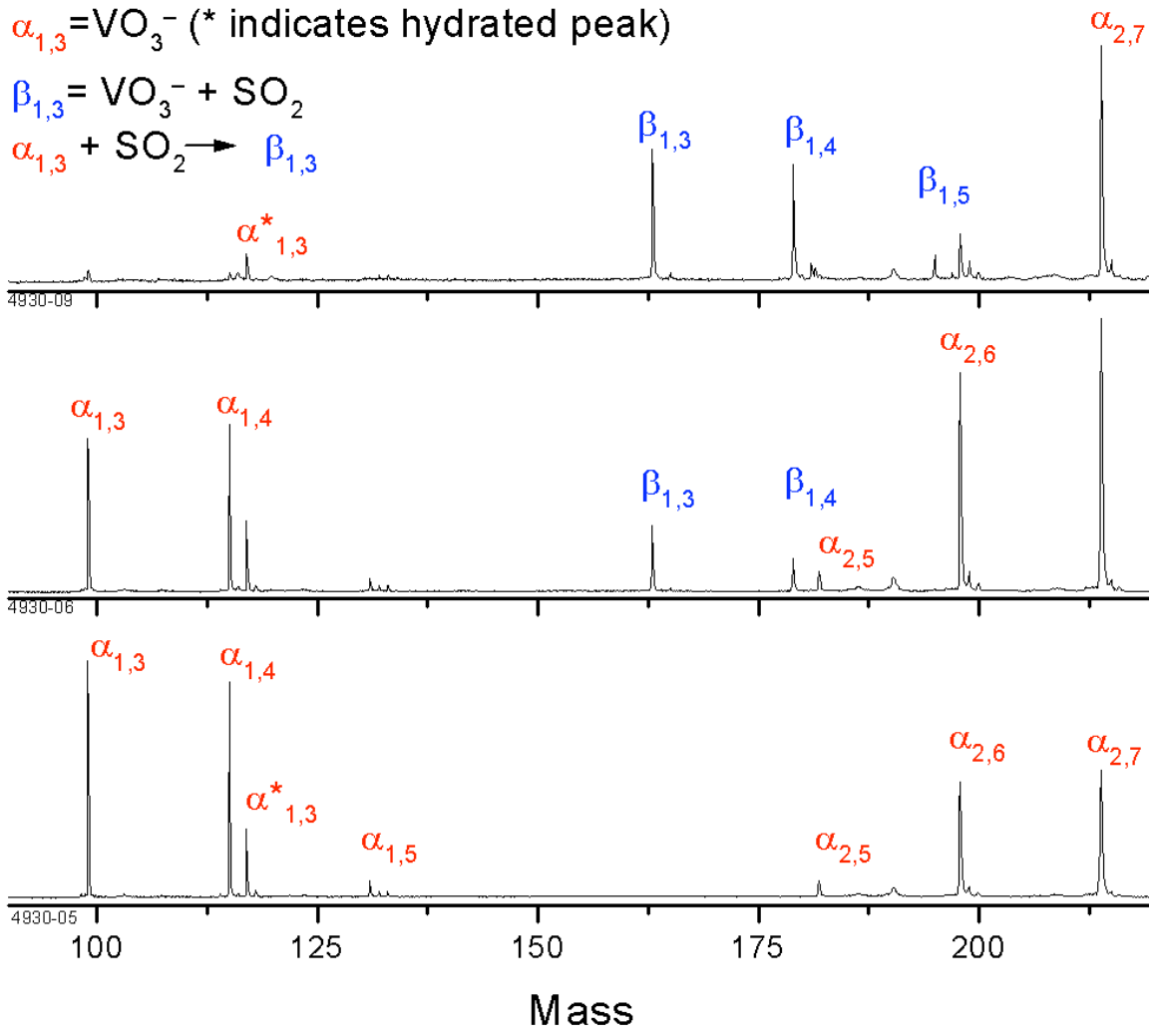

Figure 4-5. Mass spectra displaying monovanadium oxide anions, VO_3^-, VO_4^-, $H_2VO_4^-$, and VO_5^-. The notation $\alpha_{1,x}$ is used to signify VO_x^- and $\alpha^*_{1,x}$ is used to designate the hydrated $H_2VO_4^-$. The lower mass spectrum, the reference mass spectrum showing the abundances of the anions from VO_3^- to $V_2O_7^-$. The middle and top mass spectra show the results from addition of 5% SO_2 downstream to the flow reactor. The amount of SO_2 added to the flow reactor is increased from the middle to top mass spectra. The product peaks VO_5S^-, VO_6S^-, and VO_7S^- are identified by $\beta_{1,3}$, $\beta_{1,4}$, and $\beta_{1,5}$, respectively.

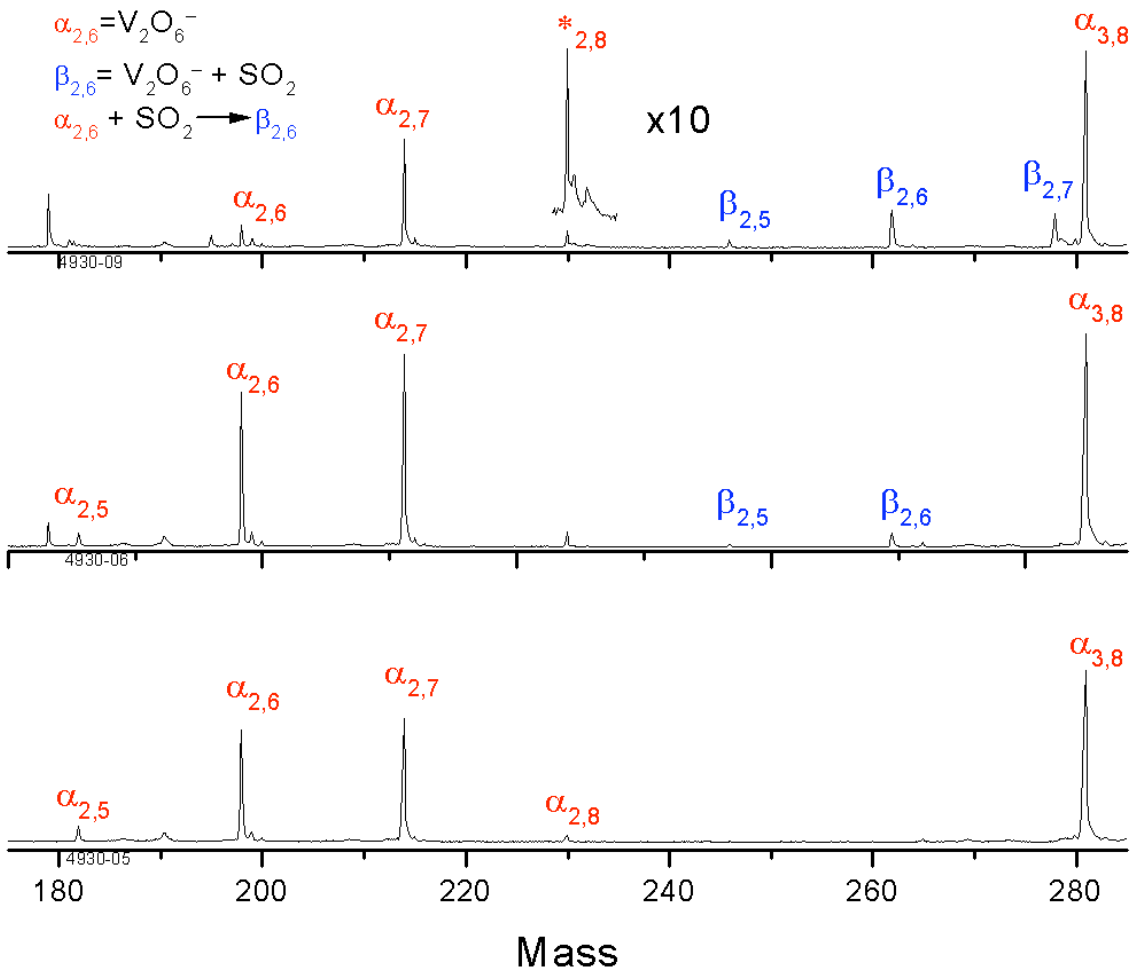

Figure 4-6. The di-vanadium oxide anions $V_2O_5^-$, $V_2O_6^-$, $V_2O_7^-$ and $V_2O_8^-$ are displayed (lower) along with the results after interaction with SO_2 (middle and top). The same notation is used as in previous figures where $\alpha_{2,6}$ and $\beta_{2,6}$ are the anions $V_2O_6^-$ and $V_2O_8S^-$, respectively. The partial pressure of SO_2 is increased going from the middle to top mass spectrum. The adsorption of SO_2 is easily justified by observing the decrease in the reactant peaks and the appearance of the new peaks. The enhancement of the peak corresponding to $V_2O_8^-$ is accompanied by an additional peak at +2 amu. This can be seen in the inset which is an x10 magnification. The sudden appearance of this peak may be attributed to the natural isotope of sulfur, ^{34}S.

A very interesting phenomenon occurs pertaining to the peak that corresponds to $V_2O_8^-$. As the amount of SO_2 is increased, the peak at 230 amu is enhanced as well as a peak at 232 amu observed in the inset. The intensities of the peaks at 230 and 232 are indicative of the isotopic distribution of sulfur. With the incorporation of a sulfur atom into the cluster, various possibilities arise. The most obvious would be adsorption of SO_2 by $V_2O_4^-$, but $V_2O_4^-$ is not present initially in the reference mass spectrum. This implies $V_2O_4^-$ would have to be a product of the interaction with SO_2 and O_2. The adsorption of a second SO_2 molecule is observed for $V_2O_6^-$ in Figure 4-6 (top), indicated by $\gamma_{2,6}$, and not in the results at the lower SO_2 concentration (middle). It is possible that the peak at 230 amu is produced by way of an catalytic process in which all the products are not observed.

Trivanadates. Figure 4-7 shows a continued trend of decreased reactivity for the tri-vanadium oxide anions. The anions $V_3O_8^-$ and $V_3O_9^-$ do not appear to adsorb SO_2 as quickly as the di-vanadium oxide anions as can be seen in Figure 4-6.

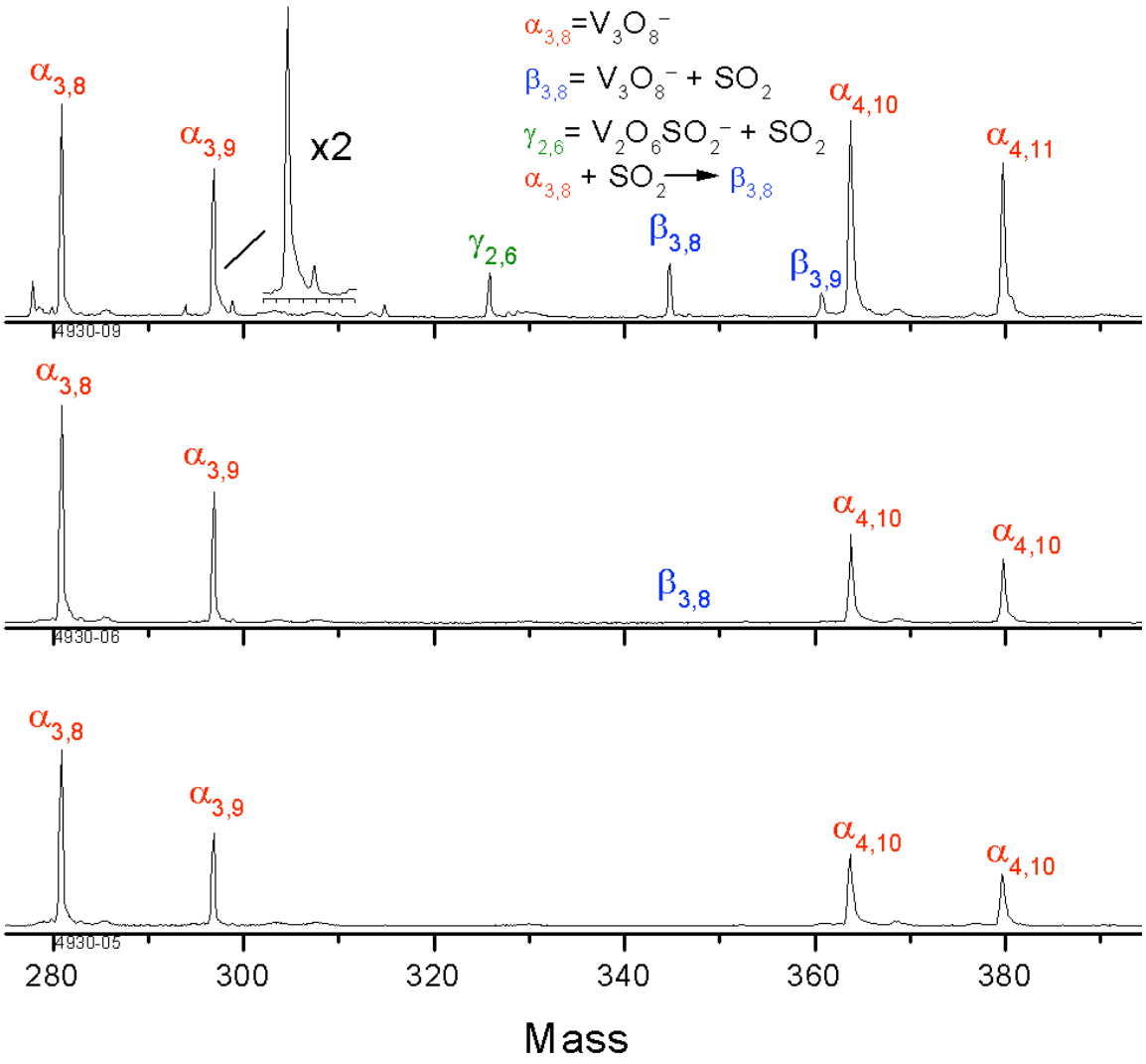

Figure 4-7. The reference mass spectra of trivanadium oxide anions is shown in the lower mass spectrum. The results of addition of SO_2 to the flow reactor can be observed in the middle and top mass spectra, where the top mass spectrum has the highest amount of SO_2 added. The α–β notation is consistent with the notation in Figures 4-1 and 4-2. The peak noted as $\gamma_{2,6}$ corresponds to an additional pick up of a second SO_2 by $V_2O_6^-$.

At higher oxygen mixtures in the buffer has, > 2%, the clusters $V_3O_8^-$ and $V_3O_9^-$ are less reactive toward SO_2. Using a helium oxygen mixture that contains greater than 2% oxygen, $V_3O_{10}^-$ can be produced. However, $V_3O_{10}^-$ has been observed to be inactive in any observable adsorption process. But when the oxygen content is reduced, the clusters become reactive, as is the case for $V_4O_X^-$ and $V_5O_X^-$. Accompanying this reduction is the loss of $V_3O_{10}^-$ and the appearance of new clusters containing fewer numbers of oxygen. As discussed in chapter II, the $V_3O_x^-$ clusters are the exception to the five-fold pattern observed in the mass spectrum. The reactivity of the these clusters ranging from $V_3O_6^-$ to $V_3O_9^-$ have been shown to adsorb up to 2 SO_2 molecules, as shown in Scheme 2, with decreased oxygen content in the carrier gas. In the case of $V_3O_7^-$, a third SO_2 is added at higher partial pressures of SO_2 in the FTR. Oddly, anions corresponding to $V_3O_7^-$ adsorbing multiple SO_2 molecules have been observed even when it is not present in the reference spectrum. The appearance of this peak is possible by either fragmentation of a larger cluster, or etching of oxygen atoms by SO_2 producing SO_3. The distinction of multiple SO_2 addition may be a characteristic of the transition from a closed ring structure to a chain structure.

$$V_3O_6^- + SO_2 \longrightarrow V_3O_6(SO_2)^- \xrightarrow{SO_2} V_3O_6(SO_2)_2^-$$
$$V_3O_7^- + SO_2 \longrightarrow V_3O_7(SO_2)^- \xrightarrow{SO_2} V_3O_7(SO_2)_2^-$$
$$V_3O_8^- + SO_2 \longrightarrow V_3O_8(SO_2)^- \xrightarrow{SO_2} V_3O_8(SO_2)_2^-$$
$$V_3O_9^- + SO_2 \longrightarrow V_3O_9(SO_2)^- \xrightarrow{SO_2} V_3O_8(SO_2)_2^-$$

Scheme 2

Figure 4-8 presents an overall view of the relative reactivity of the clusters discussed.

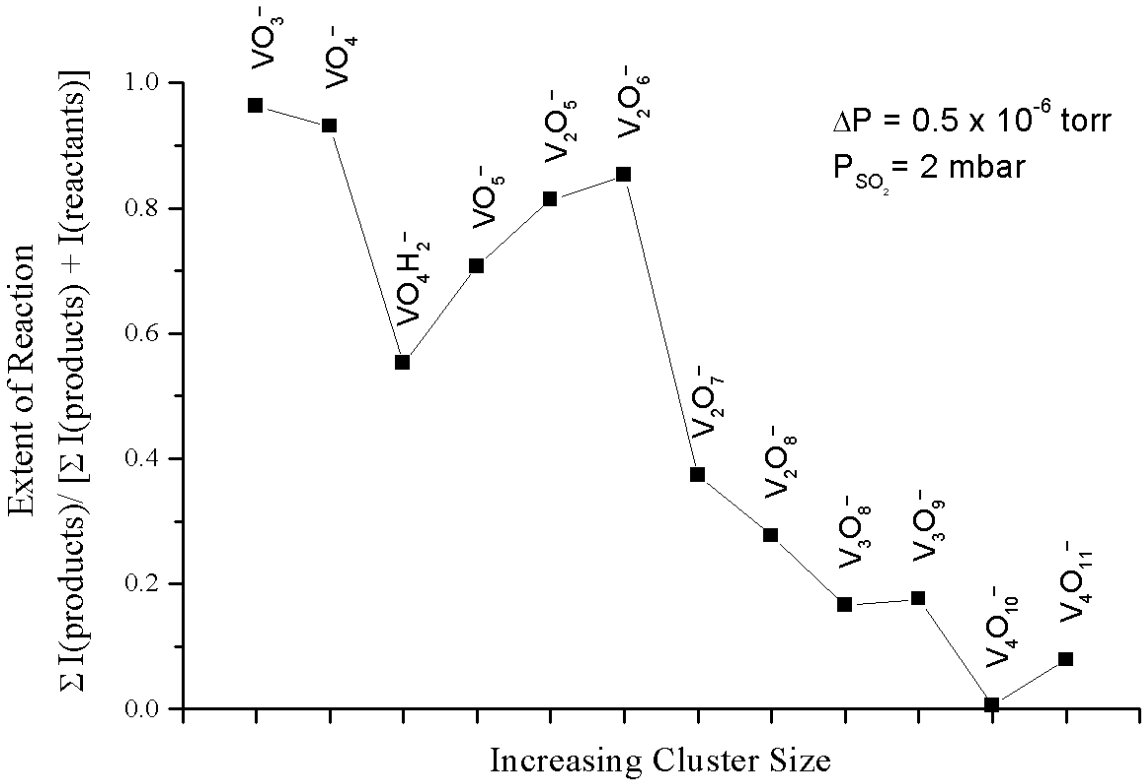

Figure 4-8. An overall view of the extent of reaction for vanadium oxide clusters generated from VO_3^- to $V_4O_{11}^-$. The reactivity decreases as cluster size increases for vanadium oxide anions with an average oxidation state of +5 for the vanadium atoms.

4.3.4 Pressure Dependent Reactions.

Partial Pressure of SO_2 (P_{SO_2}). The adsorption reactions described above were studied as a function of the partial pressure of SO_2. The experiment is discussed in detail in Chapter 2.2.3. Briefly, the amount of SO_2 added downstream was estimated as a

function of the contribution made to rise in total chamber by the reaction valve. This contribution is controlled by the length of the gas pulse delivered. An increased length from 180μs to 190μs provides a notable increase in the chamber pressure. The actual contribution to the rise in chamber pressure is also dependent on the stagnation pressure behind the reaction valve.

Total Reactor Pressure. The decrease in volume of the reactor, leads to the increase in total pressure. By using the smaller volume reactors discussed in Chapter 2.2.3, the pressure can be increased appreciably. In the case of the 560 mm^3 (or cmm) brass reactor, the pressure is increase to nearly 0.3 mbar. With the decrease in volume to 400 cmm, the pressure in the reactor is increased to approximately 0.4 mbar. The impact this inclined pressure, as shown in Figures 4-9 through 4-10, has on the adsorption reactions between SO_2 and $V_NO_M^-$ is interesting. The extent of reaction plot in Figure 4-9 displays the extent of reaction $V_5O_{12}^-$ with SO_2 versus the calculated partial pressure of SO_2 in the FTR. The plot shows the progression of reactions under three different pressures as the calculated partial pressure of SO_2 is increased. The reactions are done in each of the three FTRs. The progression of each reaction is slower as a total pressure is decreased.

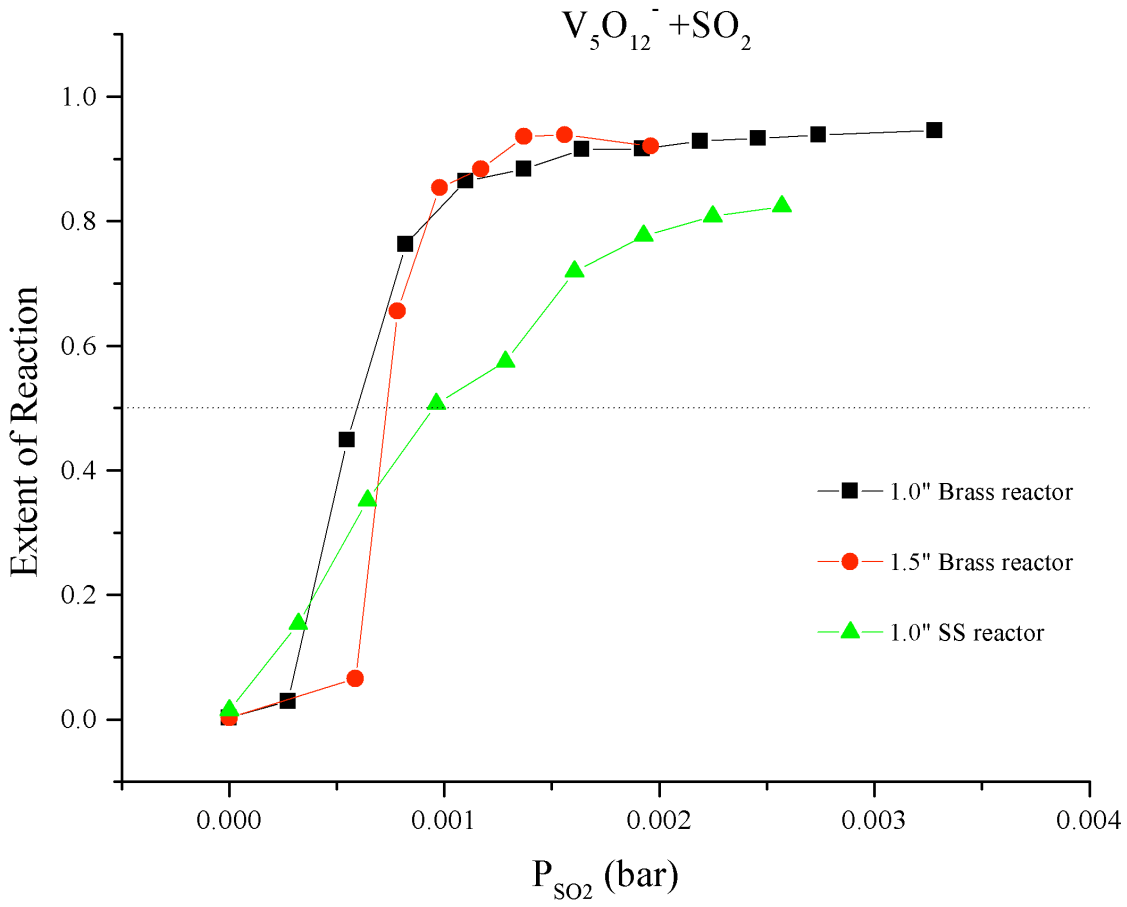

Figure 4-9. The extent of reaction of $V_5O_{12}^-$ with SO_2 in different FTRs. The total pressure is different for each reactor. The reactor pressures are 0.4 mbar, 0.3 mbar and 0.2 mbar for the 1.0" brass reactor, the 1.5" brass reactor, and the 1.0" stainless steel reactor, respectively. As the total pressure is increased the extent of reaction occurs more readily at lower partial pressures as noted by the point at which the extent of reaction crosses the 0.5 point.

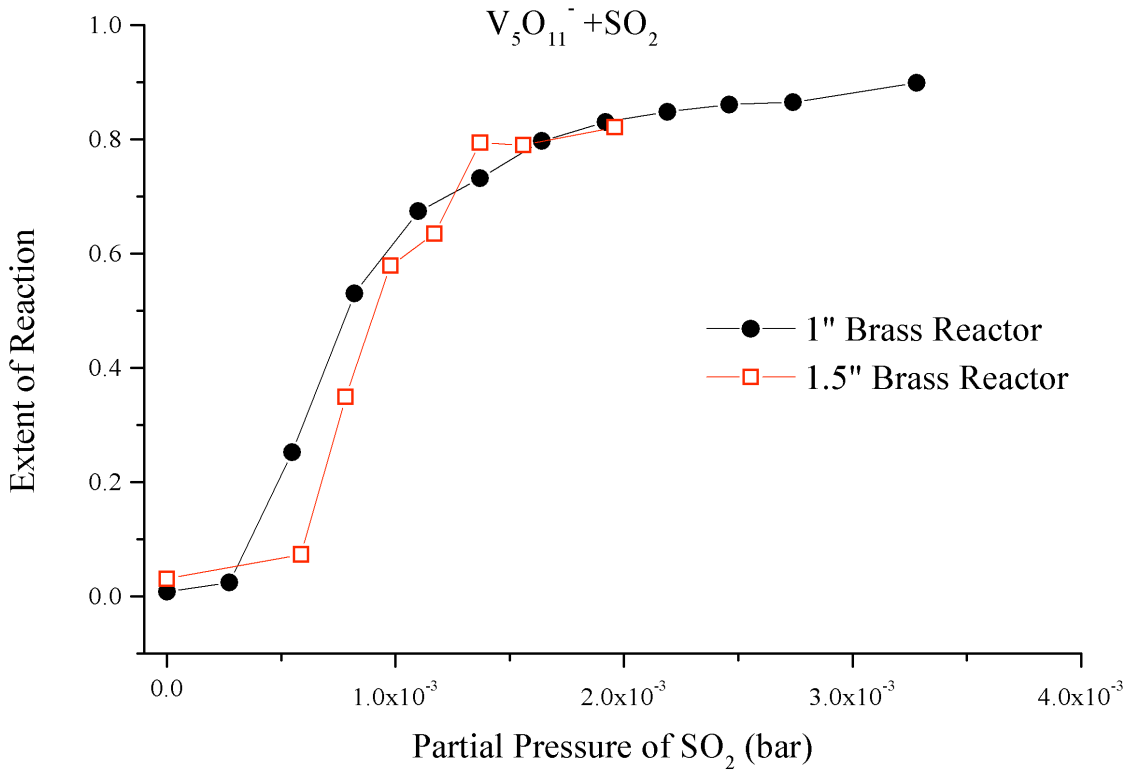

Figure 4-10. Extent of reaction of $V_5O_{11}^-$ as a function of partial pressure of SO_2 in two different FTRs, the 1" and 1.5" brass reactors. The FTRs have volumes of 400 cmm and 560 cmm, respectively.

The results in Figure 4-10 are from the reaction of SO_2 with $V_5O_{13}^-$. The data plotted in Figure 4-11 is not only at different total pressures, it is also at two different reaction times. The data is taken from the 1" (400 mm^3) and 1.5" (560 mm^3) brass FTRs. The longer reaction time has no effect on the reaction progression nor does the reactor pressure. This behavior is evident of an equilibrium reaction. The surface of the cluster may not have any defect sites, which may suggest it has no active sites. The absence of an active site does not mean the SO_2 is unable to absorb to the cluster, but at much higher energy barrier may exist.

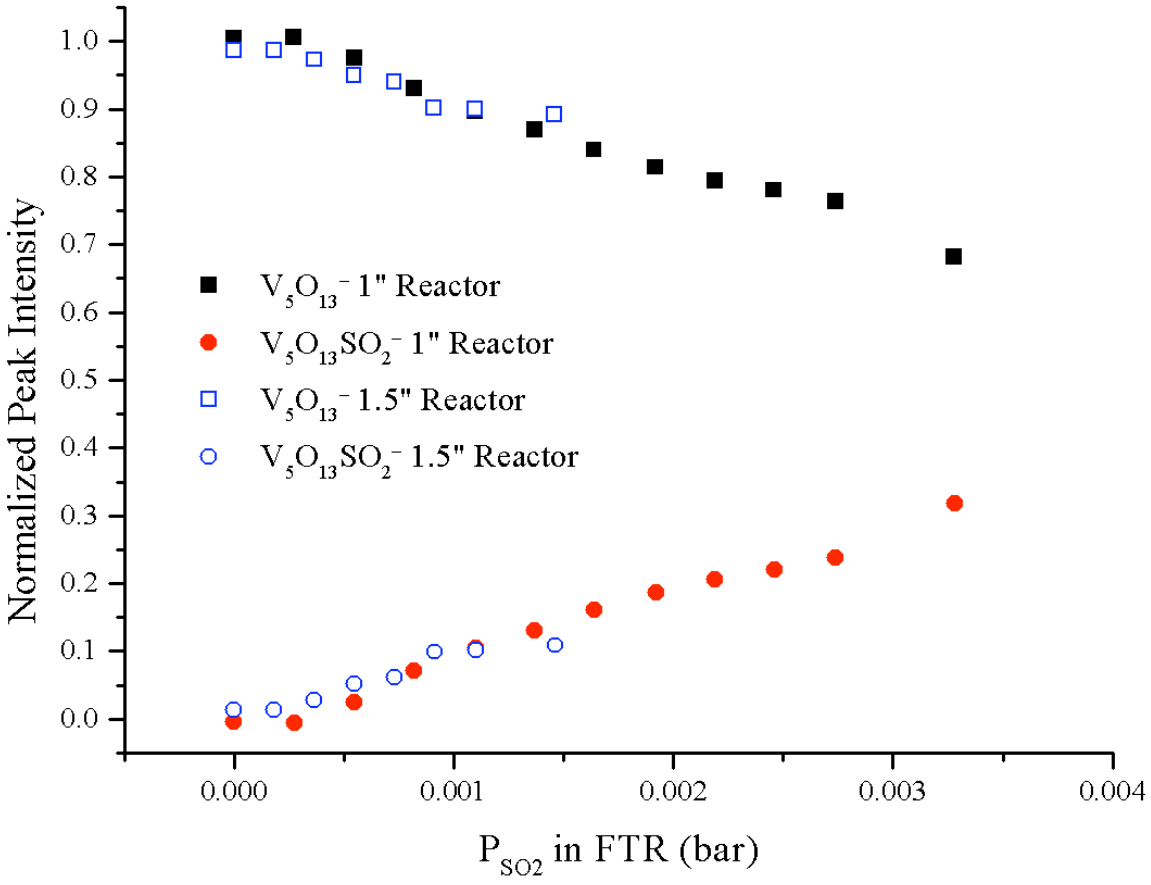

Figure 4-11. Reaction of $V_5O_{13}^-$ with SO_2 in the higher pressure brass reactors. There is no change in the reaction as the reaction time is increased in the 1.5" reactor suggesting the reaction is in equilibrium.

Figures 4-12 through 4-15 show the effect on the adsorption of SO_2 on the clusters $V_4O_{10}^-$, $V_4O_{11}^-$, $V_5O_{11}^-$ and $V_5O_{12}^-$. As expected, the product peak rises with increased SO_2 as the parent peak decreases. In the cases of $V_4O_{10}^-$, $V_5O_{11}^-$ and $V_5O_{12}^-$, a second SO_2 is adsorbed. For these cases, the product peaks of $V_4O_{10}SO_2^-$, $V_5O_{11}SO_2^-$ and $V_5O_{12}SO_2^-$ decay as they second SO_2 is adsorbed. In order to demonstrate the increase in products of $V_4O_{10}SO_2^-$, $V_5O_{11}SO_2^-$ and $V_5O_{12}SO_2^-$ the peaks were calculated as the inverse of the depletion of the parent cluster peak. This is signified by the open circles in Figures 4-12, 4-13 & 4-14.

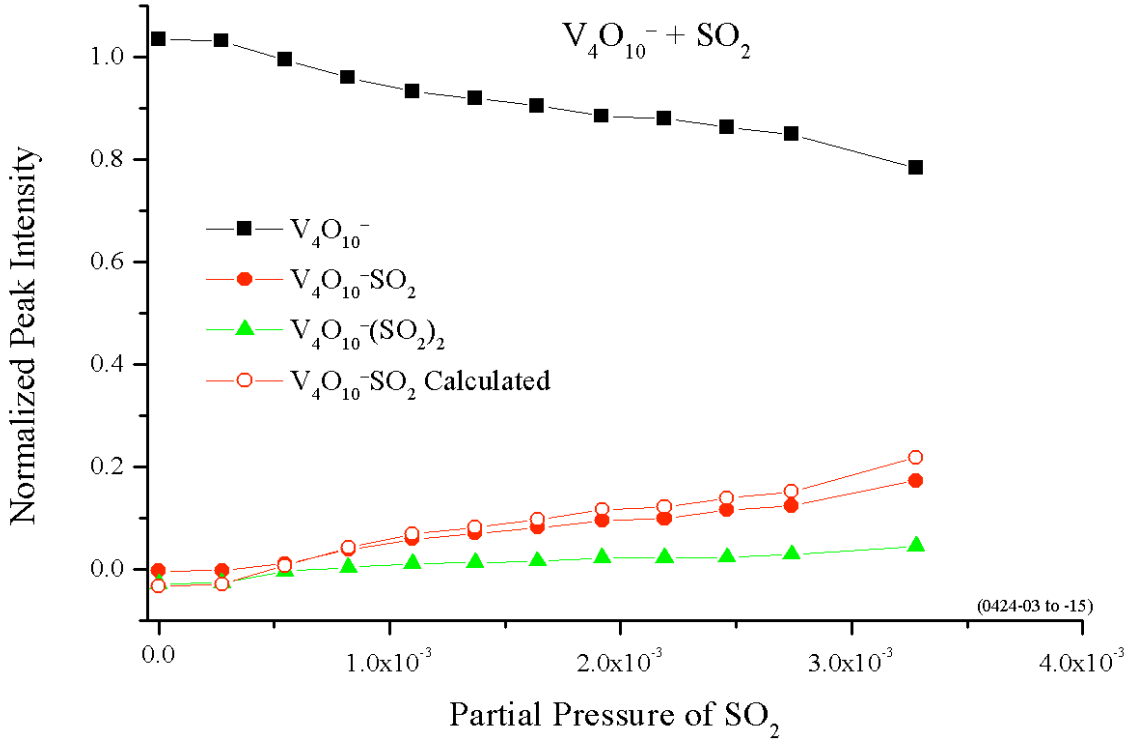

Figure 4-12. Addition of SO_2 to $V_4O_{10}^-$ as a function of the partial pressure of SO_2. As indicated by the legend, the squares indicate the peak intensity of the parent peak, $V_4O_{10}^-$. The filled circles and the triangles represent the product peaks $V_4O_{10}SO_2^-$ and $V_4O_{10}^-(SO_2)_2^-$, respectively. The open circles represent the calculated increase of the product peak $V_4O_{10}SO_2^-$.

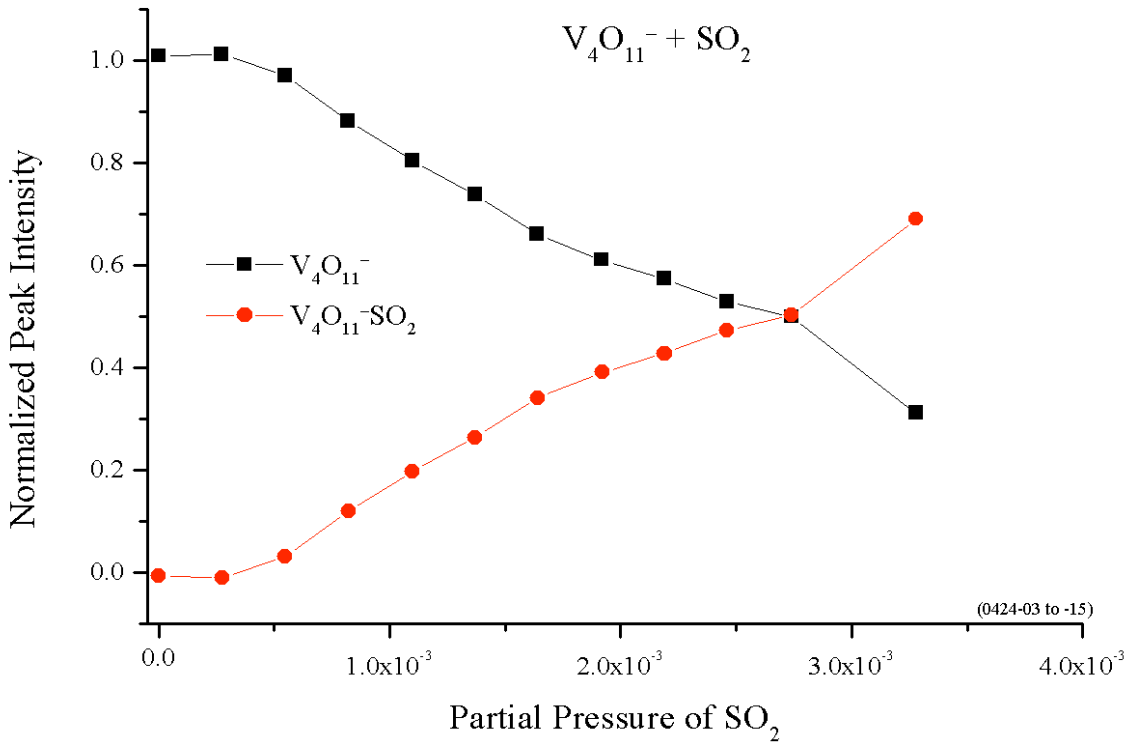

Figure 4-13. Addition of SO_2 to $V_4O_{11}^-$ as a function of the partial pressure of SO_2. As indicated by the legend, the squares indicate the peak intensity of the parent peak, $V_4O_{11}^-$. The filled circles represent the product peaks $V_4O_{11}SO_2^-$.

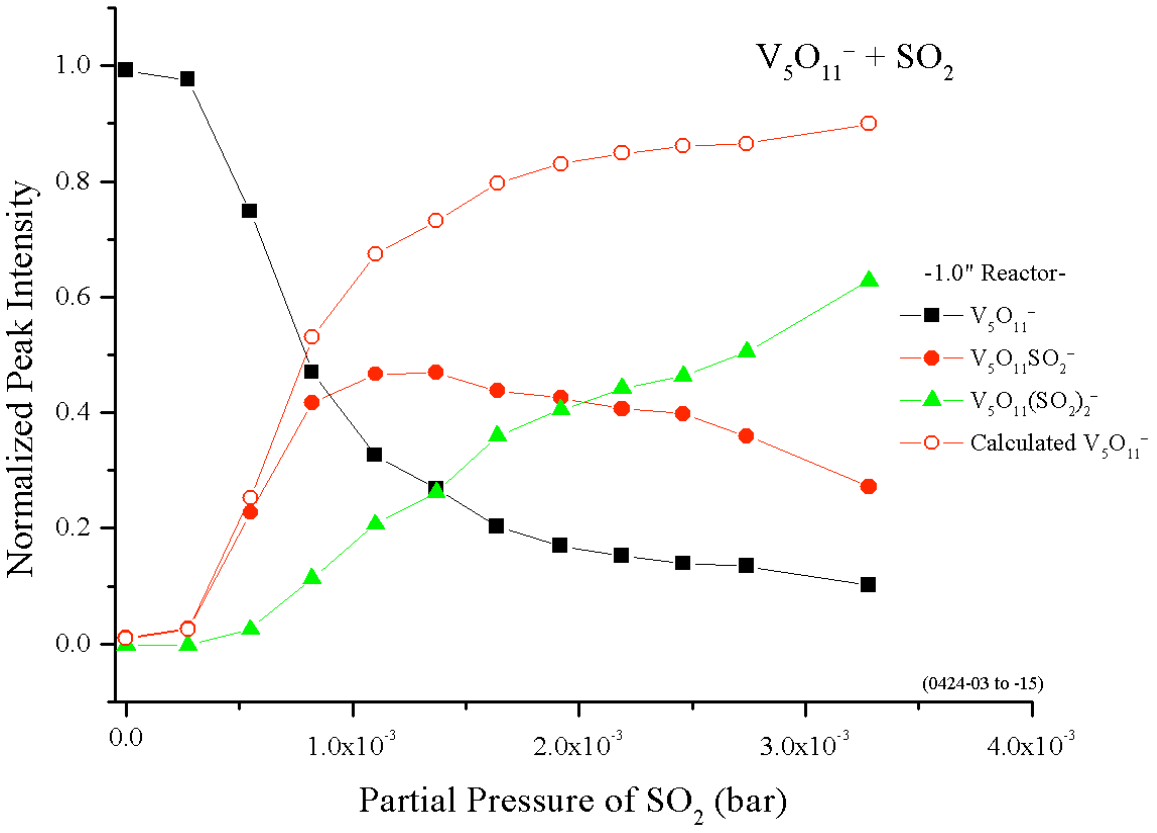

Figure 4-14. Addition of SO_2 to $V_5O_{11}^-$ as a function of the partial pressure of SO_2. As indicated by the legend, the squares indicate the peak intensity of the parent peak, $V_5O_{12}^-$. The filled circles and the triangles represent the product peaks $V_5O_{11}SO_2^-$ and $V_5O_{11}(SO_2)_2^-$, respectively. The open circles represent the calculated increase of the product peak $V_5O_{11}SO_2^-$.

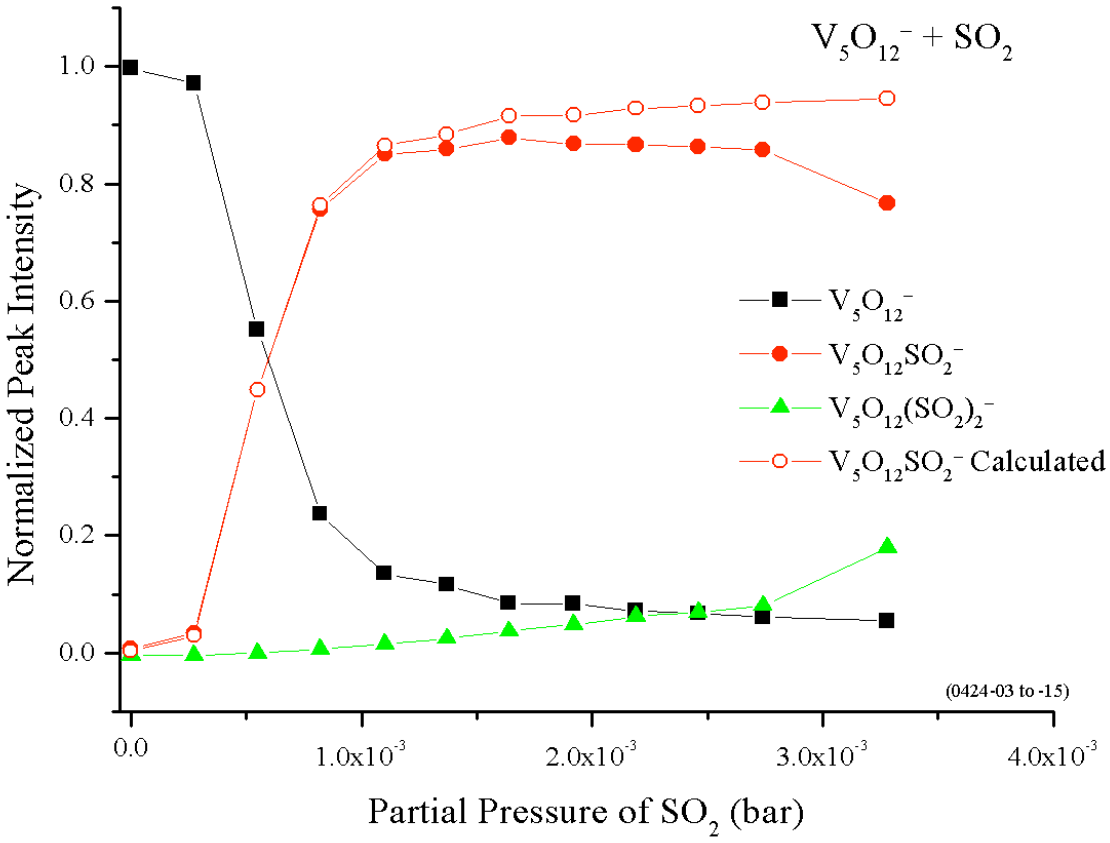

Figure 4-15. Addition of SO_2 to $V_5O_{12}^-$ as a function of the partial pressure of SO_2. As indicated by the legend, the squares indicate the peak intensity of the parent peak, $V_5O_{12}^-$. The filled circles and the triangles represent the product peaks $V_5O_{12}SO_2^-$ and $V_5O_{12}(SO_2)_2^-$, respectively. The open circles represent the calculated increase of the product peak $V_5O_{12}SO_2^-$.

Figure 4-11 shows the extent of reaction for the reaction of SO_2 with $V_5O_{12}^-$ as a function of the partial pressure. The extent of reaction is calculated from the integrated peak intensities of $V_5O_{12}^-$ and $V_5O_{12}SO_2^-$. The formula is shown in equation 4.1.

$$\text{Extent of Reaction} = \frac{I(V_5O_{12}SO_2^-)}{I(V_5O_{12}^-) + I(V_5O_{12}SO_2^-)} \tag{4.1}$$

The plot in Figure 4-11 shows the an increase in the product peak of the reaction as the partial pressure of SO_2 is increased. It is not apparent whether the reaction is in equilibrium or kinetic control.

4.4 Discussion.

In comparison of the clusters with even and odd numbers of vanadium atoms, it is easy to understand the difference between them. Determining the composition of clusters with an even number of vanadium atoms for the fully oxidized V_2O_5 stoichiometry. These structures are even easily assigned as geometric cages and assemble nicely. The clusters with an odd number of vanadium atoms are not as convenient to determine. The stoichiometry is not trivial yielding 2.5 oxygen atoms from the V_2O_5 ratio. Also, trying to assign a closed structure as either a ring or a cage is not easily accomplished with out breaking the composition or overall charge. In the case of the even clusters, the addition of the extra oxygen atom can be accomplished by easily replacing a vanadyl unit V=O, with a peroxo ligand.[40] This isn't as easily accomplished with odd clusters for two reasons. First, no predicted structures have been calculated or reported for clusters

containing an odd number of vanadium atoms of 5 or more. This is not surprising considering the second reason: When considering possible structures for these clusters it is not possible to add one more oxygen and not break bonding rules or alter the overall charge state of the cluster. This structural consideration helps explain why a switch in the abundances is observed for the even number clusters and not for the odd clusters. An adsorption is most likely to occur at the peroxo group. However, all the clusters that supposedly contain this ligand do not completely react with SO_2. This could be for many reasons. One is the reaction conditions are not such as to cause absolute depletion. For example, the partial pressure of SO_2 is not high enough. Another may be the clusters showing adsorption are only a minor fraction of the total for a given composition, i.e. there are other non reactive isomers present. A third possibility is that catalytic oxidation is occurring and regeneration of the catalytically active species is occurring more rapidly when a higher amount of oxygen is present. The regeneration step would be slower when there is a lower amount of free oxygen available, and an adsorption product is observed.

4.4.1 Null Reactivity of Larger Z = 5 Clusters.

This null result for experiments with the gases mentioned above is quite surprising at first, especially in the case of SO_2. The use of vanadium pentoxide, V_2O_5, as a catalyst in SO_3 production is well known.[2] Extensive research has been done and reported in references.[5-7] It has been concluded that two independent cycles occur during catalysis: oxidation of SO_2 to SO_3 and redox of the vanadium oxide catalyst.[11] A +4 vanadium state is was identified as the deactivating state.[8] Although, the active state is considered to be the +5 oxidation state, optimal conditions are in a minimum of the V^{+5}-O_2 phase diagram. In this region a mixture of partially oxidized vanadium oxides exist.

The active vanadium oxide forms a complex with the SO_2 that is highly negative and stabilized with counter ions. Therefore, the null reaction between the vanadium oxide anion clusters in Figure 4-1 and SO_2 is not surprising if the cluster anions are accepted as having all vanadium atoms in the +5 oxidation state.

Considering the predictions that these clusters are ultra stable energetically and structurally. The high symmetry may also prevent the vanadium oxide clusters from having localized defects at a metal. It is agreed upon that the oxidation state of the vanadium atom is a key element of the catalytic cycle. In turn, the defect free, fully oxidized clusters should be inert. When deprived of oxygen, defect sites on the clusters are formed at specific sites and the clusters are found to be much more reactive toward SO_2.

4.4.2 Addition of SO_2 to Z<5 Clusters.

The addition of only one SO_2 to $V_5O_{12}^-$, coupled with the null reaction of $V_5O_{13}^-$, suggests that the removal of one oxygen atom from $V_5O_{13}^-$ opens a single active or absorption site on $V_5O_{12}^-$. Likewise the removal of the second oxygen atom to form $V_5O_{11}^-$ allows the addition of the second SO_2 by introducing a second defect site. This would imply the structures $V_5O_{11}^-$ and $V_5O_{12}^-$ are similar to that of $V_5O_{13}^-$. The idea of removing oxygen atoms to motivate adsorption ends with $V_5O_{10}^-$. Since this cluster has only been observed to adsorb one SO_2 this cluster may not have the same structure and electronic configuration as the other three clusters. It is important to note the 'removal' of oxygen is the result of the lack of oxygen during cluster formation. The idea of removing an oxygen atom does *not* involve a process in which an oxygen atom is

physically removed from a cluster. For example, removing an oxygen atom from $V_5O_{12}^-$ to form $V_5O_{11}^-$ is a not occurring. The cluster $V_5O_{11}^-$ is assumed to be formed as $V_5O_{11}^-$ and not some larger cluster that is then fragmented into $V_5O_{11}^-$. The idea of 'removal' is used to speculate that the structures of $V_5O_{11}^-$, $V_5O_{12}^-$ and $V_5O_{13}^-$.

To further justify the idea of a caged structure for these larger clusters with the Z > +4, the stoichiometry and likely structures resemble those of the polyoxometallate polyanions. Experimental results, mentioned in chapter 3, for $V_5O_{14}^{3-}$ reveal a caged structure.[36] Similar cage structures have been observed in DFT studies and are discussed in Chapters 5 and 7. The non-existence of multiple absorption sites for $V_5O_{10}^-$ may suggest a transition from a three dimensional structure to a two dimensional structure such as a ring or a chain. It could also be argued that the depletion of oxygen could also bring about some structural rearrangement involving existing oxygen atoms that could inhibit adsorption and still maintain a three dimensional cage with the resulting structure that only possess a single active site. The issue can not be resolved with the data at hand. A more revealing theoretical study coupled with additional experimental information would be more conclusive.

The (4,11) cluster is observed to be inactive in prior studies when the seeded buffer gas contains more than 5% O_2:He. It is possible this cluster undergoes a structural change under these less oxidative conditions. $V_4O_{11}^-$ is predicted to have a very reactive superoxo, O_2^-, group bound to a vanadium atom. It is surprising this cluster is not reactive toward SO_2 under fully oxidizing conditions. $V_4O_{10}^-$, which is very similar in structure to P_4O_{10}, has other isomeric structures at 0.5 eV higher than the lowest

tetrahedral cage structure. This is predicted in the DFT calculations of Vyboischikov and Sauer. One can only speculate similar structures for $V_4O_{11}^-$ may also exist. The decrease in oxygen content may allow these isomers to form. The sudden turn on in reactivity may be due to a few possibilities. The first is that other isomers of $V_4O_{11}^-$ are being formed. Isomeric forms have been explored in theoretical investigations. [39,40] The studies showed only a small difference in absolute energies, < 0.5 eV. It is feasible that the structures formed are more disperse at lower oxygen content. The other possibility, which is shown in Scheme 3, is that the additional SO_2 interacts with the adsorbate on the cluster. This reactive oxidation generates an SO_3 molecule. This could possibly open a reaction channel for a second SO_2 to be oxidized and desorbed, leaving the cluster as $V_4O_9^-$. This could even then adsorb an O_2 molecule and result in this regeneration of $V_4O_{11}^-$.

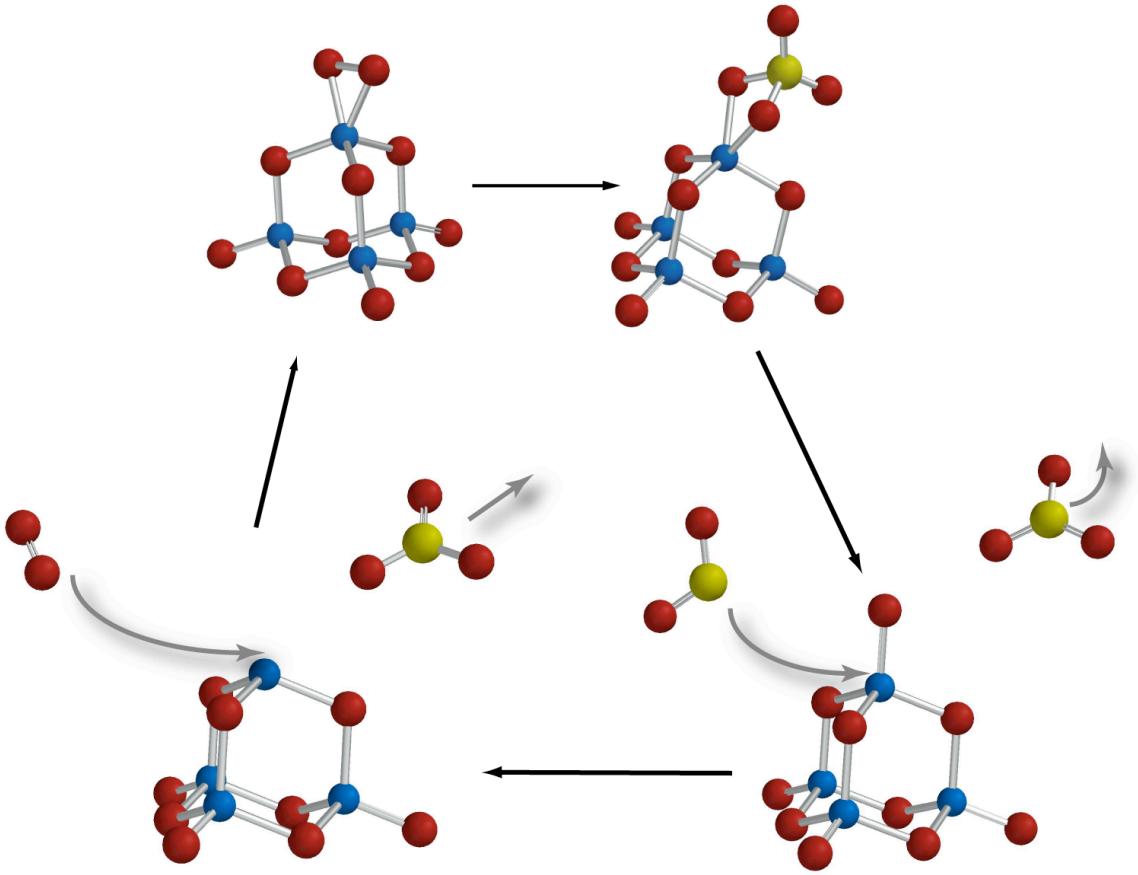

Scheme 3

The comparison of the clusters with an even and odd numbers of vanadium atoms, can explain the differences between them. Determining the composition of clusters with an even number of vanadium atoms for the fully oxidized V_2O_5 stoichiometry is simple to predict as any multiple of V_2O_5. These structures are even easily assigned as geometric cages and assemble nicely. The clusters with an odd number of vanadium atoms are more complicated to determine. The stoichiometry is not trivial yielding 2.5 oxygen atoms from the V_2O_5 ratio. Also, trying to assign a closed structure as either a ring or a cage is not easily accomplished with out breaking the composition or overall charge. In

the case of the even clusters, the addition of the extra oxygen atom can be accomplished by replacing a vanadyl unit V=O, with a peroxo ligand.[40] This isn't as easily accomplished with odd clusters for two reasons. First, no predicted structures have been calculated or reported for clusters containing an odd number of vanadium atoms of 5 or more. The second reason is when considering possible structures for these clusters it is not possible to add one more oxygen to a predicted structure and not break bonding rules or alter the overall charge state of the cluster. This structural consideration helps explain why a switch in the abundances is observed for the even number clusters and not for the odd clusters. An adsorption is most likely to occur at the peroxo group. However, all the clusters that supposedly contain this ligand do not completely react with SO_2. This could be for many reasons. One is the reaction conditions are not such as to cause absolute depletion. For example, the partial pressure of SO_2 is not high enough. Another may be the clusters showing adsorption are only a minor fraction of the total for a given composition, i.e. there are other non reactive isomers present. A third possibility is that catalytic oxidation is occurring and regeneration of the catalytically active species is occurring more rapidly when a higher amount of oxygen is present. The regeneration step would be slower when there is a lower amount of free oxygen available, and an adsorption product is observed.

In contrast to the larger clusters, the reactivity of smaller clusters shows a behavior that is not as dependent on the oxidation state of the metal atoms of the cluster or oxygen content. The monovanadium oxide anions may hardly qualify as a cluster, but more as an anionic molecule. A single vanadium atom bonded to 3, 4, or 5 oxygen atoms can be detected having a single negative charge. Unlike the poly-vanadium oxide

anions, monovanadium oxide anions composed of less than three oxygen atoms are not easily obtained. A reduction in the amount of oxygen content in the carrier gas does not yield anions that are oxidized less than VO_3^-, i.e. VO^- or VO_2^-. Instead only a shift in abundance to VO_3^- and loss of over the oxidized anions VO_4^- and VO_5^- is observed. This phenomena could be the direct result of a highly reactive VO^- or VO_2^- species. The laser ablation technique used to produced the clusters could provide ample time for these reduced species to interact with free molecular oxygen or other vanadium oxide molecules formed and are not detected by the mass spectrometer.

The extent of reactions for the clusters from VO_3^- to $V_4O_{11}^-$ with 2.0×10^{-3} bar of SO_2 added to the flow tube reactor. With in each set of anions there is an decline in reactivity as the number of oxygen atoms is increased. Overall, the activity is decreased as the number of vanadium atoms is increased. One can speculate why this may be occurring. The idea that at the smallest sizes, VO_X^-, a stable structure is formed with more accessible active sites. As the dimensionality is increased, the adsorption sites become sterically inaccessible and few in number. This would ultimately lower the probability that an SO_2 molecule will find an adsorption site. Another consideration is as the clusters grow larger, they are forming the stable cages that are predicted by DFT studies. If the cages are as stable as predicted, the SO_2 adsorption may be unfavorable and not observed.

4.4.3 Significance of Reactor Pressure.

The adsorption reactions discussed in section 4.3.1 were performed using the large volume 0.7 cc stainless steel reactor. In previous studies[67], the total pressure in the

reactor was above a critical pressure limit. Above this limit the number of collisions between clusters and helium molecules are sufficiently enough to remove the heat of adsorption and stabilize the product. The discussion in section 4.3.1, assumes the pressure is above this critical limit for the adsorption of SO_2 on vanadium oxide anions. When the reactor pressure is below this limit, unimolecular decomposition is possible and will effect the results observed in mass spectrum. The following describes the process that may occur when there are insufficient stabilization collisions with helium atoms to remove the heat of adsorption.

$$(VO)^-_X + SO_2 \underset{k'_n}{\overset{k_n}{\rightleftharpoons}} (VO)^-_X SO_2^* + He \xrightarrow{k_S} (VO)^-_X SO_2$$

When conditions are above the critical pressure: $k'_n \ll k_s$. Therefore the rate determining step is the first step involving k_n. In the discussion in section 4.3.1, it was not determined whether the reactions were in equilibrium or kinetic control, but it is assumed there is no unimolecular decay via k'_n. In this section the results from experiments performed in higher pressure reactors are discussed. The results suggest the pressure in the reactors are in the regime where $k'_n \leq k_s$ for some reactions and $k'_n \geq k_s$ in other reactions. The results indicate the pressure in the FTR ultimately governs k_s. The product is determined by the amount of helium in the reactor and is independent of the concentration of the products and time spent in the reactor. For the case where $k'_n \ll k_s$, the clusters that show adsorption as described in section 4.3.1. Since each cluster is an independent system, the binding energy of the SO_2 may differ from cluster to cluster. Therefore, at lower pressures, some adsorption reactions may under go unimolecular

decay too fast to be detected. If the increased pressure satisfies the condition $k_n' \ll k_s$, then the adsorption reactions are identified more readily in the mass spectrum.

If the increase in total pressure is above the pressure where $k_n' \ll k_s$, then it can be determined whether the reaction is in equilibrium or kinetic control. The reaction time can be varied by changing the length or temperature of the FTR. However, if k_n' is in the regime where it is competitive with the stabilization by helium, k_s, then the time spent in the FTR has no bearing on the outcome of the reaction.

The improved activation at higher pressures is also observed in the desorption of H_2O upon the adsorption of SO_2 on VO_3^-. As discussed in section 4.3.1, the weak interaction between H_2O and VO_3^- is broken and H_2O is lost with the adsorption of SO_2. With insufficient stabilization by helium interactions, the molecule $VO_3SO_2^- \bullet H_2O$ is not observed and degrades. In the smaller 400 cmm brass reactor, the reaction proceeds differently. In the smaller reactor, the heat of reaction is absorbed by the helium carrier gas. In the larger reactor, this is not the case. The loss of the H_2O molecule takes with it some of the heat of adsorption. Theoretical studies previously reported [68] reveal a binding energy of 1.02eV for H_2O on VO_3H molecule. Quantum chemical calculations reported in chapter 5, show binding energy of 2.69 eV for H_2O on VO_3^-. The calculated binding energy for SO_2 on VO_3^-, also reported in chapter 5, is found to be 2.79 eV. The loss of the H_2O would leave only ~0.1 eV to be dissipated by the buffer gas or vibrational by the molecule. However, to retain the water ~0.6 eV must be removed. This is approximately 250 collisions with the helium, if each collision removes 0.1 kT of the adsorption energy.[69,70] The dissipation of the heat of adsorption must be also be rapid. If

the dissipation is too slower then an H_2O will be lost. The increased total pressure expedites the removal of the heat of adsorption and prevents the loss of water upon adsorption.

4.4.4 Determination of Binding Energy.

When the total reactor pressure is increased, as discussed in section 4.3.4, the rate of reaction as a function of partial pressure is increased. This may suggest the reactions are not in equilibrium.

If we assume this is under equilibrium control, elementary thermodynamics can be used to predict the absorption or binding energy of the SO_2 to the cluster anion. In addition to the assumption of equilibrium, the temperature of the clusters are assumed to be the same temperature of the reactor. Also, it is assumed that there are sufficient third-body collisions with the helium carrier gas to remove the heat-of-absorption.

Equation 4.2 below defines the equilibrium constant, K_{eq}, for the last reaction shown in Scheme 1.

$$K_{eq} = \frac{1}{P_{SO_2}} \frac{[V_5O_{12}SO_2^-]}{[V_5O_{12}^-]} = \frac{1}{P_{SO_2}} \frac{f}{1-f} \tag{4.2}$$

In equation 4.2, *f* is the probability that $V_5O_{13}^-$ will adsorb an SO_2. The probability is calculated as the extent of reaction from equation 4.1. The term P_{SO2} is simply the partial pressure of SO_2. Equation 4.2 now can now satisfy the relations in equation 4.3.

$$-kT \cdot \ln(K_{eq}) = \Delta_r H - T \cdot \Delta_r S = -E_b + T \cdot S^o_{SO_2} \tag{4.3}$$

Where $\Delta_r H$ and $\Delta_r S$ are replaced with E_b, the binding energy, and $\Delta_r S^o_{SO_2}$, the standard entropy of SO_2 (= 0.248 kJ K^{-1} $mole^{-1}$ at standard temperature and pressure). After combining equations 4.2 and 4.3, we get equation 4.4.

$$-E_b = kT \cdot \ln(P^{(f=0.5)}_{SO_2}) - T \cdot S^o_{SO_2} \tag{4.4}$$

This is a convenient relation when $f = 0.5$ or when the ratio of the reactant and product peaks in the mass spectrum are 1:1.

The binding energy, E_b, can be calculated in several ways. First, one can simply extrapolate the partial pressure from the plot of the partial pressure versus extent of reaction. A convenient point to use would be where y = 0.5, then equation 4.4 can be used directly. Upon further inspection of Figure 4-11, the extent of reaction never reaches the 0.5 mark. A simple curve fit using equation 4.5 as the fitting function will allow the value for λ can be calculated attained.

$$f(P_{SO_2}) = \frac{\lambda \cdot P_{SO_2}}{\lambda \cdot P_{SO_2} + 1} \tag{4.5}$$

Now equation 4.6 can be used to calculate the binding energy, E_b.

$$\lambda = \exp\left(\frac{E_b}{kT} - \frac{S^o_{SO_2}}{k} \right) \tag{4.6}$$

A curve fit to the data in Figure 4-11 using Microcal Origin 4.1 yielded λ values of 117.7 and 66.8 for the 1-inch and 1.5-inch reactors respectively. The binding energies where then calculated to be 86.3 kJ mole^{-1} (0.89 eV) and 84.9 kJ mole^{-1} (0.88 eV) for the pair at a temperature of 300K.

A third approach is to simply select a data point and use equation 4.2 to calculate E_b. In order to give a better estimation of the binding energy, the calculation was repeated for all points in Figure 4-11. The average binding energy is then calculated to be 86.0 kJ mole^{-1} in good agreement with the curve fit giving for the 1-inch reactor and 85.7 kJ mole^{-1} for the 1.5-inch reactor. In comparison to the addition of SO_2 to $V_5O_{12}^-$, the binding energy is from DFT calculation is predicted to be 2.75 eV. The rational the product $V_5O_{13}SO_2^-$ with a binding energy of 0.89 eV is not collisionally stabilized, but $V_5O_{12}SO_2^-$ with a binding energy of approximately 2.75 eV is stabilized leads to several conclusions. The first is the probability or the reaction constant k_n is smaller for $V_5O_{13}^-$ than for $V_5O_{12}^-$. This suggests there is a greater probability that $V_5O_{12}^-$ will adsorb an SO_2 faster and have more time to become deactivated.

If we assume that the adsorption reactions of SO_2 for $V_5O_{11}^-$ and $V_5O_{12}^-$ are in equilibrium and apply this theory we calculate binding energies of 90 kJ mol^{-1} (0.93 eV) and 92 kJ mol^{-1} (0.95 eV), respectively. The meaning of these values are discussed further in Chapter V. DFT results predict the binding energy to be approximately 2.75 eV. This analysis is a clear indication that the reaction is not in equilibrium.

4.5 Conclusions.

Under fully oxidizing conditions the clusters show no signs of adsorption with SO_2. It is not until the oxygen content is lowered below a critical composition that the clusters demonstrate reactivity. The extent of reaction is easily controlled by the amount of SO_2 added down stream. The reaction can be controlled even further by changing the total pressure of the flow tube reactor. This is accomplished by decreasing the reactor volume. The time spent in the reactor can also be increased or decreased by lengthening or shortening the reactor.

The industrial catalytic oxidation of SO_2 is achieved at high temperatures, ~600K. Ideal conditions must be maintained for the catalysis to proceed, i.e. the partial pressure of oxygen and the temperature. In the case where the fully oxidized vanadium oxide anions are being produced (5% O_2:He in the carrier gas), it is not clear whether all of the oxygen in the carrier gas is consumed by the ablated vanadium atoms. This can be inherently problematic. If there is still additional oxygen present, it will undoubtedly also be present in the flow tube reactor as well. The presence of additional oxygen changes the experiment. No longer can the interaction of SO_2 and the fully oxidized vanadium oxide anions be studied. Instead, the study is of a three component system: $V_XO_Y^-$, SO_2 and O_2. As the percentage of O_2 is decreased and less oxidized anions appear, there certainly is less O_2 present in the reactor. There is no way to be absolutely sure this is the case. However, it is lower due to the initial percentage introduced initially, thus the onset of reactivity toward the fully oxidized anions may be the result.

An argument can be made that the oxygen concentration during cluster formation may determine an isomeric dispersion of the clusters produced. This could be the reason

for a sudden increase of reactivity. The formation of a different reactive isomer in the presence of less oxygen is quite possible. Further studies will have to be performed to explore this possibility via experiments that can not be performed currently in this lab. The determination of the isomers formed could be accomplished by many methods from photoelectron spectroscopy to differential mobility measurements. These types of experiments should be performed over a range of carrier gas compositions and temperatures.

Alternatively, generation of the cluster anions using a different source may prove to be successful as well. The use of a vanadium oxide target, V_2O_5, VO_2, V_2O_3, or $NaVO_3$, to produce anionic clusters may prove be as effective and would ultimately run no risk of additional unwanted oxygen that may interfere in the flow tube reactor. An alternative method for generation may yield clusters of preferred compositions or magic numbers. Proof that magic numbers exist for the vanadium oxide cluster system would be a key contribution to the understand of the structure and reactivity of said system.

CHAPTER V

MONO-VANADATE COMPLEXES: THEIR ABUNDANCES, STRUCTURES AND REACTIONS WITH SO_2

5.1 Introduction.

Mono-vanadate complexes are of interest in their own right—some have been known and used for years. These small complexes have been identified in the condensed phase and the gas phase as either neutral or charged species. The low redox potential of the vanadium atom, as well as the ability to easily adapt its bonding structure, give the metal unique catalytic properties. Most commonly vanadium pentoxide, V_2O_5, as an unsupported and supported catalyst have been widely reported[5-8] and well known[2,3], namely in the oxidation of SO_2 to SO_3 in the production of sulfuric acid, as shown here:

$$SO_2 + O_2 \rightarrow SO_3 \ (+ H_2O \rightarrow H_2SO_4)$$

Sulfuric acid is the most abundant industrially produced compound each year.[9] The V_2O_5 catalyst is less expensive and therefore has replaced platinum based catalysts. Optimal production of SO_3 is achieved at elevated temperature, with maximum efficiency achieved near 600K. The elevated temperature increases the life time of the catalyst. To compensate for this lost efficiency, layers of catalyst are used with in the reactor to completely convert all the SO_2 to SO_3.

Mono-vanadium oxides form large polyanions known as Polyoxometallates (POMs) that have many useful properties. POMs have been found to have many useful chemical and catalytic properties.[66] Homogeneous POMs containing vanadium have been identified, but more interesting is heterogeneous POMs that have been found to have unique properties that are attributed to the single vanadium atom they possess.

Vanadium complexes in biological systems has been shown to be beneficial and, in some instances, vital. A exhaustive recent review of vanadium chemistry by Crans, et al, discusses the role of monovanadium complexes in molecular biology.[71] Vanadium can also be used as an analogue for phosphorus both structurally and electronically, although some differences are apparent.

Small mono-vanadium oxide (VO_x) complexes are excellent models for high-level computational chemistry techniques. The electronic structures of these compounds have been studied on the experimental and theoretical levels.[25,40,68,72-78] Quantum chemical calculations, performed on many isomeric complexes, converge quickly and may have higher accuracy. This in-depth understanding of the complex electronic structure makes these compounds good candidates for testing new computational methods. Using such approaches, mono-vanadium oxide clusters can be used as models for bulk surface reactions such as hydrolysis and catalytic transformations at specific defect sites, grain boundaries, or edges.

Mono-vanadates also serve as model compounds for the higher VO_x compounds such tri-vanadium clusters, because they are for higher order vanadium oxide clusters.[49] Therefore, certain electronic structure and geometric features of mono-vanadates may be extended to these larger clusters. Of these larger species, tri-vanadate clusters have been

investigated and isolated. The tri-vanadate complexes have a ring structure as a global minimum. The ring is a planar ring made up of VO_3 units and V-O-V bonds forming the ring. The most interesting tri-vanadate complex is $V_3O_9^{3-}$.[35] Like the mono-vanadium compounds, the vanadium is in the +5 oxidation state. Polyoxometalate compounds have been found to be comprised of these small these small VO_x units. Sodium metavanadate solutions, $NaVO_3$, have been reported to form more complex species. These species have been observed by electrospray ionization (ESI-MS). The species present were found to be dependent on the pH of the solution.[33,34] In turn, larger polyanions of V_2O_5 stoichiometry have been isolated: [$V_5O_{14}^{3-}$] and [$V_{12}O_{32}^{4-}$].

In previously reported gas-phase studies, as well as our current research, it has been shown these complexes are abundant and very easily produced.[23,49,79,80] Small vanadium-oxide compounds are readily generated in the gas phase as charged and neutral clusters. Recently, Castleman and co-workers have reviewed several reports on the structure and reactivity of charged vanadium oxide clusters.[18] Among the various VO_x-cluster findings, the vanadium oxide cluster cations have shown a high degree of reactivity toward various organic compounds. Within their research, they found the anionic clusters are not as reactive toward the same molecules. The anion spectrum has been characterized as robust. Other reports have shown the smallest clusters are reactive toward some organic esters by means of "catalytic" decomposition.[22,79]

The VO_x clusters, whether, cationic, anionic or neutral, are easily generated by laser ablation of vanadium metal in the presence of molecular oxygen. Statistical methods have been employed to study the formation of these clusters using ablation methods.[23] The resulting charged clusters can be easily detected by mass spectrometry

techniques. The neutral clusters, however, may be more difficult to observe. The ionization potential of these clusters can be very high. There is a substantial risk of photodissociating the clusters by applying extreme laser intensity. However, improved photoionization methods have proven to be adequate in studying the reactivity and composition of the neutral vanadium oxide clusters.

Within the scope of this area of cluster research, a few elementary units can be utilized as a basis for the effects of the more complex clusters. Of the basic units, three of the most fundamentally relevant anions are VO_3^-, VO_4^-, and $H_2VO_4^-$.

Metavanadate, VO_3^-, is a common anion in the solid state and in solution-phase chemistry. It is considered a rather inert gas-phase anion by some reports, nonreactive with hydrocarbons in Castelman's reports,[19,20] but reactive toward MMA on much longer time scales, nearly 3 seconds to reach a 1:1 product to reactant ratio.[22] Our experiments deal with reaction times less than 200μs.

In its global equilibrium structure, VO_3^- is a planar, symmetric (D_{3h}) structure as shown below.[40] The V-O bond lengths are close to those of the double-bond in the vanadyl, O=V(-O-)$_3$ unit found in larger cage clusters. Electronically, the vanadium d-orbitals are empty, with all of its electrons donated to the V-O bonds. It is convenient to designate the $3d^0$ orbital as the LUMO and assign a formal oxidation state of +5 to the vanadium atom. In doing this an electron is left to be shared over all three oxygen atoms. The excess negative charge may be considered as being distributed equally over the three oxide, $O^{(2-)}$, atoms in a LCAO of the oxygen 2*p* orbitals that form the HOMO. As evidence of its stable, saturated valence, its electron affinity is very large. Experimentally, it has been determined to be 3.8 to 4.4 eV for the adiabatic electron

affinity and vertical detachment energies.[21,25] Theoretically, a range between 3.84 and 4.45 eV has been calculated with an average of 8 calculation to be 4.15 eV.[40]

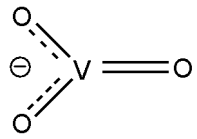

However, for the interactions at the oxygen site, i.e. that break this equivalence, the molecular orbitals are represent as such:

LUMO: Vanadium $3d_{z^2}$ orbital

HOMO: Oxygen 2*p* orbitals

In contrast, the neutral VO_3 structure is a (ever so slightly) distorted non-planar structure. Two of the V-O bonds are of equal length with the third bond slightly shorter. A more explicit discussion of the electronic state of each molecule has been presented. [40].

The molecule VO_4^- is referred to as a peroxo version of VO_3^- metavanadate. This form also has empty vanadium d-orbitals that make the $3d_{z^2}$ the LUMO, thereby confirming the vanadium in a +5 oxidation state. In its global form, two of the oxygen atoms are bound as oxides and the other two are bound to each other and to the V center in a triangular arrangement recognized as the "peroxo" form. The O-O bond length is near 1.49Å. Electronically, it is a closed shell, spin-singlet, with a large vertical electron affinity. The HOMO is the O-O single bond. Its electronic structure and bonding may be represented by the following schematic:

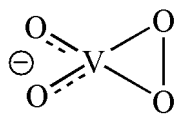

The formation of this complex may be regarded as derived from a reaction of VO_3^- with the O_2 molecule as shown in Equation (1):

$$VO_3^- + \tfrac{1}{2}\, O_2 \longrightarrow VO_4^- \qquad (1)$$

In our experiments it is found to be very reactive toward SO_2. This reactivity will be discussed later.

$H_2VO_4^-$, regarded as $V(OH)_2O_2^-$, hydro-monovanadate is detectable even under ultra-high purity conditions and no other VO_X cluster have protonated satellite features. Another frequent exception is $V_3O_9H_2^-$. (See Chapter 7.)

Its lowest-energy form may be represented by the Scheme below:

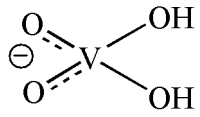

It may be regarded as the hydrolysis product of VO_3^-:

$$VO_3^- + H_2O \longrightarrow VO_2(OH)_2^- \qquad (2)$$

Accordingly, it is a saturated, closed-shell, with the vanadium atom in the +5 oxidation state.

In the following, the production of these three important mono-vanadate complexes discussed and their reactions with SO_2, O_2, and H_2O are presented. The interactions with SO_2 were carried out in a pulsed helium flow reactor and characterized by time-of-flight mass spectrometry. The resulting products were then modeled using quantum calculations at the same levels as reference 40. Lowest energy structures were determined by examining isomeric structures based on previously computed structures.

5.2 Experimental.

The VO_x cluster anions were produce via laser ablation techniques as described in chapters 2-4. Briefly, a pure vanadium rod was ablated with the third harmonic of a Nd:YAG laser in the presence of oxygen inside a vaporization block (B) as shown in Figure 5-1. The oxygen is contained in a mixture of helium that acts as a carrier gas and is delivered through a pulsed valve (A) IN Figure 5-1 . The percentage of oxygen contained in the helium carrier gas can be a crucial detail when preparing vanadium oxide clusters. In our work, oxygen-helium mixture containing from 10% to 0.5% were used and were found to have no effect on the composition of the mono-vanadium oxide complexes. The clusters are then thermalized as the carrier gas pulse moves the clusters through the expansion region (C).

The VO_x anions are then interacted with reactant gases in the flow tube reactor, Figure 5-1D. The clusters are temporally overlapped with a pulse containing 10% SO_2 in helium. The total pressure in the flow tube reactor can be changed from 200 mbar to 400 mbar. This is accomplished by using various flow tube reactors with different volumes. As a result, the total pressure can be increased as the volume is decreased. The technique allows the same reactions to be studied as a function of the total pressure with in the reaction vessel. Upon exiting the flow tube reactor, the cluster beam is skimmed and then analyzed by a time-of-flight mass spectrometer.

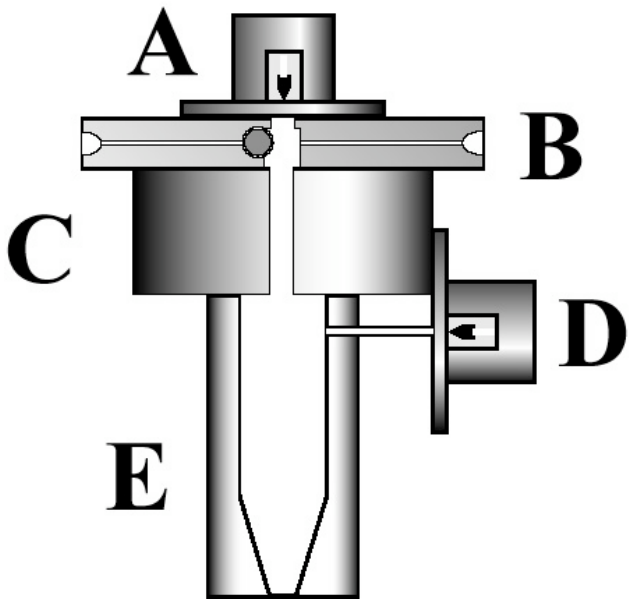

Figure 5-1. Cluster source and flow tube reactor. A carrier gas mixture is introduced via a pulsed gas valve (A). The vaporization block (B) contains a pure vanadium target rod. The ablated atoms interact with the oxygen in the carrier gas and form the vanadium oxide anions. As the cluster pulse moves through the thermalization region (C) it is equilibrated to the temperature of the experiment. As the pulse enters the flow tube reactor (D) it is overlapped with a reactant gas. Upon exiting the rector, it is then analyzed using a time of flight mass spectrometer.

5.3 Theoretical Techniques.

Density functional calculations were performed using MacSpartan '02 with Q-Chem.[81] Prior DFT studies on vanadium oxide clusters [40,54] employed Becke's hybrid three parameter nonlocal exchange functional with the Lee-Yang-Parr correlation functional (B3LYP) [82-84] with an Alrich's all electron triple-zeta valence (TZV) basis set. [85] These studies each compared and considered other exchange correlations and basis sets, but have shows this combination to give the best results. [40,54]

The results of the DFT calculations were compared to the structures and electron affinities reported in Ref 40. The geometric properties match very well with bond lengths within 0.01A and the bond angles were within 0.1 degree. The electron affinity calculation were also with acceptable values. The adiabatic electron affinity and the vertical detachment energies were each calculated. In comparison to the values reported by Sauer using the B3LYP exchange correlation and the TZV basis set, the computed energies were in good agreement with in 0.02 eV.

5.4 Results and Discussion.

5.4.1 Experimental Results and Discussion.

Typical representative mass spectral data collected is shown in Figure 5-2. The mono-vanadate complexes of interest are observed in spectrum (i). The masses are assigned to the high abundance peaks in as follows in Table 1 below.

Table 5-1. Monovanadium Cluster Anion Masses and Variant Names.

Mass (amu)	Cluster	Variant/Name
99	VO_3^-	Metavanadate
115	VO_4^-	Peroxovanadate
117	$V(OH)_2O_2^-$	Hydroxyvanadate
163	VO_5S^-	Sulfito Vanadate
179	VO_6S^-	Sulfato Vanadate
181	$H_2VO_5S^-$	Sulfito Hydroxyvanadate

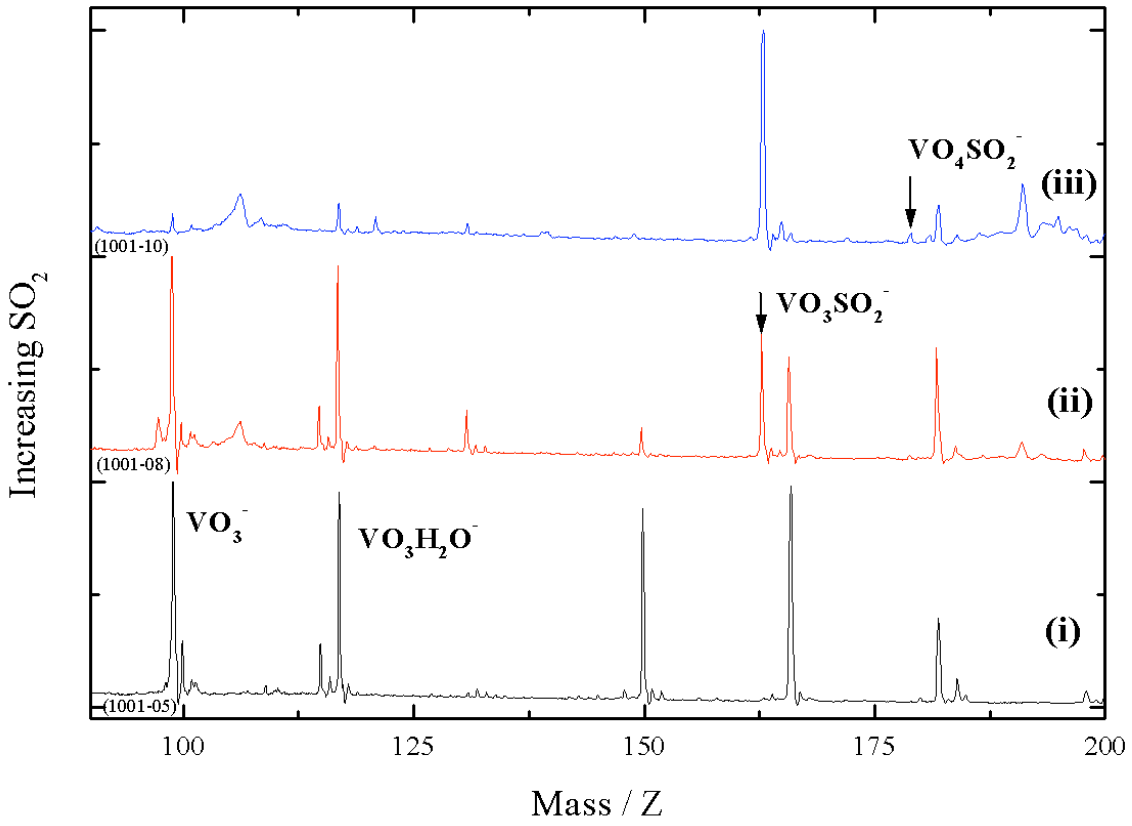

Figure 5-2. Mass Spectrum of monovanadium oxide anions: spectrum (i) is a reference mass spectrum displaying VO_3^- and $VO_3H_2O^-$. The peak that is not labeled preceding $VO_3H_2O^-$ is VO_4^-. Spectra (ii) and (iii) are the results after SO_2 is added to the flow tube reactor. The amount of SO_2 is increased quantitatively going from spectrum (ii) to spectrum (iii). As the amount of SO_2 is increased, the SO_2 adsorbs and completely converts the clusters VO_3^- and $VO_3H_2O^-$ to $VO_3SO_2^-$. A peak corresponding to $VO_4SO_2^-$ accounts for the depletion of the VO_4^-.

The vanadate complexes that have been found to be inert toward organic molecules[86] have been receptive toward addition of SO_2 in flow reactor experiments. It can observed in Figure 5-2, that addition of SO_2 occurs as the amount or partial pressure of SO_2 is increased in the flow tube reactor. The reduction in abundance and the appearance of new product peaks at 163 amu and 179 amu explained as the direct result of the adsorption process. The particular experiment displayed in Figure 5-2 also shows the dehydration of $VO_3H_2O^-$.

The absence of a product peak appearing at 181 amu verifies this result. The reaction shown in equation (3) best describes this observation.

$$V(OH)_2O_2^- + SO_2 \rightarrow VO_3SO_2^- + H_2O \qquad (3)$$

The loss of H_2O is further justified quantitatively by comparing the integrated peak intensities of the mass peaks 99, 115 and 117 amu with the integrated intensity of the peaks at 163, 179 and 181 amu. If the sum of the areas of the reactant peaks at the lower masses in spectrum (i) are equal to the sum of the area of the products peaks (high mass peaks) in spectrum (ii) and (iii), then it is assumed the ion molecules are not lost as reaction conditions change. In the experiments discussed, it has been verified the ion molecules are conserved by comparing the peak areas. Not only does this confirm the products originate from the parent VO_3^-, VO_4^- and $V(OH)_2O_2^-$ complexes, but it also suggests that there is no fragmentation of larger clusters contributing to these masses. Larger di-vanadium oxide anion complexes can be observed in mass spectra (i) and (ii) and presumed to also uptake SO_2, as described elsewhere. It is important to note the

mass of $V_2O_5^-$ is 182. Distinguished $V_2O_5^-$ from $VO_6SH_2^-$ at 181 amu is well with in the resolution capability of the mass spectrometer.

The loss of H_2O from the $V(OH)_2O_2^-$ anion can be controlled to some extent. This displacement of H_2O can be a result of insufficient cooling upon adsorption of SO_2. In Figure 5-3, it is observed that the addition of SO_2 does not necessarily include the loss of H_2O. This is can be observed in spectrum (iv) of Figure 5-3 by the much stronger intensity of the $VO_6SH_2^-$ complex peak at mass 181. The conditions of the reaction studied in Figure 5-3 were under higher carrier gas pressure. A smaller reactor volume was used to increased the total pressure of helium to about 0.4 bar. As a results the increased pressure of the buffer gas increased the stability to the formation a $VO_6SH_2^-$ molecule.

At this higher pressure, unimolecular decay still occurs however. One indication of this is broad hump in the base line located between mass peaks 163 and 179. This broad shaped peak is characteristic of ions that fall apart in the mass spectrometer and are reflected at a different velocity by the ion reflector. If a molecule fragments while in the free flight region of the mass spectrometer, the charged fragment will maintain its velocity. However, when this fragment is reflected in the turn-around region of the mass spectrometer, it will penetrate less deeply, turn around sooner and thus arrive at the detector before its parent.

The result is the broad peak observed in spectrum (iv) of Figure 5-2. Such decays can be studied and used to calculate unimolecular decay constants. Further discussion of such analysis is not with in the scope of this report.

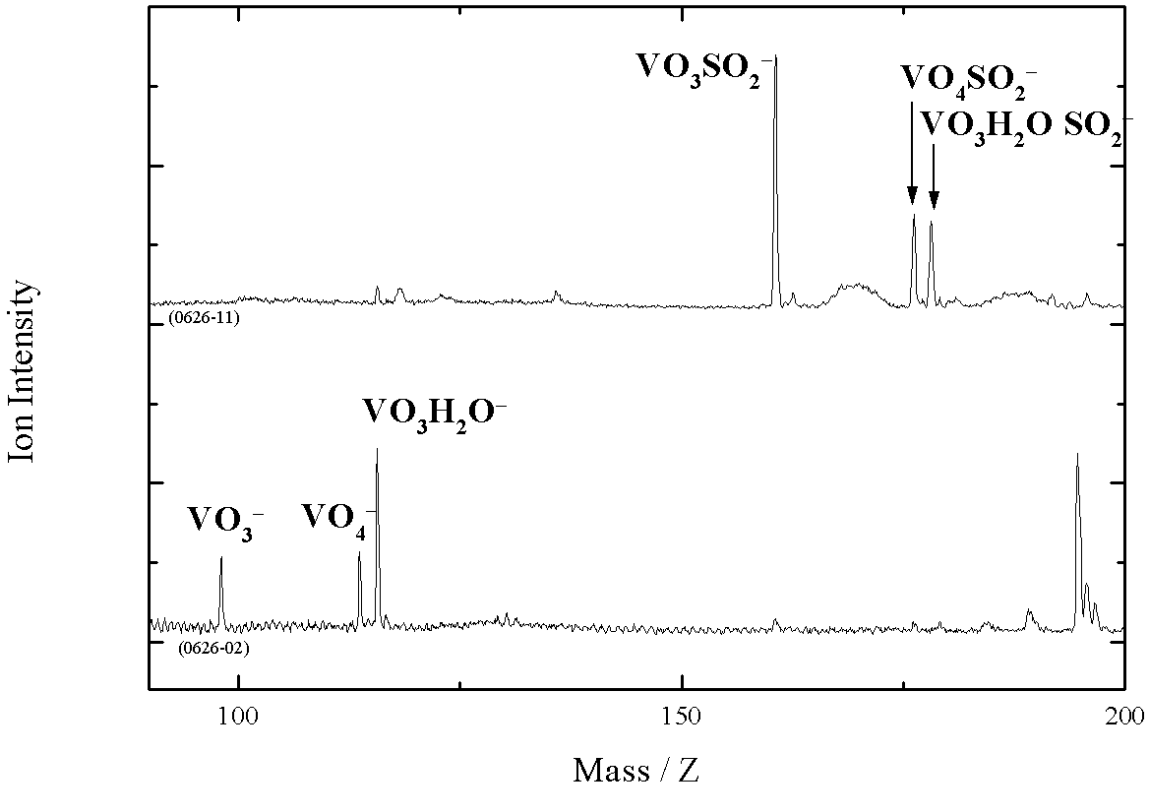

Figure 5-3. Addition of SO_2 at 400 mbar. The total pressure in the flow tube reactor is increased to nearly 400 mbar by decreasing the volume of the flow tube reactor. The lower mass spectrum is the result before addition of SO_2. The clusters VO_3^-, VO_4^- and $VO_3H_2O^-$ are mark in the reference spectrum. After addition of SO_2 to the flow tube reactor, it is observed that the clusters adsorb SO_2 and show up as the product peaks as labeled in the top mass spectrum. The results at this total pressure differ from the same experiment performed at lower pressure show in Figure 5-2, where the addition of SO_2 is accompanied my the loss of H_2O for $VO_3H_2O^-$.

From the experimental data a complete set of observed reactions are summarized by equations 3-6 :

$$VO_3^- + SO_2 \rightarrow VO_3SO_2^- \qquad [4]$$

$$VO_4^- + SO_2 \rightarrow VO_4SO_2^- \qquad [5]$$

$$V(OH)_2O_2^- + SO_2 \rightarrow V(OH)_2O_2SO_2^- \qquad [6]$$

The high efficiency, i.e. a sticking probability comparable to C_8^-, of these processes suggest they are driven by the formation of strong bonds, unhindered by any high barriers to reaction. The quantum-chemical modeling, discussed next, confirms this strong bonds are formed.

5.4.2 Theoretical Results and Discussion.

Figures 5-4 through 5-7 illustrate the candidate structures and reaction Scheme pathways observed in experimental data. The base of the phenomena is VO_3^-. At the different stages of the experiment, VO_3^- can undergo several transformations. While in the vaporization region, further oxidation of the anion occurs to yield peroxovanadate complex, VO_4^-. Also, hydrolysis of trace water can occur to yield the hydroxovanadate variant, $VO_4H_2^-$. Each of the anions then undergo addition of SO_2. The mechanism by which SO_2 adsorbs to the VO_x cluster is not easily determined. Several reports on the catalysis of SO_2 to SO_3 by V_2O_5 propose several mechanisms and structures. The structures reported included multiply charged multi-sulfate complex with the molecular formula $(VO)_2O(SO_4)_4^{4-}$.

$VO_3SO_2^-$. The product from the reaction described in equation 4, has detected in the mass spectrum as shown in Figure 5-2 and 5-3. DFT calculations have produced several different structures and confirmed a large, favorable bond association energy. The structure of VO_3^- was calculated and used as a starting point for the interaction with SO_2. The geometry of the VO_3^- molecule was found to be consistent with that calculated by Vyboischikov and Sauer. The resulting minimized configuration was found to be a

trigonal planer structure with D_{3h} symmetry as closed-shell singlet ground state. The V-O bond length were found to be 1.66Å with a O-V-0 bond angle of 120°. It should also be noted the 3d orbitals of the vanadium atom were found to be the LUMO confirming a +5 oxidation state.

The addition of SO_2 is not as trivial as may be expected. The sulfur dioxide molecule is an ambidentate ligand, meaning electron donation can occur through the sulfur atom, the oxygen atoms, or both. From the experimental details, it is also unclear whether the oxygen atoms or the vanadium atom of the VO_3^- interacts with the SO_2. This ambiguity leaves four possibilities for the adsorption reaction: i.) a sulfur-vanadium bond, ii.) an oxygen-vanadium bond, iii.) a sulfur-oxygen bond or iv.) an oxygen-oxygen bond. However, a fifth possibility is a combination of options ii. and iii. It should be considered that the sulfur and the oxygen can each be involved.

The addition of SO_2 bound through the sulfur atom to the vanadium atom, gives structure A as shown in Figure 5-4. The trigonal planer VO_3 is distorted slightly into a pyramid structure with the sulfur forming a long dative bond with the vanadium. The oxygen atoms of the sulfur are positioned equidistant from the vanadium atom and lie in the same plane as the vanadium and sulfur atoms. This state is highly unstable and very unfavorable at an energy of 0.24 eV higher than the isolated VO_3^- and SO_2 energies. Vibrational analysis suggests this structure is a saddle point giving an imaginary frequency concerning the oxygen atoms of the SO_2.

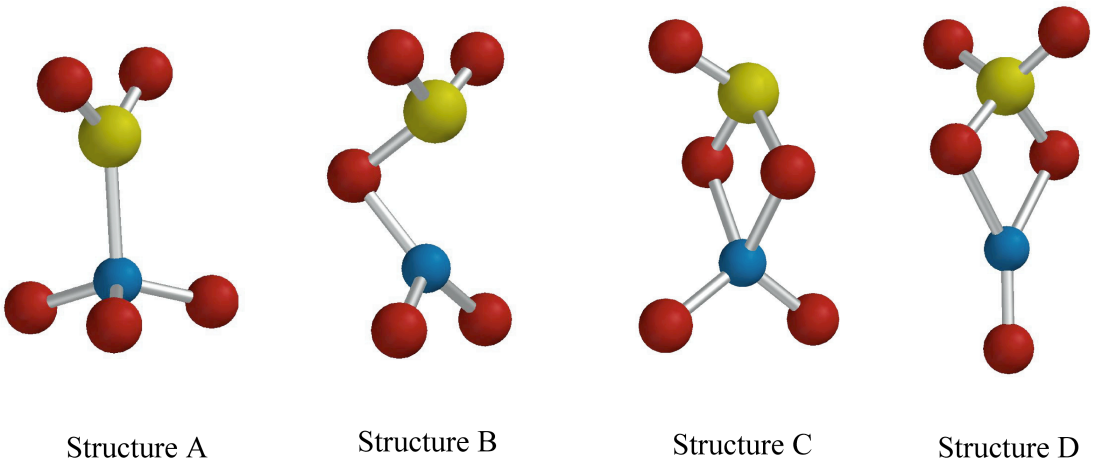

Figure 5-4. Calculated Structures for VO_3^- and SO_2.

When the SO_2 is perturbed from its aligned position a local minimum is found at 1.10 eV lower than the separated components. This is structure B, as shown in Figure 5-4, is closed shell anion singlet. The SO_2 is associated with an oxygen atom of the VO_3 component forming a sulfite. The sulfite group is bound to a what would be a VO_2 unit through an elongated V-O bond. This complex is very different than the starting reactants. By inspecting the oxidation states of the sulfur and vanadium, there has to have been a charge transfer from the vanadium to the sulfur. By assigning the oxygen atoms a -2 oxidation state, the vanadium still maintains a +5 state. By assigning the negative charge to the sulfur of the SO_2, the sulfur maintains its +4 state.

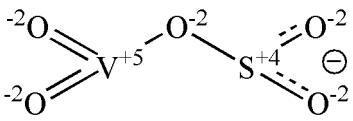

A local saddle point was calculated for this structure and determined to be 0.44 eV higher in energy than structure B and 0.66 eV lower than the initial reactants total

energy. The saddle point structure calculation yielded a much long V-O bond. The saddle point is associated with the uptake of SO_2, so it is clear from the geometry that the reaction coordinate is the S-O(V) distance.

Although the structure B is favorable in energy, the search produced a much more stable structure. Structure C shown in Figure 5-4 is the result the minimization calculation. The anion is calculated to be a singlet ground state with a change in energy of 2.57 eV. The sulfur and the vanadium are bound by two bridging oxygen atoms, one atom "donated" from the VO_3^- and one atom "donated" from the SO_2. The sulfur has a third doubly bound oxygen that gives the sulfur a trigonal pyramid structure. The vanadium center is left with the remaining oxygen atoms that are symmetrically bound in a tetrahedral position with respect to the bridging oxygen atoms. The bond angles about the vanadium atom are not a pure tetrahedral. The (S)O-V-O(S) bond is strained at an angle of 78.3°. The other angles are more relaxed with the (S)O-V-O at 115.7° and the O-V-O bond at 110.5°. The negative charge is found to be in a HOMO dominated by the 2p orbitals of the oxygen atom of the sulfito group. The LUMO remains the d_{z^2} orbital of the vanadium atom.

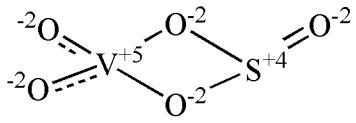

To confirm the lowest energy isomer was a sulfite complex, an energy minimization was preformed on a sulfato complex that resulted in structure D in Figure 5-4. The anion was found to be nearly the same energy as the separated starting components, 0.1 eV higher. Chemical intuition can justify this auto-redox reaction giving a less stable structure. As shown below, the oxidation state of the sulfur is now a

+6 to compensate for the additional oxygen bonds. In order to preserve the over all negative charge of the anion, the vanadium atom must take on a +3 oxidation state. As a result of this unfavorable rearrangement, the electronic charge is found on the vanadium atom.

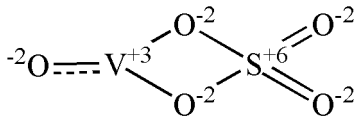

$VO_4^-SO_2^-$. The calculations above model the interaction of VO_3^- and SO_2 as shown in Figure 5-4 or 5-7. If VO_3^- is further oxidized to VO_4^- , as represented in Scheme 1, then the adsorption of SO_2 can take a different path. A DFT calculated structure for VO_4^- is shown in Figure 5-5. This structure and electronics properties were found to be in excellent agreement with the reports by Vyboischikov and Sauer.[40] (For a detailed discussion of this molecule see or the supplementary material section for geometric details.)

Here, SO_2 was found to bond directly to the peroxide ligand, generating a sulfato complex. The vanadium and the sulfur have tetrahedral structure which gives the product C_{2V} symmetry. Details of the bond lengths and bond angles can found in the supplementary materials.

As part of a previous study, Froeberg and Johansen[87] used Hartree-Fock (HF) methods and complete active space perturbation treatment (CASPT) to study this very complex. In comparison, our geometric results were within 5 pm for the HF number, while the CASPT results were with in 1 pm. This study compared their calculated geometries with that of a divanadate-sulfate crystal structure isolated by Nielsen and coworkers. [88] The isolated structure was then later claimed to be the active complex

responsible for the oxidation of SO_2 to SO_3. [8] However, the claim is not without controversy.[11]

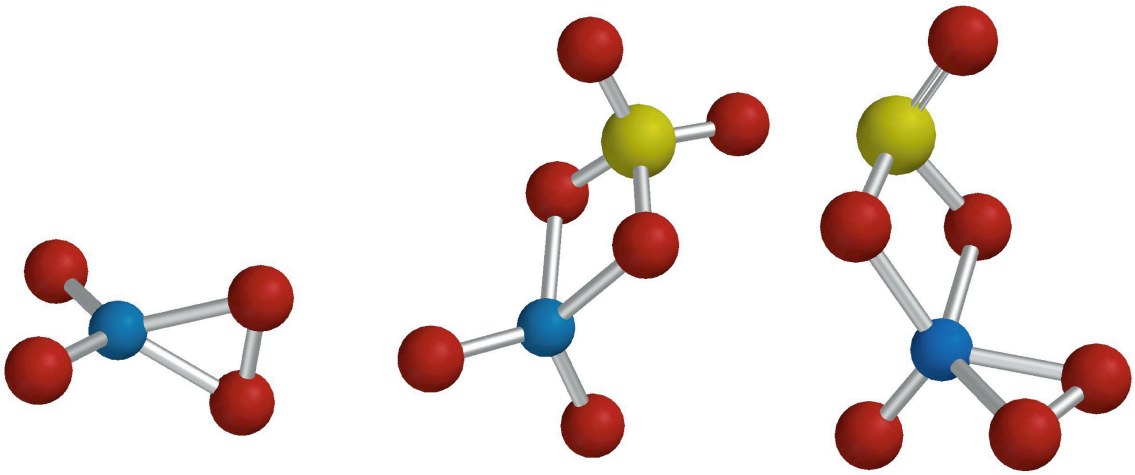

Figure 5-5. Calculated structures for VO_4^- and SO_2.

The peroxovanadate(E) HOMO derives from the 2*p* orbitals of the oxygen atoms. The charge, is distributed over the oxygen atoms on the sulfur and those on the vanadium. Since it is a singlet ground state, the HOMO is obviously shared by a pair of electrons. However, the LUMO is dominated by a V 3d-orbital. This helps to confirm the fully oxidized vanadium atom. Geometrically, the anion has C_{2V} symmetry. The angle formed by the O2-S-O2' is 95.0° compared to 109.5° calculated for an unbound SO_4^{2-}. This is a more relaxed than the measure of the analogous angle found in the sulfite form found in the $VO_3SO_2^-$. Examination of the oxidation states, shows the sulfur atom going to a +6 state from a +4 state. The vanadium center maintains the +5 state by keeping the

charge state of the cluster complex, but the peroxy-oxygens each go from (-1) to (-2), formally.

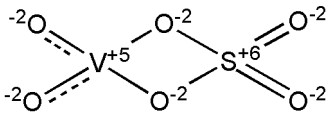

$VO_4H_2^-$. The DFT calculations of hydrated monovanadium oxyanions produced results similar to those above. Figure 5-6 shows the lowest energy structures for the hydrated VO_3^- and the products upon adsorption of SO_2. A recent study explored the proton affinities of tetrahedral oxyacids that included $H_2VO_4^-$.[89] The authors reported bond lengths and vibrational frequencies for VO_4^{3-} and its protonated variants up to $H_4VO_4^+$.

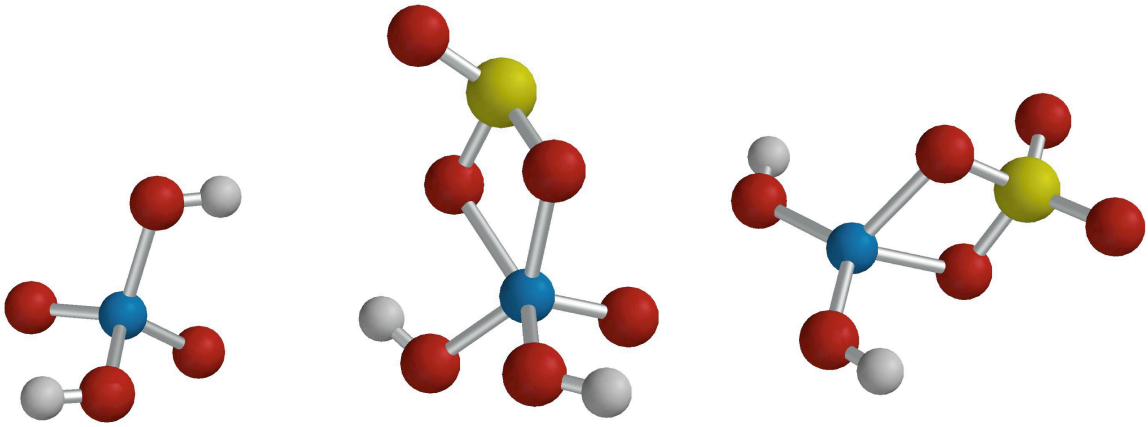

$VO_2(OH)_2^-$ Structure G Structure H

Figure 5-6. Calculated Structure for the complex $VO_2(OH)_2SO_2^-$.

The analysis correlated the proton affinity to the highest O-H vibrational stretching frequency. The geometric and vibrational details reported for $H_2VO_4^-$ were in agreement with our calculated values. Details of the geometric structure of this molecule are included with the supplementary information. Briefly, the anion was found to have C_{2V} symmetry. Each V-O bond length is 1.63Å with the V-OH bonds having a length of 1.87Å. The structure is nearly a pure tetrahedral. The only distinction is the O=V=O angle that is widened at an angle of 112.3° compared to 109.2° for the HO-V-OH angle. The electronic ground state of $H_2VO_4^-$ was found to be a singlet with A_2 symmetry for the HOMO. The vanadium and oxygen atoms retain a +5 and –2 oxidation numbers, respectively. The HOMO is assigned to the 2*p*-orbitals of oxygen molecules as in the VO_3^- molecule as shown here:

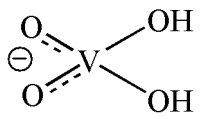

According to Figure 5-7, we suggest the addition of H_2O to VO_3^- results in hydrolysis of H_2O. In fact, the hydrolysis results in the lowest energy structure for $H_2VO_4^-$. We explored the possibility of having a weakly hydrogen bonded H_2O molecule associated with a VO_3^- molecule. A local minimum was found at 0.87 eV lower than the energies of the initial free components, VO_3^- and H_2O. Although favorable, the hydrolyzed form is 2.69 eV lower in energy.

The addition of SO_2 to this complex is not as trivial as in the cases of VO_3^- and VO_4^-. Various structures were considered. The lowest-energy conformation is of the

sulfito type, preserving the +4 oxidation state of the sulfur as a SO_3 and the +5 state of the vanadium atom. However, the binding of the SO_2 is much weaker than that of SO_2 to VO_3^- or VO_4^-, yielding only 0.74 eV. The oxidation states can be accounted for by counting the electrons as follows:

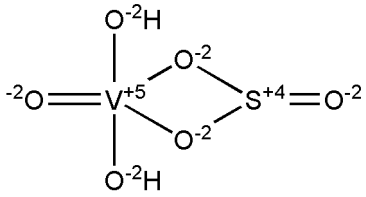

The structure about the vanadium is a distorted trigonal bi-pyramid. However, the equatorial VO_3 unit resembles the neutral VO_3 molecule. The sum of the three angles, two HO-V-O angles and one HO-V-OH angle, is 311.0° compared to 332° computed by ref.[40]. The HOMO is filled occupying the *p*-orbitals of the free oxygen of the SO_3 unit. The LUMO appears to be the d_{xy} orbital of the vanadium atom.

A second structure, of the sulfato type, shown in Figure 5-6 H, with C_{2v} symmetry. It is higher in relative energy than the infinitely separated components. In comparison to the fore-mentioned bi-pyramidal structure, it is 1.62 eV higher. The rearrangement to higher symmetry involves a redox reaction where the sulfur is oxidized to a +6 oxidation state and the vanadium is reduced to a +3 state as shown here:

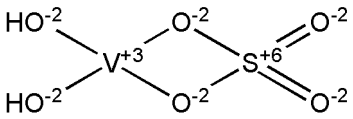

The ground electronic state of this molecule is a singlet. The HOMO has a A_1 symmetry with the electronic charge localized in the vanadium d_{z^2} orbital. The LUMO is also located on the vanadium atom as the d_{xz} orbitals.

Figure 5-7 incorporates all the these lowest-energy structures on an energy-level diagram, with arrows indicating the inferred processes. The calculated energies of the reactants and products of each are listed in table 1.

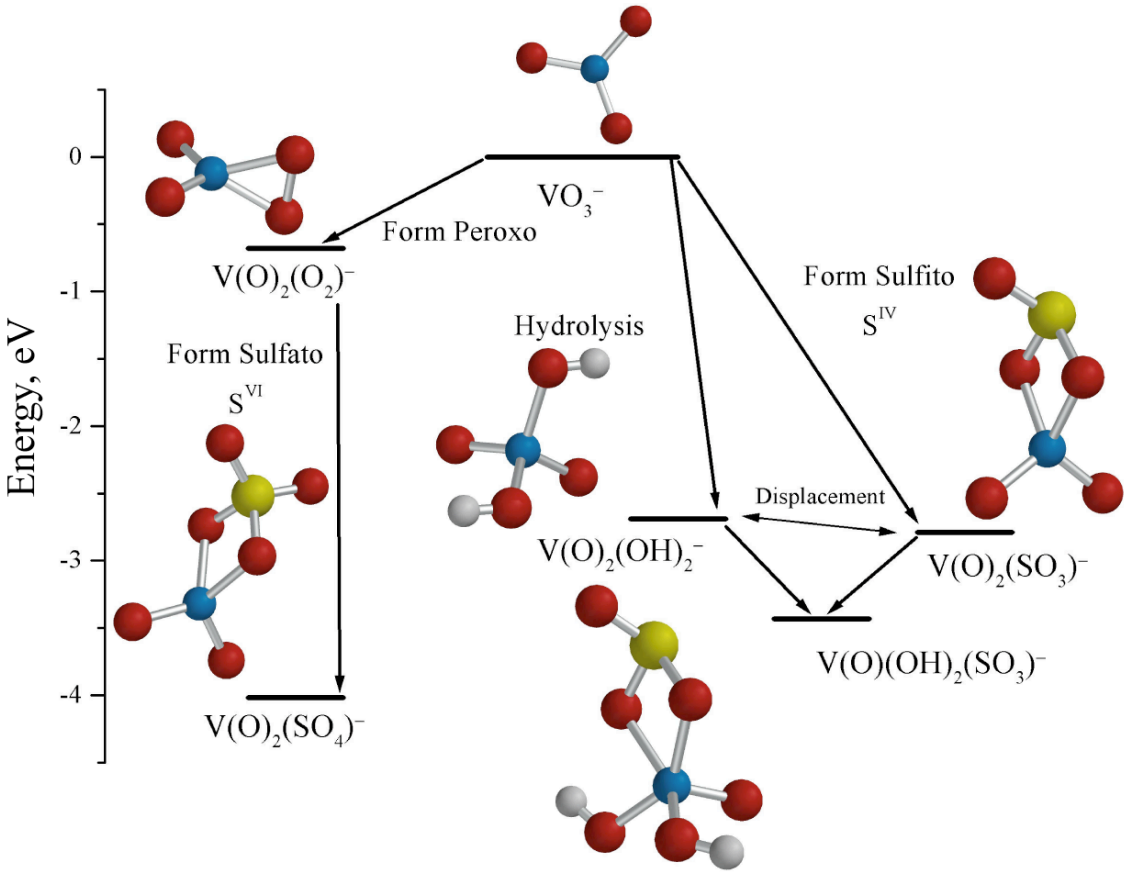

Figure 5-7. Summary of reaction pathways observed in the experiments described in Figures 5-2 and 5-3. The energy scale on the left depicts the change in energy upon absorption with respect to VO_3^- and SO_2.

5.5 Conclusion:

The interaction between monovanadate oxide anions and sulfur dioxide results in a very strong adsorption reaction. This is observed experimentally as shown in Figures 5-2 and 5-3 and summarized in equations 3 through 6. The amount of SO_2 added in the flow reactor determines the extent of reaction. This is evident when comparing spectra (ii) and (iii) in Figure 5-2, where the amount of SO_2 is increased in spectrum (iii). In spectrum (iii), it can be observed that all the mono-vanadate clusters have adsorbed an SO_2 molecule, which is bound only by ~0.7 eV. The cluster "$VO_3 \bullet H_2O^-$" adsorbs an SO_2 molecule and loses the H_2O equivalent mass. If the total pressure in the flow tube reactor is increased, the H_2O molecule is not lost quantitatively and the stabilized product $VO_3H_2O \bullet SO_2^-$ is detected. The higher gas pressure provides more stabilizing collisions after addition of SO_2. This removes the heat of adsorption faster than when the reaction is performed in the low pressure limit. In the low pressure limit, the loss of the H_2O molecule will remove heat when it is desorbed. This helps form a stable product with less collisions with the carrier gas.

The quantum calculations show very high binding energies for either VO_3^- and VO_4^- with SO_2 as shown in Table 1 as well as the hydrolytic addition of H_2O to VO_3^-. These three reaction yielded the highest change in energies, all greater than 2.6 eV, and are the most predominant in the experiments. The addition of SO_2 to the hydrated VO_3^- species has been shown to be less favorable than to the dehydrated cluster.

Thus, a series of reactions can be used to describe this experiment as shown in Figure 5-7. Starting with VO_3^- there are three possibilities that can occur. First, two

VO_3^- can interact with additional oxygen molecule and adsorb another oxygen atom to become VO_4^-. Second, the VO_3^- can alternatively adsorb an H_2O molecule hydrolytically; or third adsorb an SO_2 as sulfite. In the flow reactor, VO_4^- can interact with an SO_2 form the sulfite complex $VO_2(SO_4)^-$. Finally, $VO_3H_2O^-$ can adsorb an SO_2 forming either $VO_3H_2O{\bullet}SO_2^-$ or $VO_3SO_2^-$. The loss of the weakly bound H_2O molecule can help remove and additional energy.

Table 5-2. Reaction Energies for VO_3^-, VO_4^- and $VO_3H_2O^-$ with SO_2.

Reaction	Sum of Reactant Energies (hartrees)	Sum of Product Energies (hartrees)	Change in Energy (eV)
$VO_3^- + SO_2 \rightarrow VO_5S^-$	-1718.5854	-1718.6869	-2.79
$VO_4^- + SO_2 \rightarrow VO_6S^-$	-1793.8010	-1718.9239	-3.34
$VO_3^- + H_2O \rightarrow VO_4H_2^-$	-1246.3769	-1246.4759	-2.69
$VO_4H_2^- + SO_2 \rightarrow VO_6SH_2^-$	-1795.1450	-1795.1722	-0.74
$VO_5S^- + H_2O \rightarrow VO_6SH_2^-$	-1795.1475	-1795.1722	-0.67
$VO_4H_2^- + SO_2 \rightarrow VO_5S^- + H_2O$	-1795.1450	-1795.1475	-0.07

The computed results suggest preservation of the oxidation states of the vanadium and sulfur will form the most favorable complexes. In the case where the oxidation states are not preserved, it is the oxidation of the sulfur that is found to be the most favorable followed by the reduction of the vanadium atom.

5.6. Supporting Information

Table 5-3. Geometry of VO_3^-.

	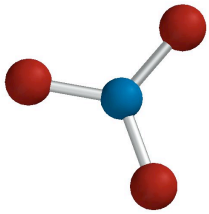	
VO_3^- $E=E^0$	Bond	Length (Å)
	O-V	1.66
	Angle	Degrees
	∠O1-V-O1'	120
VO_3 $E = E^0 + 4.22$	Bond	Length (Å)
	O1-V O2-V	1.67 1.61
	Angle	Degrees
	∠O1-V-O1' ∠O1-V-O2	112.0 107.0

Table 5-4. Geometry of $VO_3SO_2^-$ (B).

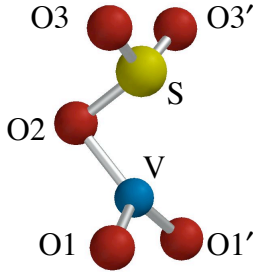		
$VO_3SO_2^-$ (B) E= E^0 -1.10 eV	Bond	Length (Å)
	O1-V	1.62
	O2-V	1.87
	O2-S	1.70
	O3-S	1.49
	Angles	Degrees
	∠O3-S-O3'	115.9
	∠O3-S-O2	108.8
	∠O3-S-V	122.0
	∠S-O2-V	82.0
	∠O2-V-O1	120.5
	∠O1-V-O1'	113.1

Table 5-5. Geometry of $VO_3SO_2^-$ (B).

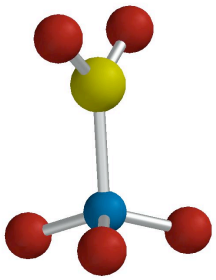		
$VO_3SO_2^-$ (A) E = E^0 + 0.24 eV	Bond	Length (Å)
	O3-S	1.42
	O1-V	1.67
	O2-V	1.68
	S-V	2.20
	Angle	Degrees
	∠O-V-O	112.6
	∠O-S-O	104.6

Table 5-6. Geometry of VO_3SO_2 (C).

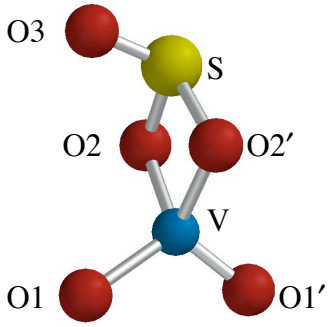

$V(O)_2SO_3$ (C) $E = E^0 + 3.10$ eV	Bond	Length (Å)
	O3-S	1.46
	O2-S	1.74
	O2-V	1.81
	O1-V	1.81
	O1′-V	1.58
	S-V	2.64
	Angle	Degrees
	∠O3-S-O2	109.6
	∠O2-S-O2'	88.4
	∠S-O2-V	93.5
	∠O2-V-O2'	83.8
	∠O2-V-O1	115.2
	∠O1-V-O1'	111.8

Table 5-7. Geometry of $VO_3SO_2^-$ (C).

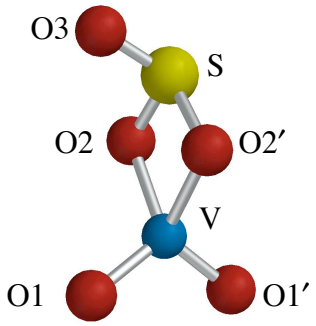

$V(O)_2SO_3^-$ (C) $E = E^0 - 2.57$ eV	Bond	Length(A)
	O3-S	1.49
	O2-S	1.67
	O2-V	1.92
	O1-V	1.62
	O1′-V	1.62
	S-V	2.63
	Angle	Degrees
	∠O3-S-O2	108.9
	∠O2-S-O2'	93.2
	∠S-O2-V	94.3
	∠O2-V-O2'	78.3
	∠O2-V-O1	115.7
	∠O1-V-O1'	110.5

Table 5-8. Geometry of $VO_3SO_2^-$ (D).

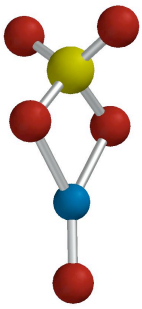		
$VOSO_4^-$ (D) $E = E^0 + 0.1$ eV	Atoms	Distance(Å)
	O3-S	1.48
	O2-S	1.61
	O2-V	1.97
	O1-V	1.62
	S-V	2.64
	Angle	Degrees
	∠O3-S-O3'	1-16.9
	∠O3-S-O2	110.4
	∠O2-S-O2'	96.6
	∠O2-V-O2'	74.8
	∠O2-V-O1	142.6
	∠S-O2-V	94.3

Table 5-9. Geometry of VO_4^-.

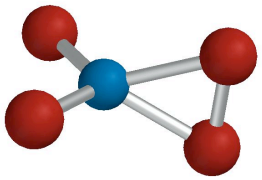		
VO_4^- $E = E^0 - 0.68$ eV	Bond	Length(A)
	02-V	1.85
	01-V	1.63
	02-02	1.49
	Angle	Degrees
	∠O2-V-O1	120.0
	∠O1-V-O1'	113.8
	∠O2-V-O2'	47.3

Table 5-10. Geometry of $VO_4SO_2^-$ (E).

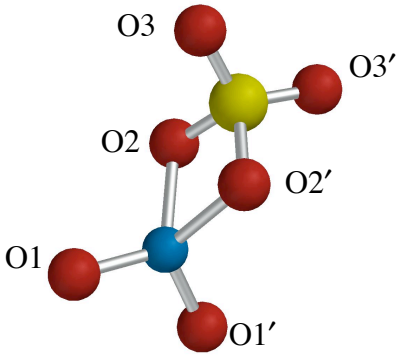

$VO_4SO_2^-$ (E) $E = E_0 - 4.02$ eV	Bond	Length(Å)
	O3-S	1.47
	O2-S	1.61
	O2-V	1.94
	O1-V	1.61
	S-V	2.63
	Angle	Degrees
	∠O3-S-O3'	117.4
	∠O3-S-O2	110.5
	∠O2-S-O2'	95.0
	∠O2-V-O2'	75.5
	∠O2-V-O1	116.9
	∠S-O2-V	94.9
	∠O1-V-O1'	110.2

Table 5-11. Geometry of $V(O)_2(OH)_2^-$.

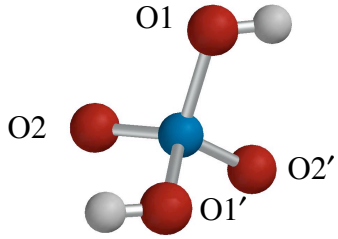

$V(O)_2(OH)_2^-$ E= E^0 - 2.69 eV	Bond	Length(Å)
	O1-V	1.87
	O2-V	1.63
	H-O1	0.96
	Angle	Degrees
	∠O2-V-O2'	112.3
	∠O2-V-O1	109.3
	∠O1-V-O1'	109.2

Table 5-12. Geometry of $VO_2(OH)_2SO_2^-$.

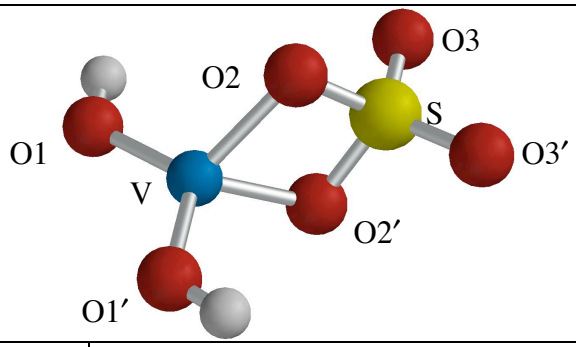

$VO_2(OH)_2SO_2^-$ (H)	Bond	Length
E =E^0 –3.57 eV	O3-S	1.48
	O2-S	1.61
	O2-V	1.95
	O1-V	1.81
	H-O	0.96
	S-V	2.67
	Angle	Degrees
	∠O3-S-O3'	1.16.3
	∠O3-S-O2	111.4
	∠O2-S-O2'	93.0
	∠O2-V-O2'	73.6
	∠O2-V-O1	113.4
	∠S-O2-V	96.7
	∠O1-V-O1'	120.2
	∠H-O1-V	123.1

Table 5-13. Geometry of $VO_2(OH)_2SO_2^-$.

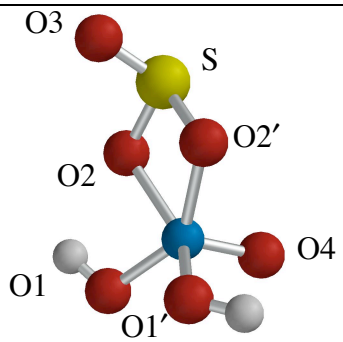

$VO(OH)_2SO_3^-$ (G)	Bond	Length(A)	Bond	Length(A)
E= E^0 – 3.43eV	O3-S	1.50		
	O2-S	1.68	02'-S	1.65
	O2-V	2.03	02'-V	1.95
	O1-V	1.83	01'-V	1.83
	O4-V	1.59		
	Angle	Degrees	Angle	Degrees
	∠O3-S-O2	109.2	∠O3-S-O2'	108.5
	∠O2-S-O2'	89.7		
	∠S-O2-V	97.6	∠S-O2'-V	100.3
	∠O2-V-O2'	71.0		
	∠O4-V-O3	107.2	∠O4-V-O3'	105.7
	∠O1-V-O1'	98.1		
	∠O2-V-O1	80.4	∠O2'-V-O1	143.0
	∠O2-V-O1'	143.5	∠O2'-V-O1'	91.6
	∠O2-V-O4	10	∠O2'-V-O4	104.2

Table 5-14. Adsorbate molecules.

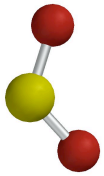		
SO_2	E = -548.6691 hartrees	
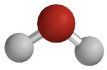		
H_2O	E = -76.4606 hartrees	
O_2	E= -150.3809 hartrees	

Table 5-15. Table of Absolute Energies and Symmetry.

Molecule	Energy (hartrees)	Symmetry
VO_3^-	-1169.9163	$^1A_2'$ D_{3h}
VO_4^-	-1245.1319	$^1A_2$ C_{2v}
$VO_2(OH)_2^-$	-1246.4759	^1A C_{2v}
$VO_3SO_2^-$ (A)	-1718.5766	$^1A'$ C_s
$VO_3SO_2^-$ (B)	-1718.6329	$^1A'$ C_s
$VO_3SO_2^-$ (C)	-1718.6869	$^1A'$ C_s
$VO_3SO_2^-$ (D)	-1718.5888	$^1A_1$ C_{2v}
$VO_4SO_2^-$ (E)	-1793.9239	$^1B_2$ C_{2v}
$VO_4SO_2^-$ (F)	-1793.8593	^1A C_s
$VO_2(OH)_2SO_2^-$ (G)	-1795.1722	^1A C_1
$VO_2(OH)_2SO_2^-$ (H)	-1795.1127	$^1A_1$ C_{2v}

CHAPTER VI

EFFICIENT LOW-TEMPERATURE OXIDATION OF CARBON-CLUSTER ANIONS BY SO_2: ATMOSPHERIC SOOT AND HEALTH IMPLICATIONS

6.1 Introduction.

Carbon-cluster anions, C_N^-, are very active toward SO_2 (sticking probability of 0.012 ± 0.005 for C_{27}^- at 25 ºC), as compared to their inertness toward other common atmospheric gases and pollutants. In flow-reactor experiments at ambient temperature and near atmospheric pressure, primary adsorption of SO_2 by the carbon cluster anions, N = 4 – 60, yields $C_NSO_2^-$ (α_N) or $C_{N-1}S^-$ (β_N), eliminating CO_2 neutral, as also detected in collision-induced dissociation. At higher temperatures, the reaction of SO_2 with nascent carbon clusters yields these α_N, β_N products as well as $C_{N-1}SO^-$ (γ_N) along with undetected CO_2 and CO. The size-dependent initial reactivity reflects the previously established cluster structural transitions, i.e. from linear-chain to cyclic to cage structures. Secondary

adsorption, observed, with higher intrinsic reactivity, suggests an accelerating oxidation process. Such carbon clusters are formed in sooting flames and can act as nuclei for the formation of primary soot particles, and serve as model compounds for black-carbon soot, to the extent that they share the local structural features of active soot particle sites. The facile generation of reactive carbon-sulfide and –sulfinate units may therefore have implications for understanding the health and environmental effects attributed to the coincidence of soot and SO_2.

Concentrated atmospheric emissions of black-carbon (soot) particulates and SO_2 coincide in many parts of the world as a result of incomplete fossil-fuel and biomass combustion. An estimated 12 to 24 Tg of carbon soot is emitted annually into the troposphere from biomass combustion and anthropogenic sources such as diesel engines and coal-fired power plants.[90,91] The simultaneous (coincidence) presence of these agents has been linked to death from lung cancer and heart disease.[92] However, the nature of any such cooperative interaction between SO_2 and soot particulates remains unclear, despite long study.[93] Among the possible mechanisms of soot-SO_2 interaction, soot may efficiently adsorb SO_2, thereby concentrating it in the lungs where subsequent processes lead to damage. Soot could also catalyze the oxidation of SO_2 to SO_3 (H_2SO_4) as first suggested in 1974 by Novakov *et al*,[94] and others more recently,[95-97] whereas a homogeneous gas-phase or aqueous reaction involving photogenerated OH radicals is the dominant reaction pathway for global-scale production of atmospheric H_2SO_4.[42,98] Finally, soot could react stoichiometrically with SO_2, modifying either the soot particle or SO_x into more harmful species. Carbon-SO_2 interactions are also relevant in

environmental remediation since activated carbon is used to remove SO_2 from hot flue gases.[99]

Here we address these questions by investigating the size-selective reactions of carbon-cluster anions with SO_2 vapor in an atmospheric-pressure fast-flow-reactor at ambient temperature. It has been shown that such carbon clusters are generated in sooting flames and act as the precursors to the larger (~ 5 nm) primary soot particles.[100] Carbon soot particles as small as 10-*nm* in diameter have been detected in sooting flames using differential mobility analysis.[101] Primary soot particles are defect-rich multishell structures with active sites for adsorption, and for unpaired electrons, as well as negative charging. Carbon-cluster anions, C_N^-, have been extensively studied.[102-104] They are generally highly stable (high electron affinity) species with known carbon-chain, -ring, and –cage structures, sharing these characteristics with active soot.[103,104] By contrast, carbon cluster cations (C_N^+) and neutrals are reactive toward a variety of atmospheric gases such as O_2, N_2O, and SO_2.[105-108] Certain carbon cluster anions can thus serve as well-defined models for defect sites in soot.

6.2 Results and Discussion.

Our initial interest has been in the adsorption and reaction processes of SO_2, without presence of O_2 or H_2O. Although the complete oxidation of carbon-graphite by SO_2 is favorable (-23 kcal·mol^{-1}), it is immeasurably slow except at elevated temperatures. Humeres *et al.*[99] studied the reduction of SO_2 on activated carbon at elevated temperatures. Using reactor partial pressures of 0.20 atmospheres of SO_2 at a temperature of 600 ºC, the dominant products were CO_2 and S_2. Above 630 ºC, CO and COS were formed in significant amounts. Using carbon-cluster anions (C_N^-) as a

surrogate for carbon soot, comparisons of the heats of formation of C_N^- and C_N and their reaction products containing $-SO_2$ were made for the smaller clusters N = 8 and 9, where accurate theoretical treatment is available. Many structural models have been considered – and actually calculated[82,84] – for the initial and intermediate products of SO_2 – cluster interactions in an attempt to identify plausible reaction mechanisms. Attempts to optimize certain cyclic addition structures, suggested by known organic analogs as well as XPS results on activated carbon,[99] led to the identification of strong-bound intermediates, depicted in Figure 6-1 and Table 1. The table contains the heats of reaction for the linear carbon clusters, C_N^m reacting with SO_2 to produce $C_NSO_2^m$.

Table 6-1. Quantum Calculated energies for SO_2 adsorption on carbon anions.

C_N	$C_N^m + SO_2 \rightarrow C_NSO_2^m$ $\Delta H_{reaction}$ (kJ·mol^{-1})	
N	Neutral m = 0	Anion m = -1
8	-129	-249
9	-70	+1.6

These calculations suggested that the reactions listed in Table 1 are favorable. Figure 6-1 shows the calculated structures for $C_8SO_2^-$ and $C_9SO_2^-$ using density functional theory[82,84].

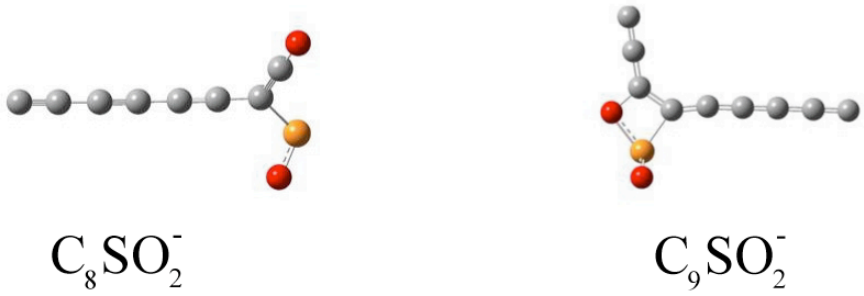

Figure 6-1: Calculated structures of $C_8SO_2^-$ and $C_9SO_2^-$. Energies for optimized ground-state configurations (linearly constrained) of carbon chains (above) were calculated with density functional theory utilizing the hybrid exchange-correlation functional B3LYP at the 6-311+G level. The optimized structures of the stable product $C_8SO_2^-$ (left) and $C_9SO_2^-$ (right) were left unconstrained. All quantum chemical calculations were conducted with the *GAUSSIAN '03* computational package. A complete theoretical study of this reaction will be published in the near future.**

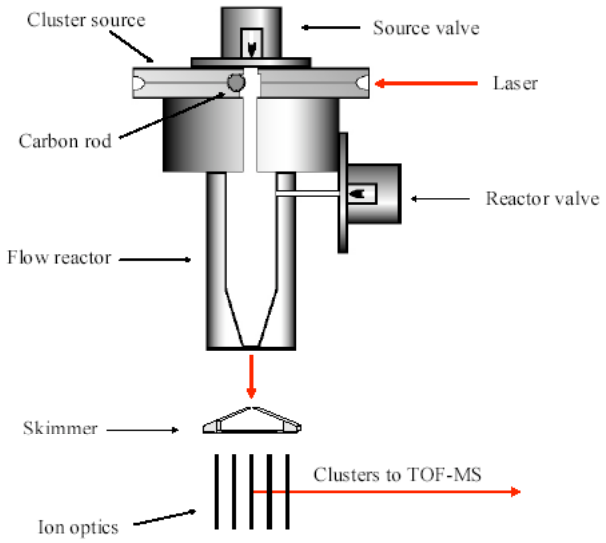

Figure 6-2: A schematic of the pulsed cluster source with atmospheric-pressure flow reactor. In each cycle of operation, the source gas-valve opens and delivers pulses (0.3-ms long, 20 mm^3 displaced volume) of high-pressure (8-*atm*) helium gas. The peak pressure in the flow-reactor can thus approach 0.5 bar, because of the choked exit-flow and modest (15-fold) volume expansion. Carbon clusters of various sizes and charge-states are produced by laser ablation (Nd:YAG, 355 nm) of a graphite rod, entrained and thermalized in the primary He flowstream. This packet merges with the reactant flowstream — a longer, weaker flow of SO_2 in He carrier — introduced from a reactor gas-valve, which opens at a variable delay with respect to the cluster-packet arrival. The SO_2 concentration in the reactor exceeds that of all the carbon clusters combined. The SO_2 partial-pressure in the reactor is estimated to be approximately 0.08% of the total pressure (approaching 0.4 mbar), as calculated from the prepared dilution (1.5 % for reactor insertion) in He and the instantaneous relative intensities (1:20) of the two gas pulses, as measured on a fast ionization gauge. The exit orifice of the flow reactor is tapered down from the reaction channel diameter of 6 mm to a diameter of 3 mm to ensure turbulent mixing of the reactants. The transit-time of the clusters through the reactor is estimated at 90-μs, corresponding to a 300-*m*/*s* flow speed (Mach-0.2 for He at this temperature). During this period, a carbon-cluster is estimated to undergo on the order of 10^5-10^6 thermalizing collisions with helium atoms, depending on cluster-size, and on the order of 10^2 encounters with SO_2. Such values are normally sufficient to establish the high-pressure limit of bimolecular reaction kinetics, as well as to ensure thermodynamic control in the case of reversible adsorption processes. After leaving the flow reactor, the jet containing reactants and products expands into vacuum, is skimmed, and enter the pulsed-voltage extraction region of the time-of-flight mass spectrometer.

Scheme 1 shows the proposed primary reactions offered to account for product identities found in our mass analysis. The efficient reaction of thermalized carbon anion clusters, C_N^-, with a dilute mixture of SO_2 in helium at ambient temperature yields $C_NSO_2^-$, C_NS^-, and C_NSO^-, accompanied by the (undetected) evolution of CO_2 and CO across a cluster size range of N = 4 to 50. The presence of the CO_2 product was confirmed indirectly as a meta-stable decay neutral. Under the same experimental conditions, no adsorption or reaction products due to the interaction of O_2, NO, or the much more strongly oxidizing N_2O with C_N^- were detected. The interaction of NO_2 with certain C_N^- does produce detectable amounts of associated products.

$$
\begin{array}{ccc}
 & & C_NSO_2^- \\
 & \alpha_N \uparrow & \\
C_N^- + SO_2 \rightleftharpoons [C_N^- \bullet SO_2] & \xrightarrow{\beta_N} & C_{N-1}S^- \\
 & \gamma_N \downarrow & \\
 & & C_{N-1}SO^- + CO
\end{array}
$$

Scheme 1

The reaction of SO_2 with C_N^- occurred in a near atmospheric-pressure, variable-temperature fast-flow reactor and the products were detected by a time-of-flight mass spectrometrically, following standard procedures.[109] Figure 6-2 shows the schematic features of the cluster source – flow reactor and details of the apparatus are described elsewhere. Similar results are also obtained with O_2 (2% in He) or H_2O (saturated vapor in He). The cooled clusters enter the flow reactor and interact with a flow of dilute 1.5% SO_2:He gas mixture for up to 0.10 ms as the clusters traversed the length of the flow reactor (15 or 25 mm).

The C_N^- cluster reacts with SO_2 to form stable products under ambient temperature and near-atmospheric conditions at ~230 ppm of SO_2 at a total flow reactor pressure estimated at 0.3 bar. Figure 6-3 shows the mid-N mass region of the resultant mass spectra with and without the addition of SO_2 to the flow-stream of thermalized (wall temperature ~300 K) C_N^- clusters. In Figure 6-3(a), a reference spectrum (lower) is produced when the reactor gas flow is offset temporally from the source gas flow to show unreacted C_N^- clusters only for N = 11 - 26. In Figure 6-3(a), (upper) the flows are overlapping and both product and reactant peaks are present. The low-N mass region (N = 5 to 18) with and without the addition of SO_2 under the same conditions are shown in Figure 6-3(b). The primary products are detected and correlated to the depletion of the parent C_N^- concentration via the proposed (α_N, β_N) reactions shown in Scheme 1. The α_N and β_N products contain one sulfur each as confirmed by an isotopic-abundance analysis of the product peak groupings (m, $m+1$, $m+2$) in higher SO_2-concentration spectra revealing the presence of both C (^{13}C, $m+1$) and S (^{34}S, $m+2$). As the SO_2 concentration is increased in the flow reactor, the abundance of products increase relative to that of unreacted C_N^- clusters, suggesting that the reaction can be driven toward completion. The sticking probability was estimated to be 0.012 ± 0.005 for C_{27}^- at 45% depletion at ambient temperature under the experimental conditions used.* These estimates are quite different from the uptake coefficient (0.002) of SO_2 on n-hexane soot at – 100 ºC reported by Koehler *et al.*[97]

---

* For example, under conditions where the SO_2 partial pressure is estimated (from previous calibrated experiments) at 0.015 Torr, the C_{27}^- cluster is found to be depleted by 45% as a result of 20 encounters. To estimate the number of encounters, one multiplies the geometrical cross-section for these species, 0.9 nm^2, their rms speeds, 340 m/s, the SO_2 concentration, and the transit time, 90 μs.

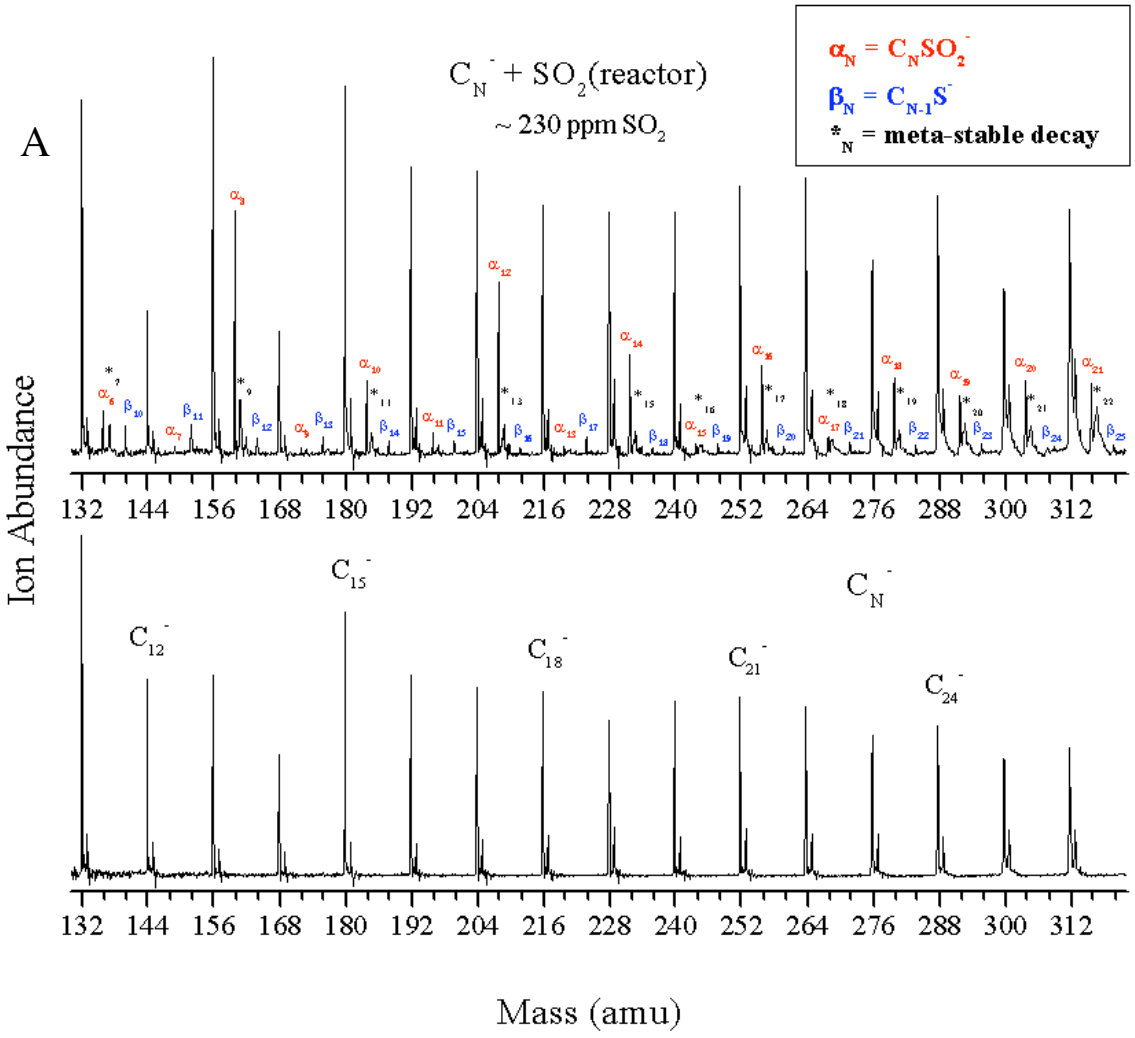

Figure 6-3(a): **A high-N mass spectra of thermalized carbon cluster anions, C_N^-, in the region of C_{11}^- - C_{26}^- without (below) and with (above) exposure to a 1.5% SO_2:He stream in the flow reactor at room temperature (P_{SO2} = 0.14 mbar). The addition of SO_2 leads to the appearance of new peaks in the mass spectrum corresponding to ambient-temperature reactions producing $C_NSO_2^-$ (α_N) and $C_{N-1}S^-$ (β_N). Isotopic analysis of the product peak groupings (*m*, *m+1*, *m+2*) in higher SO_2-concentration spectra reveals the presences of both C (^{13}C, *m+1*) and S (^{34}S, *m+2*). Broad peaks β_N* assigned to the delayed loss of CO_2 are present and appear every ~24 amu (N = 5 – 15), then every 12 amu (N = 16 – higher).**

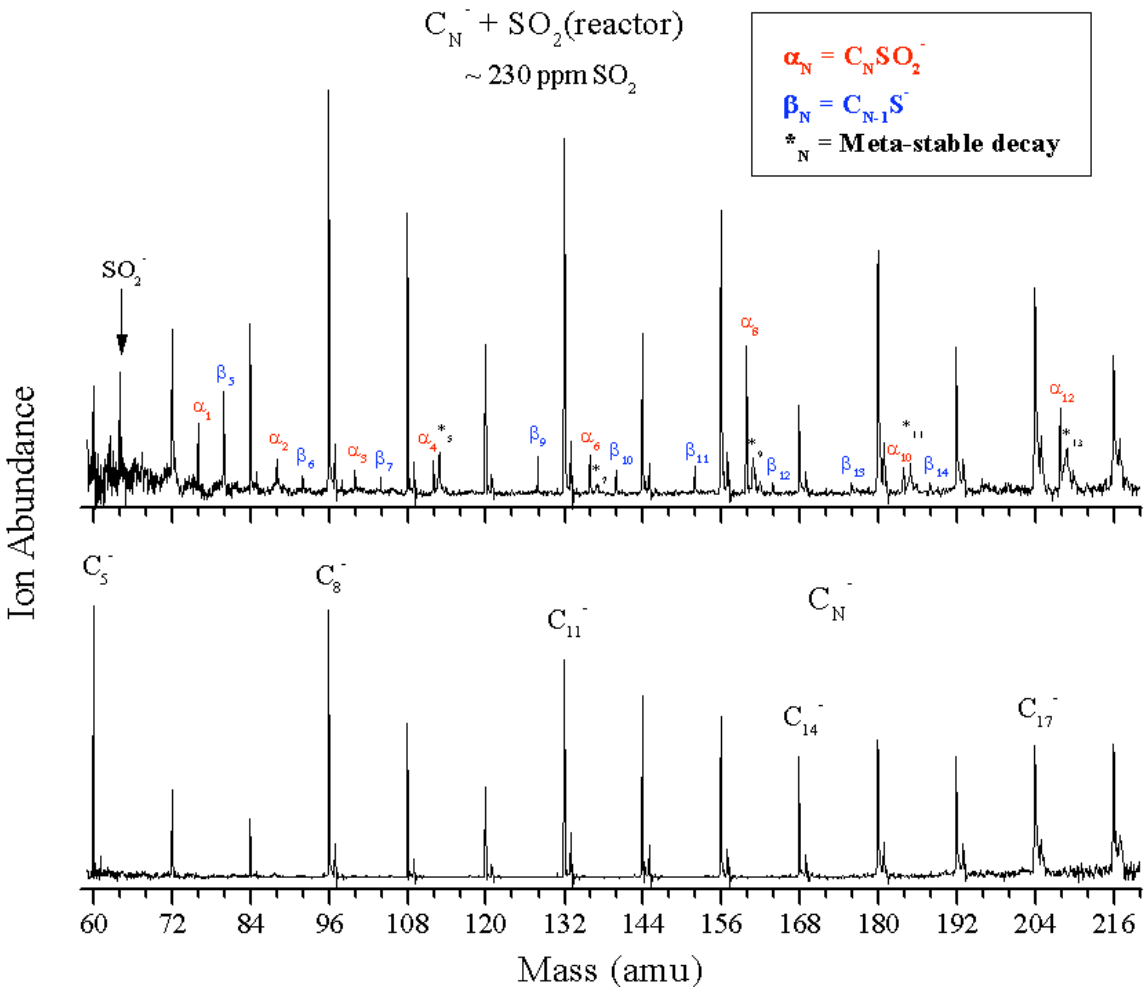

Figure 6-3(b): **Same conditions as (a), but for low-N mass in the region of C_5^- - C_{18}^-. Increasing the partial pressure of SO_2 in the reactor drives the reaction toward completion.**

The reaction mass spectra (Figure 6-3) also show the presence of broad peaks located near to the α_N product peaks. These peaks were assigned to the meta-stable decay of weakly adsorbed species during the flight in the field-free region of the TOF spectrometer.[110] A characteristic of meta-stable peaks is that their location is dependent on the potential difference across the reflectron thus their positions on the mass scale can be moved by changing the reflectron voltages. Stable product peaks will maintain the same mass position independent from the reflectron voltage. These meta-stable peaks were calculated to be the result of the loss of weakly-bound CO_2. Figure 6-4 shows the comparison of the calculated time difference and the measured time difference between the stable product and its charged daughter fragment that would occur during the field free flight if the product lost CO_2. This process is represented by

$$\alpha_N \_ \beta_N^* + CO_2 \qquad (2)$$

The meta-stable peaks occur at 24 amu spacings in the low-mass region (89, 113, 137, 161, 185, 209, and 233 amu) then shift to a 12-amu spacing in the higher-mass region (245, 257, 269, …, 665). Each one of these meta-stable peaks can be assigned to the meta-stable decay of the low mass $\alpha_{odd\text{-}N}$ cluster from N = 5 – 15, then α_N (even and odd) from N = 16 and higher to produce the corresponding β_N cluster and CO_2.

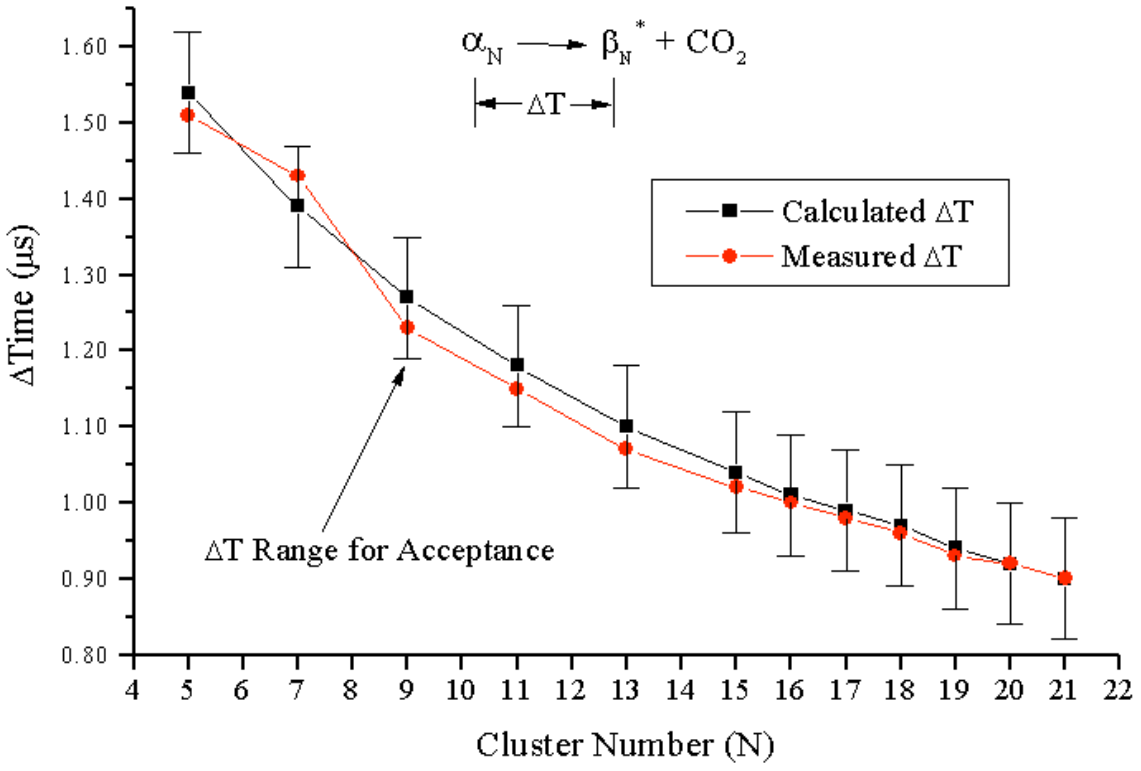

Figure 6-4: Calculated versus the measured time difference between the arrival at the detector of a stable product ion and a daughter ion as the result of a meta-stable decay. An α_N product can dissociate (decay) while in the field-free region of the TOF mass spectrometer. By assuming the loss of CO_2, a calculation can reveal when the fragmented ion will be detected. This assumption is verified when the measured ΔT is within 80 ns of the calculated value. All meta-stable products appearing in Figure 6-3 can be assigned α_N products decaying to β_N* and CO_2.

Figure 6-5 shows the extent of reaction versus cluster size, for the reaction channels in Scheme 1. These were calculated from the abundances from Figure 6-3 where no attempt was made to account for the meta-stable (β_N*) decay products. An odd-even N reaction dependence is observed throughout the cluster sizes studied. Even-N C_N^- clusters are more reactive (fewer parent C_N^- clusters remain) from N = 6 to 20 while odd-N C_N^- clusters are more reactive from N = 21 to 27.

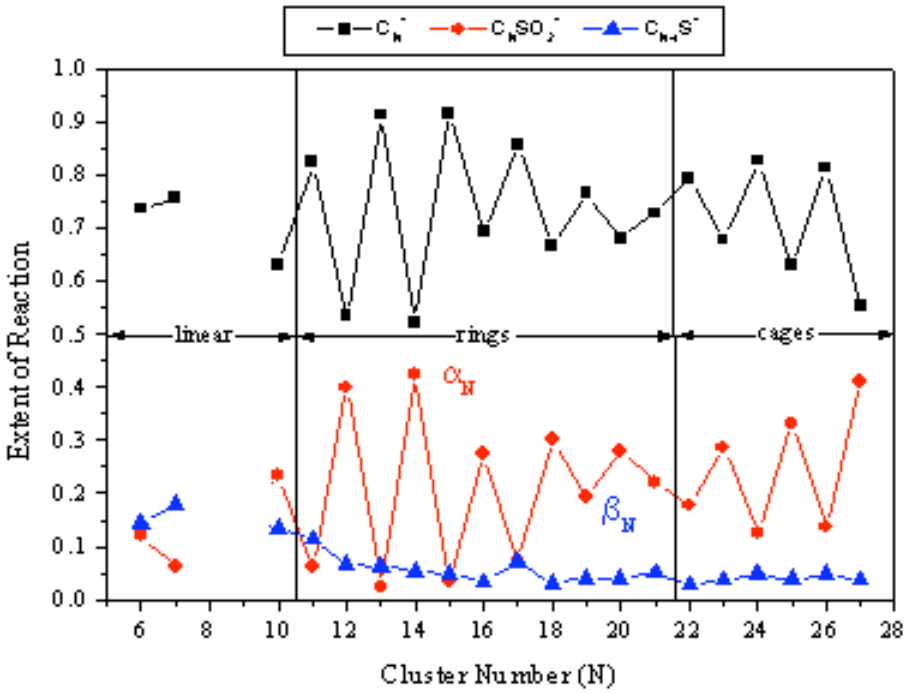

Figure 6-5: The extent of reaction for each carbon cluster anion is shown with regions of defined reactivity. Previous structural assignments of linear, rings, and polycycles or cages were correlated with reactivity. Though linear structures dominate from N = 4 to 10, only N = 6 & 7 are shown. Generally even-N clusters are more reactive in this linear region. Ring structures dominate from N = 11 to 21 showing the greatest extent of reaction for all isomers with a very strong odd-even dependence favoring the even-N clusters. The cage structures dominate from N = 22 and higher as evidenced by a strong odd-even N dependence on the extent of reaction. This dependence could be attributed to the simple adsorption of one or more SO_2 molecules to the less reactive even-N cluster (fullerene structure) as compared to the more reactive odd cluster (non-fullerene structure).

This size dependence can be explained by the well-established transitions in the structural and electronic characteristics of the C_N^- anions. Previously, Gotts *et al.* measured size-dependent isomers for both the positive and negative ions of carbon.[111] For the carbon cluster anion, linear isomers dominate up to N = 9, ring structures dominate from N = 10 to 40 and fullerenes are possible from N = 35 and greater, though cluster source conditions can affect the distribution of isomers. Given the higher pressures used in this study, fullerenes may be present in greater abundance and at lower cluster sizes than depicted in the work of Gotts *et al.* From N = 23 and higher, this odd-even effect could be due to the presence of caged carbon structures where even-numbered clusters produce fullerenes (less reactive). Note that all carbon cluster anions are open-shell radicals in which no preferential odd-even N effect is seen in the pure C_N^- mass spectrum.[111] The lack of an electronic effect points to structural considerations in developing an explanation of the relative intensities.

In order to explore higher temperature reaction channels, SO_2 was seeded into the source buffer gas to allow for the simultaneous presence of SO_2 and nascent carbon clusters at the moment just after the laser ablation of carbon. The results are shown in Figures 6-6 (A-C). The carbon clusters are present with a higher partial pressure of SO_2, free electrons, and higher reaction temperatures than present in the reactor. Figure 6-6(a) shows the resultant low-N mass spectrum from the injection of SO_2 in the cluster source. As in the case of the reactor experiments described above, the α_N ($C_NSO_2^-$) and β_N (C_NS^-) products are present. On close inspection of the unreacted C_N^- peaks, an isotopic abundance analysis reveals a significantly enhanced (*m+2*) peak confirming the presence

of ^{34}S. Thus sulfur is present in a reaction product that is mass coincident with C_N^-. A product assignment based upon the third reaction in Scheme 1 was assumed.

$$C_N^- + SO_2 \rightarrow [C_N^-\_SO_2] \rightarrow C_{N-1}SO^- (\gamma_N) + CO \qquad (3)$$

Given that no meta-stable decay peaks are apparent in the spectrum, a straightforward conversion of C_N^- to the α_N, β_N, and γ_N products is inferred. Preliminary results obtained by heating or cooling the reactor indicate that the α_N process decreases with increasing temperature, suggesting it is a non-activated, reversible binding, whereas the β_N process increases with temperature, consistent with an activated, irreversible process (CO_2 elimination), as also concluded from the analysis of the metastable decay process (collisional activation leading to dissociation). In the low-N spectrum, the even-N clusters (N = 6, 8, and 10) do not undergo partial oxidation to produce CO. Finally, SO_2 introduced in the flow reactor can produce cluster anions ($S_nO_m^-$) where n = 1, 2 and m = 2 – 6, due to their favorable electron affinities.[112,113] These ($S_nO_m^-$) peaks are mass coincident with both parent and product peaks thus adding to the apparent intensity (area) of the peak.

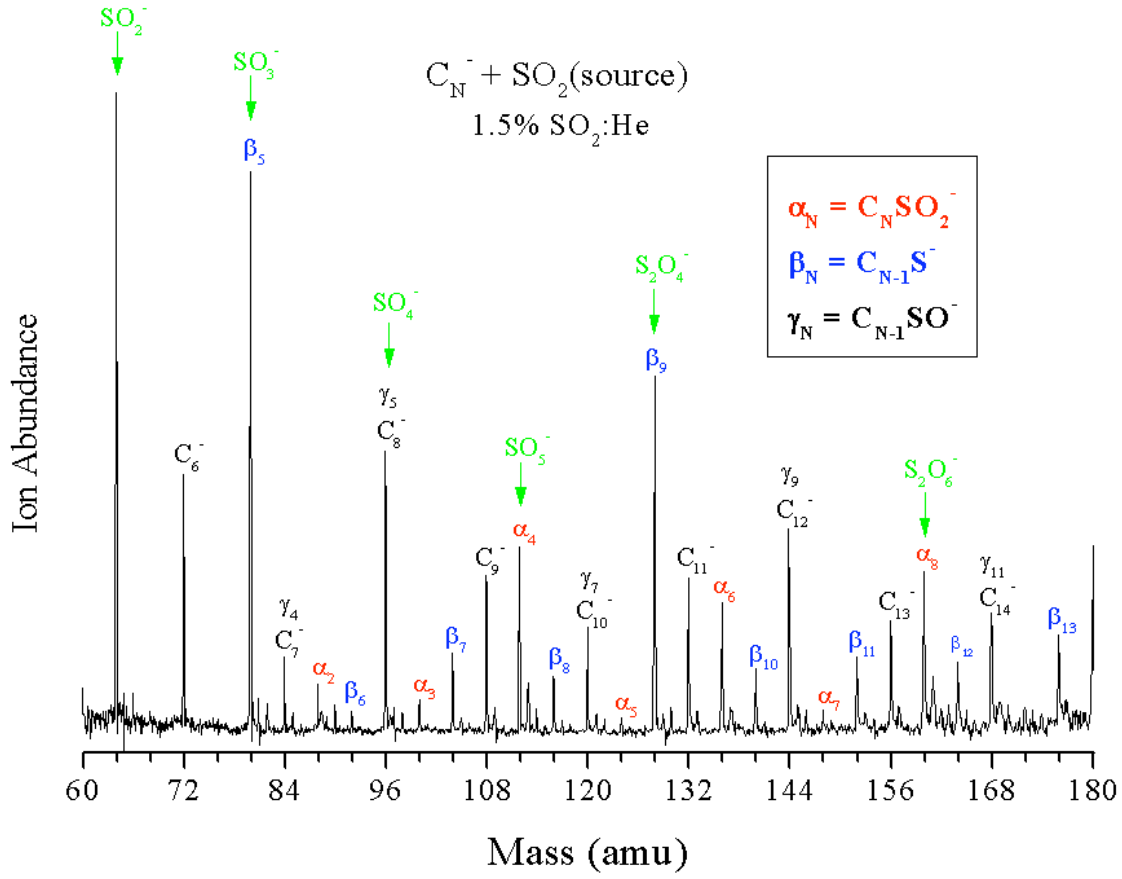

Figure 6-6(a): A low-N mass spectra of thermalized carbon cluster anions, C_N^-, in the region of C_6^- - C_{15}^- without (A) and with (B) exposure to a dilute amount of 1.5% SO_2:He in the cluster source at room temperature. In addition to $C_NSO_2^-$ (α_N) and $C_{N-1}S^-$ (β_N), the product $C_{N-1}SO^-$ (γ_N) was identified. This product is mass coincident with the parent C_N^- cluster and the assignment was based upon an isotopic sulfur analysis.

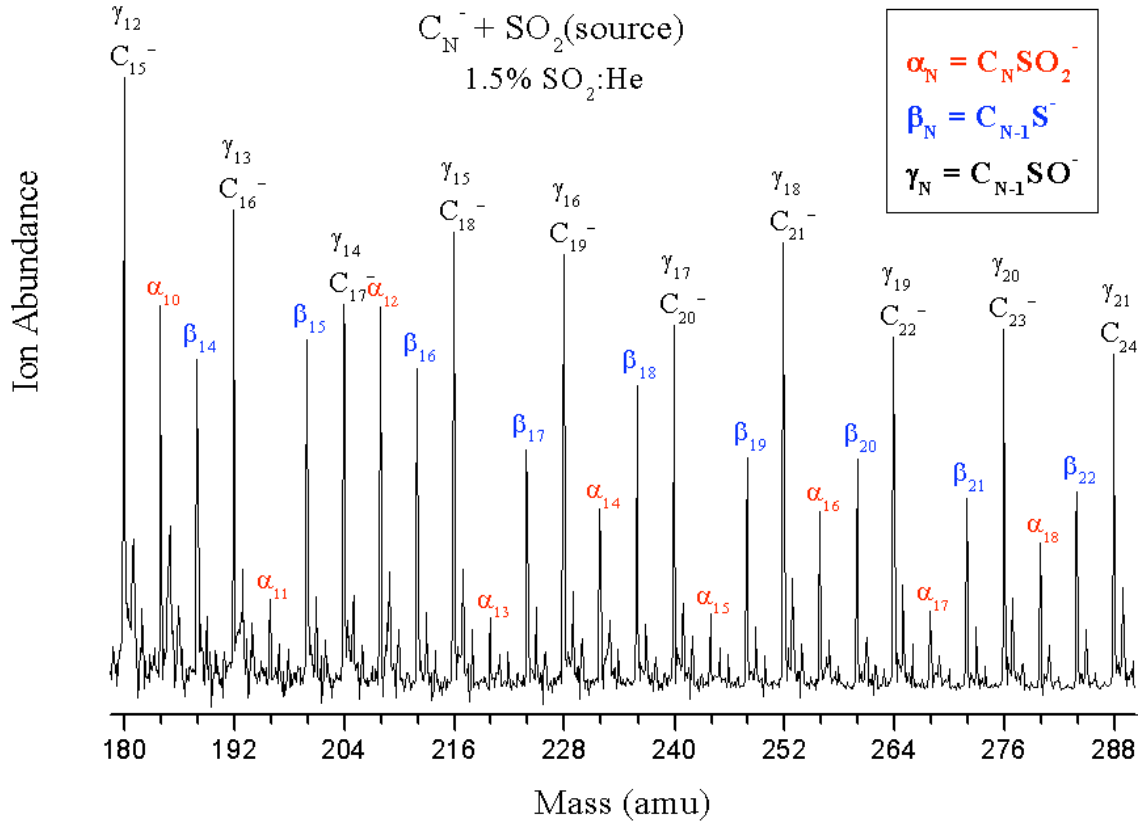

Figure 6-6(b): Same as (a), but showing region C_{15}^- - C_{24}^-. The formation of $C_NSO_2^-$ (α_N) for odd-N clusters is not favored from N = 11 – 21. By N = 23, the formation of $C_NSO_2^-$ (α_N) for odd-N clusters is slightly favored over even-N clusters.

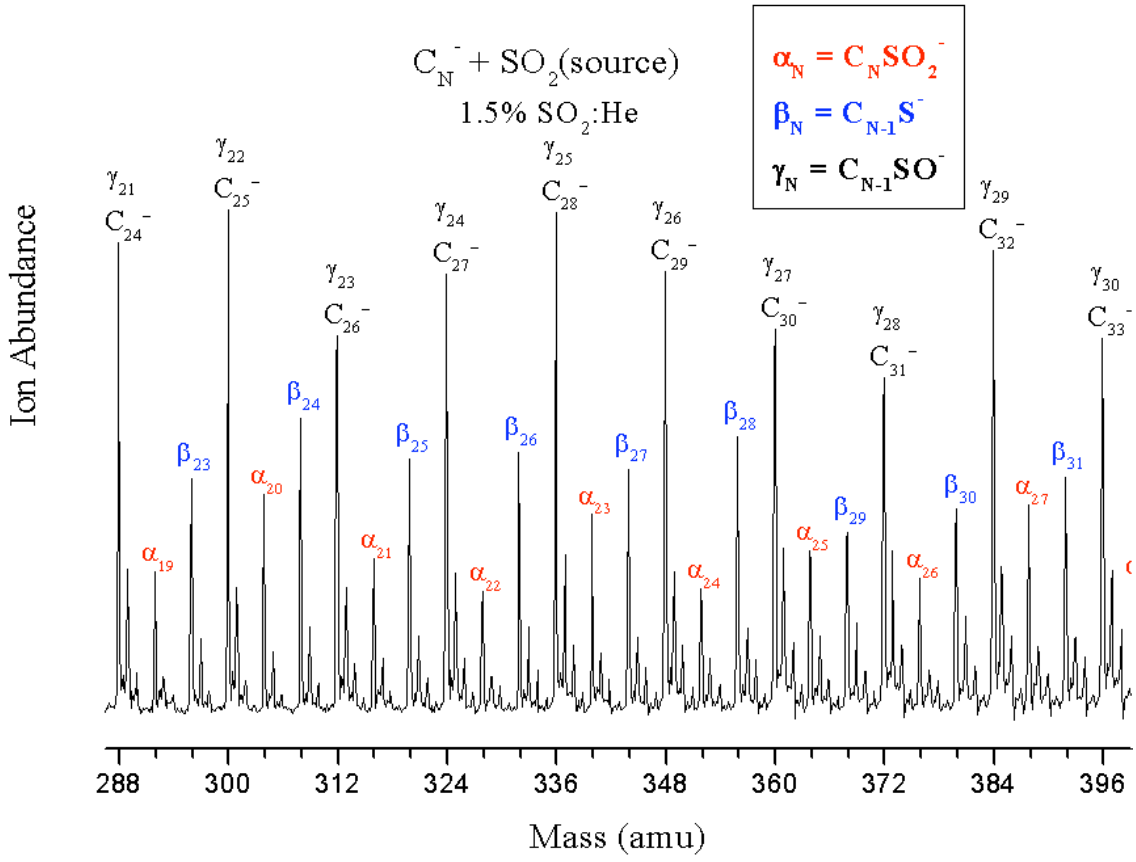

Figure 6-6 (c): Same as Figures 6-6(a) and 6-6(b) displaying the clusters C_{24}^--C_{33}^-.

Figures 6-6(b) & (c) show the high-N mass spectrum of C_N^- reacting with SO_2 seeded in the source gas. Since the γ_N product peak is mass coincident with the C_N^- parent peak, quantitative analysis of the extent of reaction is not possible under these conditions. The odd-N α_N products (N = 11 – 17) are not favored when compared to their corresponding β_N products and perhaps γ_N products. This suggests the α_N product is most likely unstable (higher energy) preferring conversion to the β_N and γ_N products. As N increases, the even-N clusters become less reactive while the reactivity of the odd-N clusters increase. By C_{23}^-, no odd-even alternation is discernable possibly due to the addition of the γ_N product to the remaining C_N^- peak masking any intensity alternation.

6.3 Conclusions.

We conclude by briefly describing the results of a series of broader experiments that have been carried out to address the robustness and generality of our principal findings. In the absence of a fast, in situ thermometry, we have been very concerned to establish that these SO_2 reactions are taking place with properly thermalized carbon-cluster anions. Toward this end, we have carried out a long series of control reactions, with various reactants introduced in the same manner and over the same concentration-range as for SO_2. No evidence for reactions or reaction products could be detected by introducing O_2, NO, N_2O, or H_2O into the room-temperature reactor. Addition of NO_2 to selected carbon clusters could be detected, barely above the detection limit, at least 100-fold less efficient than SO_2. Our conclusion is thus that carbon-cluster anions produced and thermalized in this source are reacting in a highly selective manner with SO_2, rather than indiscriminately as would be expected from uncooled clusters. We have separately

introduced saturated water-vapor into the (helium) carrier-gas, which allows one to detect hydrated carbon-cluster anions as well negatively-charged water clusters, $(OH^-)(H_2O)_m$, m = 1 to 8. These relative abundances of these clusters are consistent with a temperature below 100 ºC.

The carbon-cluster anions appear to be inactive toward water when it is introduced as saturated water-vapor into the reactor, in contrast to the experience with alkali-halide and metal-oxide clusters generated in the same source, and thus consistent with the general inertness mentioned above. A much higher (100-fold) partial-pressure and relative humidity RH can be generated by introducing saturated water-vapor into the cluster-source region, in which case hydrated carbon-clusters as well as hydrated-hydroxide clusters are readily detected. The relative abundances of the latter can be used along with established thermochemical parameters as a thermometer and hygrometer. However, the hydration is readily replaced when SO_2 is then introduced into the reactor zone. If the carrier helium contains both H_2O and O_2, hydrated-superoxide clusters are detected along with carbon-cluster-anions, but the SO_2 reaction appears to proceed as before.

Preliminary results obtained by heating or cooling the reactor indicate that the α_N process decreases with increasing temperature, suggesting it is a non-activated, reversible binding, whereas the β_N process increases with temperature, consistent with an activated, irreversible process (CO_2 elimination), as also concluded from the analysis of the metastable decay process (collisional activation leading to dissociation).

As compared to other black-carbon soot models, such as graphite, activated carbons, or lab-generated soot, the carbon clusters show extraordinary higher activity for

adsorption and reaction with SO_2. This likely reflects the greater concentration of exposed reactive sites and the unrestricted access to such points. The unexpected ambient-temperature oxidation of the carbon cluster anions by SO_2 to produce $C_NSO_2^-$, $C_{N-1}S^-$, $C_{N-1}SO^-$, CO, and CO_2 may suggest an alternate mechanism for the uptake of SO_2 in the troposphere where C_N^- serves as a surrogate for carbon soot. The possible production of carbon-sulfur compounds in point source plumes that goes on to participate in other atmospheric reactions and play a role in the soot-SO_2 health issues raises questions for further study. This study provides an example of the use of clusters to model the interaction of small particles such as soot with environmentally relevant gases in the atmosphere.

CHAPTER VII

CONCLUSIONS AND FUTURE WORK

The experiments presented in the previous chapters have shown appealing results toward many interesting problems. Each set of experiments have opened new opportunities for a continuation of experiments. This chapter presents some discussion of experiments that should be done to continue research on the gas phase reactions imparted earlier. With in this discussion, some new nonessential results are presented as part of a hodge-podge of experiments that are extensions of some reports that have been published on a particular topic. Other experiments presented are preliminary experiments that have not yet been revisited by the researchers in this laboratory.

7.1 Vanadium Oxide Clusters.

The research presented in Chapters III, IV, and V have shown exciting results for anionic clusters of vanadium oxide. In previous reports, these clusters have displayed little or no reactivity. The idea to tune the oxidation state of the vanadium atoms has never fully explored in any reports. This is a key concept when relating cluster studies to and surface chemistry. After initial understanding of the fully oxidized system, it is then necessary to explore defects sites whether in order to model surfaces or to explore the

resilient nature of the clusters themselves. Developing nondestructive techniques to introduce defect sites will be a must, thus the benefits of oxidation state tuning.

A great deal of the work performed on vanadium oxide clusters was motivated by the predictions of cage-clusters that have been calculated using high level Density Functional Theory by Vyboischikov and Sauer.[39,40] The resistance to adsorption shown in Chapter IV and elsewhere [18] supports the claims made by the theoretical study that the larger vanadium oxides are very stable.

With such an ultra stable prediction, researchers should set out to find uses for these materials as well as reliable means of production. The robust clusters anions that have been described in Chapter IV, are readily produced in the gas phase as cationic[18,79], anionic, and neutral[23] species. Characterization of these particles for use, if only as used as standardizing materials, should be preformed.

The 2001 report from Vyboischikov and Sauer[39] does not include all cluster clusters from V_4O_{10} to $V_{24}O_{60}$ as shown in Chapter III. The calculations only include those that are a multiple of V_2O_5. This means only clusters containing an even number of atoms were calculated. In the experiments shown in Chapters III, and IV, clusters containing odd and even vanadium atoms were shown to be reactive and as robust as those that were calculated previously. It may be found that certain geometric shapes can be attributed to the resilient nature of the odd vanadium clusters as well. The first and foremost problem that is presented is the that the odd vanadium clusters are not as easily fitted to closed geometric Figures as the even numbered clusters are. For most of the favorable geometries found for the even vanadium oxide clusters, a geometric shape with an even number of vertices is found to be the most stable structure. For example, a

tetrahedron was found to be the best geometry for V_4O_{10}. At each vertex of the tetrahedron reside a V=O unit and along each edge a bridging oxygen atom. To assign similar closed structures to the odd number vanadium oxides is more difficult. For a cluster containing an odd number of vanadium atoms, selecting geometric figures that resemble closed figures, such as a cube, a tri-prism, or an icosahedron, is not trivial. Mostly because highly symmetric figures that are suitable and obey the bonding rules of said molecules are not known by mathematicians. This may mean they don't exist. In order to attempt to fill in the gaps in the alternative structures is that are neither closed structures or hollow cages may be considered. Structures have been identified in the polyoxometallate (POM) field, but for multiply charged species such as $V_5O_{14}^{3-}$. Although similar stoichiometries are identifiable between the two field, the POMs are always multiply charged. Figure 7-1 shows the results of a calculated structures for $V_5O_{13}^{-}$. The structure was calculated using the techniques described in Chapter V. Briefly, a B3LYP correlation functional with an Ahlrich's TZV basis set as used by Vyboischikov and Sauer[39]. The structures are converged to a minimum energy, but not a global minimum. The calculations yielded imaginary frequencies for the converged structures that pertained to the oxygen atoms that bridged the top VO_5 molecule to other four vanadium atoms. Due to the time it takes to calculate these structures, not many attempts were made to explore the problem. A more dedicated theorist may not find a more trivial way to solve this problem.

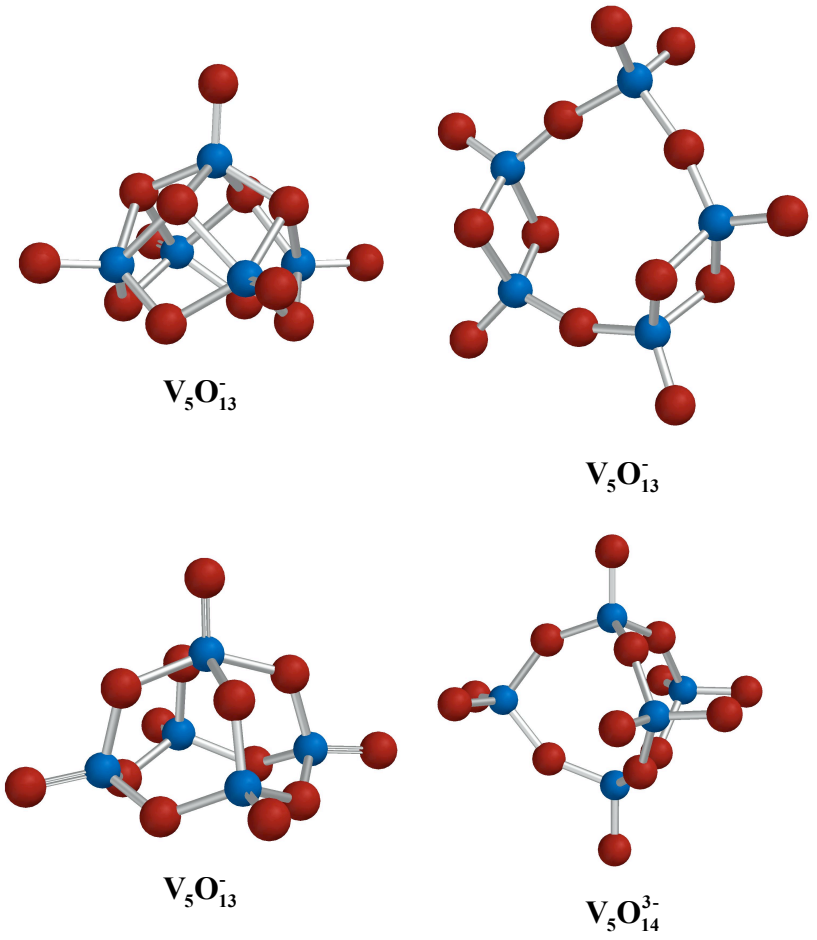

Figure 7-1. DFT calculated structures for $V_5O_{13}^-$ and $V_5O_{14}^{3-}$.

Another anion that hasn't been reported is $V_3O_9^-$. This molecule has been isolated and crystallized as $V_3O_9^{3-}$ and reported previously.[35] However, in our experiments it shows up as a singly charged anion. An early investigation by Vyboishchikov and Sauer [40] investigated some tri-vanadium complexes, but did not investigate $V_3O_9^-$. It has been shown in our experiments to readily adsorb water as well. A preliminary investigation of the structure and the hydrated forms are shown below in Figure 7-2.

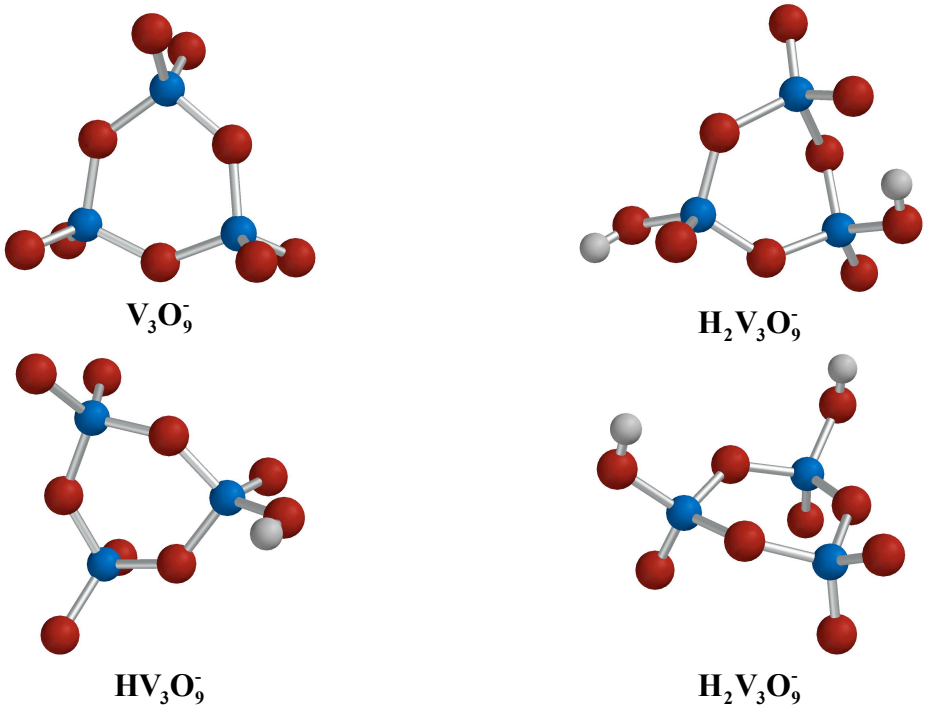

Figure 7-2. DFT calculated structures for $V_3O_9^-$, $HV_3O_9^-$, and $H_2V_3O_9^-$. The $H_2V_3O_9^-$ variants have two considered structures concerning the hydrogen atoms. The top depicts a trans- form while the bottom shows a cis- form.

Aside from theoretical studies, many other studies can be performed on the vanadium oxide complexes including a multitude of molecules have been studied by Castleman and co-workers.[18-20,49,54,80,86,114-120] Exploring some of these systems here in our experimental set up may add to what has already published. They easily observe many of these molecules fragment when interacted with hydrocarbons. This relatively easy to find when studying mass selected clusters, however our studies are done collectively with out mass selectivity. It may be interesting to study a system that is know to fragment and gain a perspective on what will be observed in our experiments. Furthermore, our studies are on the order of 150 to 300 torr, where the experiments performed by Castleman and co-workers are done at < 1.0 mTorr. [121] Higher pressure may yield more stable clusters

with out fragmentation and add to the kinetic and equilibrium information on these systems.

The reaction studies reported in Chapter IV and V have several open avenues for continued work. First and foremost is to study the cationic vanadium oxide clusters and their interactions with SO_2. It would be interested to find out whether cations display the same robustness as the anions when fully oxidized. A study of this sort would most definitely support or refute the idea presented by Vyboischikov and Sauer that these clusters are as stable as theoretical calculations tell us.

Further experiments would include temperature dependent studies to determine the nature of adsorption, whether it is in kinetic or equilibrium control. Preliminary studies on temperature dependence were very clear and very inconsistent. This could be for several reasons. Experimental subtleties could have been over looked. The dependence on partial pressure could have also played a key role in inconclusive results. Since there is no way to monitor the total pressure of the reaction cell, variations of the total pressure with increased or decreased temperature can not be monitored. This will most definitely alter all the partial pressure.

The reactions performed under conditions where a high oxygen content gas mixture was used to prepare the vanadium oxide anions presented the possibility that a great amount of oxygen was present in the reactor. This most definitely affects the observed results when an interacted with gases in the reactor. No longer is the experiment observing a single component, but two components: the reactant gas and the additional oxygen. Moving away from using oxygen in the cluster source will ultimately correct this problem, as was found in later experiments when the amount of oxygen was

reduced. But if the dependence of oxygen in the carrier gas was removed, this issue would be as well. It is possible to use N_2O as a source of oxygen in the cluster source.[23,79] This would greatly reduce the likelihood that residual oxygen will play a part in the reactor. The dependence of an additional gas could be removed completely by using an alternate target rod. A target rod that is composed of V_2O_5, VO_2, V_2O_3, or $NaVO_3$ would most definitely remove all dependence on mixture carried gas in the source. This would also be a great technique to search for magic number. Using the current method of clusters production discussed in Chapter III, no magic number are observed. This has been the case in other cluster systems as well.[122] In contrast to removing additional gases down stream, introducing more gases would be interesting as well. The addition of H_2O with SO_2 may provide interesting results. Two approaches can be taken to accomplish this experiment: First the SO_2 and H_2O could be introduced simultaneously through the same valve. However, this does not allow for independent control over each reactant. An alternate approach would be to add a second reaction valve to the flow tube reactor. This can be easily accomplished by using the modified expansion piece discussed in Chapter II. This would provide an ultimate arsenal of experimental options that would undoubtedly provide an ample amount of research, data, and seemingly limitless research that could be extended to atmospheric-like conditions.

Aside from vanadium oxide clusters, the opportunity exists to study other reducible metal oxides. Immediately, niobium oxide and tantalum oxide are obvious choices for comparison and have been used by Castleman and co-workers.[123-125] Not only can metal of the same group be studied, but oxide cluster of Ti, Cr, Mn, Mo and W could be investigated as reducible metal oxides as well. Furthermore, all of the work

presented on the vanadium oxide anions here could be performed using these materials as well as the future directed research.

7.2 Carbon Clusters.

The work on the carbon clusters has indeed been very productive. Future directions of this work should include extending the experiments to larger clusters up to and including C_{60}, C_{70} and C_{80}. A study of variable temperature and increased reactor pressures should also be performed after the thorough investigations at ambient temperature are fully understood. As rewarding as these experiments can be, there is a limit the experiments. There is no option to change the material or its composition. Only reaction conditions can changed. Further physical properties could be investigated using electron detachment techniques, but the chemical reactivity studies are a finite unless new experiments are devised.

7.3 Alkali Halide Cluster.

Previous studies of alkali halide systems have provide intriguing adsorption-desorption results.[126,127] The use of these systems could be implemented again as calibration methods as many reactions are well known that involve charged alkali halide clusters and halide ions.[128] Beyond interest in the laboratory, alkali halide particles are of atmospheric relevance as well.[42] On going studies to date include the interaction of SO_2 with sodium chloride anions, $(NaCl)_NCl^-$. Some preliminary studies are shown in Figure 7-3 below.

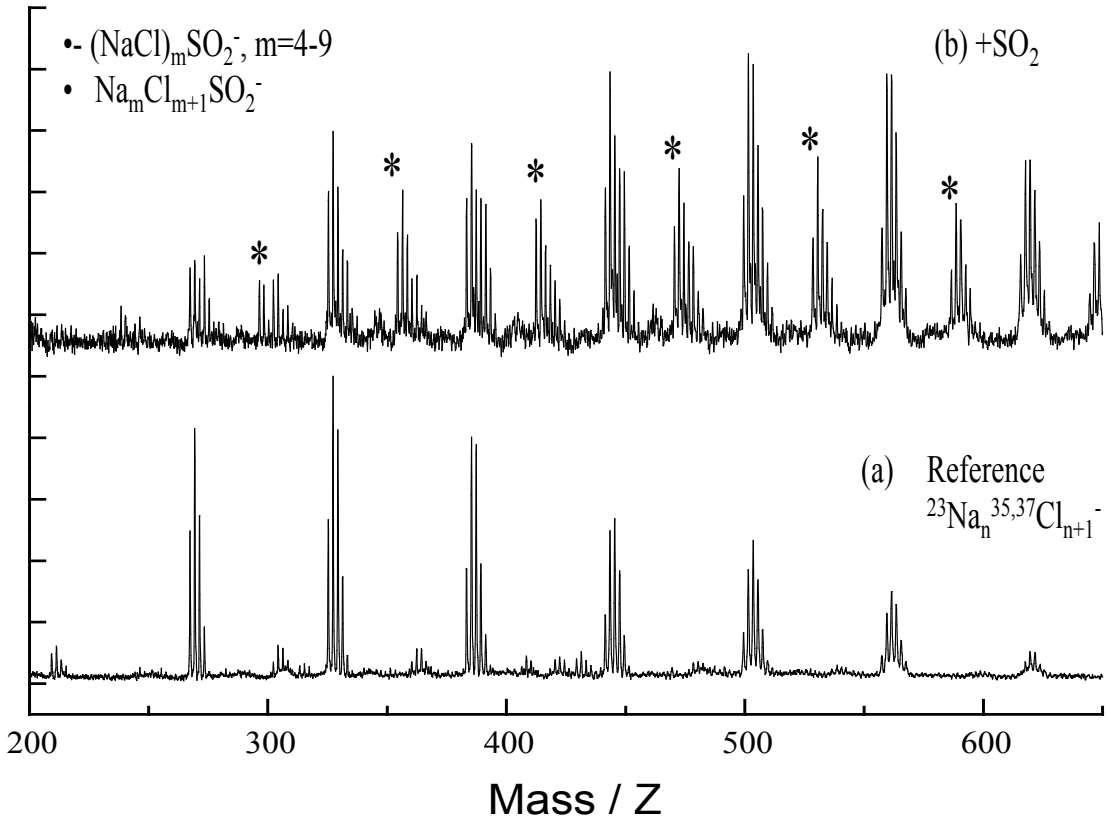

Figure 7-3. Sodium Chloride Anion spectrum and reaction with SO_2. Spectrum (a) shows a reference mass spectrum of sodium chloride anions beginning with the $Na_3Cl_4^-$ at left most peaks and highest clusters shown are $Na_{10}Cl_{11}^-$. Spectrum (b) is the result after addition of SO_2 to the flow tube reactor. The new peaks consist of clusters corresponding to $(NaCl)_NCl^-$, $(NaCl)_NSO_2^-$ and $(NaCl)_NCl{\bullet}SO_2^-$.

The reaction with SO_2 yields new peaks that include $(NaCl)_NSO_2^-$ and $(NaCl)_NCl{\bullet}SO_2^-$. One hypothesis of the process occurring is that the neutral $(NaCl)_N$ clusters are absorbing and SO_2 and showing up as a negatively charge cluster. A second hypothesis is that multiple SO_2 molecules are interacting with the additional Cl atom on the negative clusters described as follows:

$$(NaCl)_NCl_N^- + SO_2 \longrightarrow (NaCl)_N^- + ClSO_2$$
$$(NaCl)_N^- + SO_2 \longrightarrow (NaCl)_NSO_2^-$$

Further investigation is needed to resolve the details of the problem as well as other atmospheric relevant processes.

CHAPTER VIII

NEAR-INFRARED ABSORPTION & LUMINESCENCE BANDS IN *NM*-SCALE METAL PARTICLES:

THE CIRCULATION-FREQUENCY RESONANCE AT $HV_F/\pi D$

The recently discovered near-infrared absorption and luminescent bands of smaller metal nanoparticles are explained as a resonance arising from the circulation of the most energetic conduction electrons. This surprisingly distinct and long-lived resonance phenomenon, which lies beyond the predictions of the standard (Mie) theory, coexists and competes for intensity with the familiar giant-dipole (plasmon) resonances at higher energy. The size-dependence of the circulation-resonance frequency is contrasted with that of the intrinsic band-gap of semiconductor nanoparticles.

8.1. Introduction.

Discrete metal nanostructures possess a set of unique properties that underlie both long established as well as emerging applications. The centuries-old art of incorporating them into optical materials is based on the permanence of their colors and intense iridescence, in transmitted or reflected light.[129] Their widespread inclusion in practical catalysts is based on their resilient adsorption and capacitive (redox) properties.[130] Bioconjugate probes take advantage of their robust, strong scattering for contrast under the electron or optical microscope.[131,132] Their quantized conductance[133] and capacitance[134] properties underlie existing resistor technology (cermets) as well as emerging applications in nano-electronics, electro-catalysis, and sensors. However, metal nanostructures generally have very poor luminescence properties, compared to materials that have an intrinsic band-gap, such as organic dyes or semiconductor nanostructures.[135] Their strong interactions with light — absorption, refractive, and nonlinear optical properties[136] — arise instead from collective resonances (plasmons) that are too short-lived for significant luminescence, unless they are coupled into extended (many 10s or 100s of nanometers) antenna-like plasmonic structures, for near-field microscopy[137] or surface-enhanced raman spectroscopy.[138]

It is therefore a surprising result, as recently reported, that isolated smaller metal particles (diameter $D < 2\text{-}nm$) exhibit distinct absorption and emission (luminescence) bands, in the near-infrared (NIR) spectral region.[139,140] These bands, which shift toward higher energy with decreasing diameter, appear to be located at the onset, or edge, of measurable absorption, while the luminescence band is shifted to slightly lower energy

and can have an efficiency approaching one percent, even at room temperature. An improved understanding of this luminescent phenomena may lead to strategies for its enhancement and application, e.g. in hybrid (microscopy, capacitance, conductance) – luminescence sensors or probes.

These bands are *not* predicted by the standard electrodynamical (Mie) theory,[141] which uses the empirical dielectric functions of the bulk metal to calculate the spectrum of a nanostructure of specified size, shape, and surrounding medium. A particular success of the Mie theory is that it accounts for the features of the giant-dipole (GD) resonance, or surface-plasmon band, which is understood as a collective oscillation of the plasma of free, or conduction, electrons of the zero-valent metal.[142] (Because of this success, the GD band is often regarded as a signature property of the finite metallic state, although there are circumstances involving elemental metals and alloys where the conduction electrons do not give rise to a recognizable GD band.)

The emergence of the NIR bands in smaller particles may coincide with a severe broadening of the higher-energy GD band, to the point where it can hardly be recognized. The question naturally arises: Do these effects in tiny metal particles signal the loss of their metallic character? An intrinsic band-gap, with associated absorption edge and luminescence phenomena, could arise from increased electron correlations (amounting to a metal-to-insulator transition), or from electron transfer to adsorbate groups (a metal-to-semiconductor transition). In either case, the GD resonance based on the conduction-electron plasma could not be expected to survive.

Instead, the purpose of this note is to explain how the NIR bands can be reconciled with the standard electronic structure and dynamics of small metal spheres.

We stress here that first-principles calculations have *always* predicted that certain low-frequency transitions could co-exist, and compete for intensity , with the broad GD band centered at higher energy (Figure. 8-1).[143-148] However, these transitions have not been emphasized, because of their presumed experimental inaccessibility. Their recent emergence may thus be attributed to improved sample quality — homogeneity and photo-stability — as well as to enhanced sensitivity in the NIR region.

To promote the widest understanding and application of the essential phenomenon, we have reduced the effect – the size-dependence of a low-frequency, dipole-allowed resonance —to its physically simplest form, as a resonance occurring at the *circulation frequency*, CF, of the most energetic conduction electrons, orbiting the particle's circumference, πD, at speed v_F, Figure. 8-2. (An alternative formulation has been given earlier by deHeer[149], but without an emphasis on the spectroscopic transitions involved.)

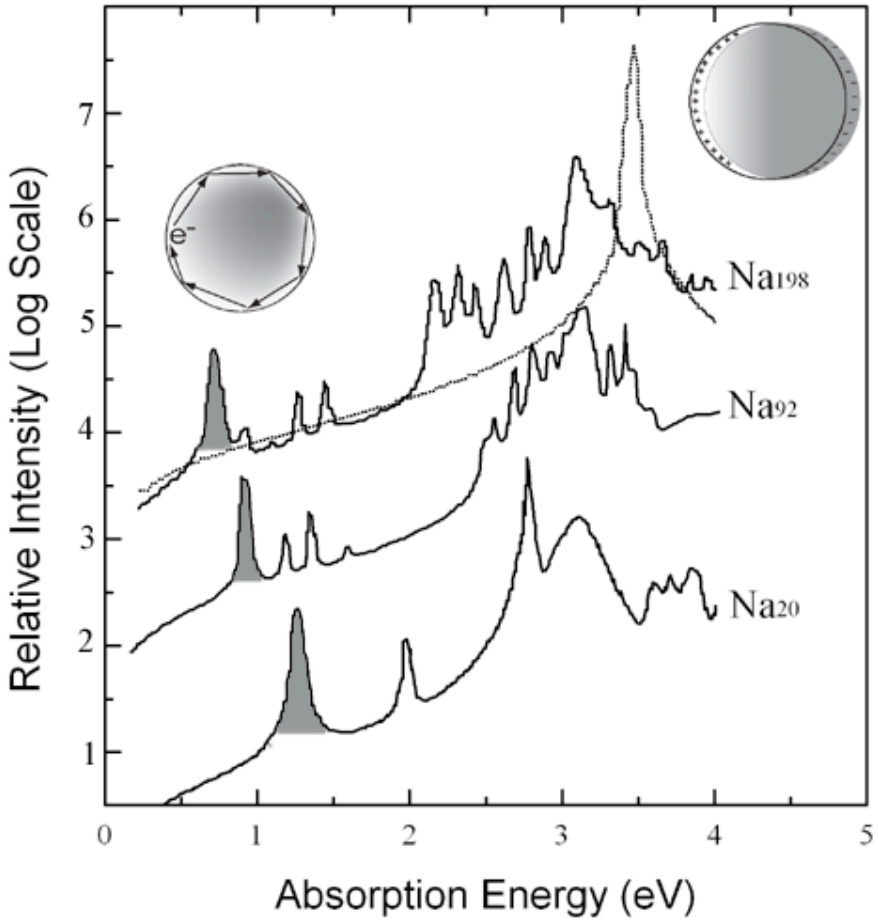

Figure 8-1. A plot of the calculated absorbance spectrum for Na_{20}, Na_{92} and Na_{198}, adapted from ref [143].

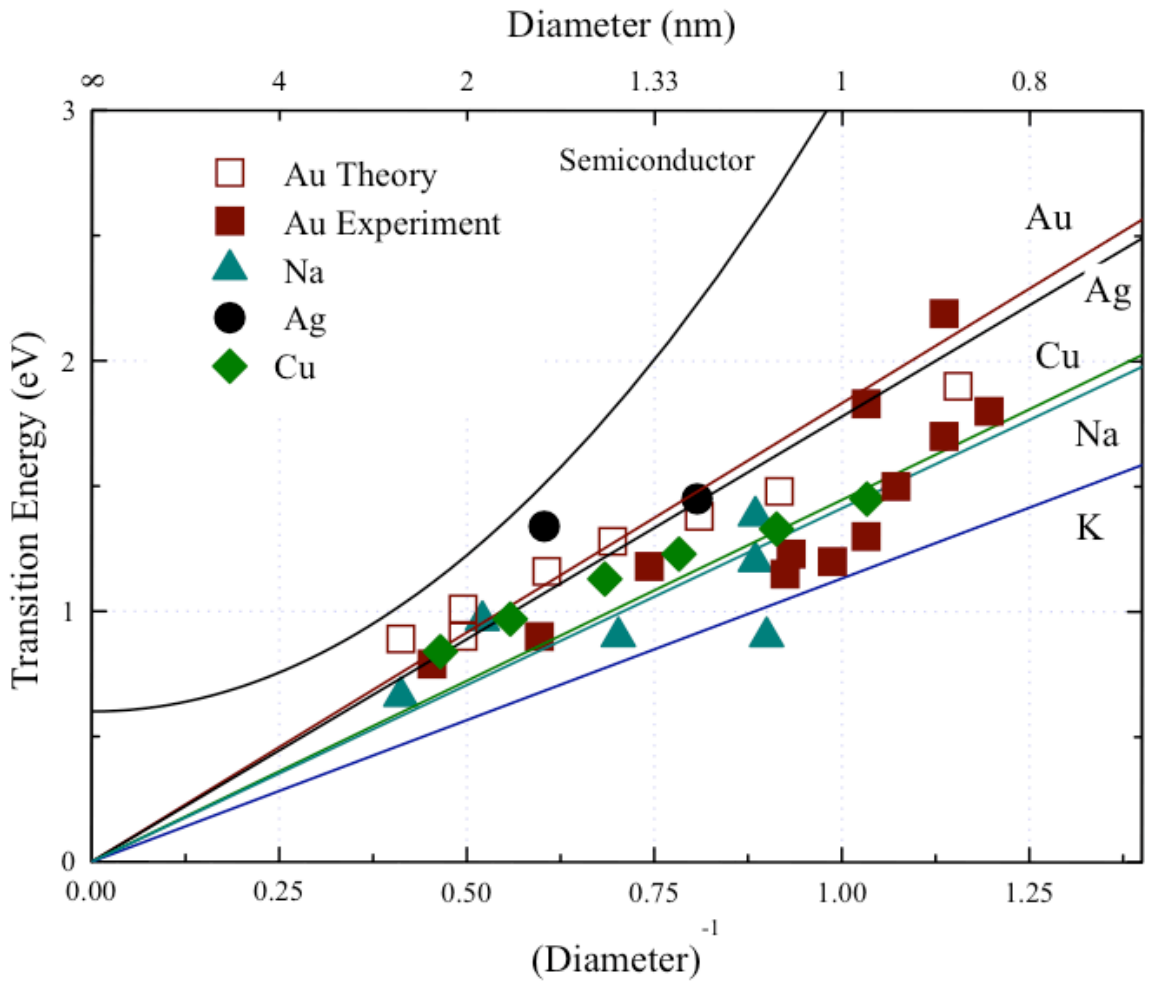

Figure 8-2. Plot of the resonant frequency energy as a function of the (diameter)$^{-1}$.

In the following, we first summarize the theory of the GD transition, as it applies to monovalent metals, with particular reference to its size-dependence, or lack thereof. This is contrasted with the strongly size-dependent quantum electronic structure and dynamics of spherical metal particles. A key result can be quantitatively captured in a simple formula for the lowest-energy allowed transition. We conclude by interpreting this transition as a CF resonance, and distinguish it from similar quantum size-effect phenomena in materials and structures.

8.2. Collective excitations: the giant dipole resonance.

According to the standard (Mie) theory[141], a spherical particle in a surrounding medium may rise to a giant-dipole resonance at frequency ω_{GD}, when the condition

$$\varepsilon_1(\omega) \Leftrightarrow -2\varepsilon_m \qquad (1)$$

is met. Here $\varepsilon_m(\omega)$ is the dielectric constant of the medium, and $\varepsilon_1(\omega)$ is the real part of the dielectric function of the particle, which is assumed to have the exact (empirical) form of the bulk. For metals, $\varepsilon_1(\omega)$ may be decomposed into separate contributions from the conduction-electron "plasma" and the core electrons bound to the metal-ions,

$$\varepsilon_1(\omega) \cong \left\{1 - (\frac{\omega_P}{\omega})^2\right\}\varepsilon_0 + \varepsilon_{core} \quad , \qquad (2)$$

where $\omega_P^2 = \rho\ e^2/\varepsilon_o m_e$ is the so-called plasma frequency determined by the conduction electron density, ρ, and the effective mass, m_e. Inserting (*2*) in condition (*1*), gives a convenient formula for the plasmon (GD) frequency:

$$\omega_{GD}^2 = \frac{\varepsilon_0}{2\varepsilon_m + \varepsilon_{core}} \omega_P^2 \quad . \qquad (3)$$

Table 1 collects the GD resonance frequencies predicted by this simple expression for monovalent metals of varying densities and ion-core polarizabilities, which agree well with experiment.

It is important to recognize that, within this theory, the frequency of the GD resonance is medium-dependent, but *size-independent*, as is its shape, or bandwidth. Size-dependent shifts and broadening are obtained only by incorporating additional effects. The largest and best understood of these is the so-called 'spill-out' effect, wherein the conduction electron density of a metal structure extends beyond its nominal surface, even in neutral (uncharged) particles. This effect reduces the electron density (ρ), in small particles, from that in Table 1, and increases its electrical polarizability. In the alkali-metals (small ion-core polarizability), the well-known result is a reduced GD resonance frequency, i.e. a *red-shift*. Contrariwise, in the noble metals (*Cu, Ag, Au*), spill-out introduces a *blue-shift* at small sizes, because the conduction electrons extend over a volume significantly larger than that containing the highly polarizable d^{10} ion-cores. Depending on the metal, a large blue-shift may cause the GD resonance to overlap

the absorption bands originating from the d-electrons, resulting in a severe broadening. [150-152]

We believe this account of the modest frequency shifts and broadening is both well founded and general — in the sense of co-existing with the quantization effects described next — in contrast to the models invoking ad hoc surface scattering or adsorbate bonding effects, which are incompatible with discrete resonance structure.

8.3. Electronic structure and dynamics of small metal spheres.

The very same conduction electrons that collectively constitute a plasma (above) may also be regarded singly as occupying delocalized orbitals, at respective energy levels ranging from the bottom of the bulk conduction band up to a highest-occupied orbital (the Fermi level), some E_F higher in energy.[1] (Although this picture may seem incompatible with the plasma model, photoelectron spectroscopy of ultra thin metal films and of globular clusters leaves no doubt that these energy levels can be sharply defined.) For a neutral particle of a monovalent metal, the number of conduction electrons equals the number of atoms, N, and the *mean* energy spacing of the occupied levels is simply $\sim E_F/2N$ (including spin). This parameter has long been used to express the scale of quantization effects lying outside the range of the bulk dielectric function, e.g. (*2*).

However, if the metal particle attains a globular shape, approximated as spherical — just as in the derivation of *(1)* — then the conduction-band energy levels become

[1] *Since this is almost entirely kinetic energy, i.e. of electrons confined to a 'box' the shape of the particle, $E_F = m_e v_F^2/2$ defines the 'Fermi velocity, i.e. the speed of the electron in the highest-occupied orbital. The corresponding momentum defines a (deBroglie) wavelength, $\lambda_F = h/m_e v_F$, another very useful parameter for discussing quantization effects.

highly bunched, much as they would in a giant atom. Each bunch, or "subshell", is classified according to its principle (n) and angular-momentum (l, m_l) quantum numbers, and holds $2(2l+1)$ electrons. Furthermore, these angular-momentum subshells tend to be grouped further into "shells", each labeled by its highest-l component, in a universal aufbau Scheme:

I	II	III	IV	V	VI	VII
$\mid 1s^2$	$\mid 1p^6$	$\mid 1d^{10}\ 2s^2$	$\mid 1f^{14}\ 2p^6$	$\mid 1g^{18}\ 2d^{10}\ 3s^2$	$\mid 1h^{22}\ 2f^{14}\ 3p^6$	$\mid 1i^{26}\ 2g^{18}\ 3d^{10}\ 4s^2$	$\mid 1j^{30}$
2	8	(18) 20	(34) 40	(58) 70	(92) 112	(138) 166	(198)

Scheme 1: *Top*: shell index; *Middle*: orbital labels; *Bottom*: total *e*-count at closings

This so-called spherical shell model, and its spheroidal variants, have been used to account for hundreds of diverse experimental observations, mostly on gas-phase metal clusters ranging from a few up to hundreds or even thousands of atoms, as well as to organize the results of electronic-structure calculations on the same. The quantization effect represented by the gaps between shells is tremendously larger than the mean spacing, and decreases only slowly with increasing cluster size, going as $\sim E_F/N^{1/3}$.

Many observed features of the quantum electronic structure of such metal particles can be obtained from calculations in which the actual cluster structure — i.e. its spatial distribution of ion-cores — is replaced with a positive continuum, a so-called 'jellium', of specified charge, size, and shape. Such calculations also allow for calculation of the electrodynamic response, i.e. the spectroscopic properties of small metal particles, with the conduction electrons treated fully quantum-mechanically.

Figure 8-1 incorporates typical results from such (DFT) calculations, carried for an electron-density appropriate to neutral *Na* clusters, which account for the red-shift of the GD band and also predict one or more weaker bands at lower frequency (NIR region). The latter can be attributed to allowed transitions from the highest-occupied shell to the first unoccupied shell, e.g. in the case of Na_{92}, to the $1h - 1i$ transition of *Scheme 1*, and it is clear that they move to higher frequency with decreasing size. Their strength (intensity), relative to that of the GD band, depends sensitively on the extent of electron correlation (plasma screening). Their integrated intensity is typically much less than one percent of the GD band, yet their potential sharpness implies that their peak intensity can be quite high. (Other results of such calculations are collected in Figure 8-2, and in the *Supplementary Materials* section.) It is the size-dependence of the frequency of these resonances for which we seek a convenient interpretation.

8.4. The circulation-frequency resonance compared to observed low-frequency bands.

The main result can be obtained directly by considering a transition from the $(n,l) = (1,l_o)$ component highest-occupied shell, to the corresponding component $(1,l_o+1)$ component of the first-unoccupied shell. Such a transition clearly satisfies the electric-dipole selection rule $\Delta l = +1$. Because the energy of such states are almost entirely dominated by centripetal motion at the particle radius, R, the transition energy is given by

$$\Delta E_{l_o \to l_o+1} \approx \frac{h^2}{2m_e R^2}(2l_o + 1) \quad . \qquad (5)$$

To express this result in terms of a bulk parameter, namely the Fermi velocity v_F, consider that for purely circular motion at the Fermi energy, an angular momentum may be defined by

$$h \cdot l_F = m \cdot v_F \cdot R \quad , \; l_F \cong l_o + \tfrac{1}{2} \quad ,$$

which follows from l_F being neither l_o nor (l_o +1) but rather halfway between. Carrying out this substitution gives the final result,

$$\Delta E \approx h \frac{v_F}{\pi \cdot D} \quad , \qquad (6)$$

where D is the particle diameter, which shows that an allowed transition can be expected at an energy which scales as the inverse of the diameter of the particle.

Table 1 collects the pre-factor (hv_F/π) for several metals in convenient units (eV-nm), e.g. 1.7 eV-nm for Au, and Figure 8-2 plots the predicted ΔE *vs.* D^{-1} lines for comparison with the results of various electronic-structure calculations as well as recent experiments. It is indeed seen that this result (*6*) can account for the existence and the quantitative size-dependence of NIR (~ 0.5 to ~ 2.0 eV) absorption and emission bands, and provides a satisfactory account for the variations among the simpler metals. At the present stage, there would seem to be no justification, to pursue further refinements to (*6*): such as splittings due to non-sphericity; extension to other shell components (or higher-energy excitations), which may appear as absorbing or as forbidden transitions; or interactions with adsorbates.

Instead, we note here a few aspects of the interpretation of *(6)* and related expressions.

8.4.1. Classical picture of the circulation frequency resonance.

A simple geometric picture enables the visualization of (*6*). Note that the denominator (πD) is the circumference of the spherical metal particle, so that the quantity $\tau = \pi D/v_F$ is simply the period of time for an electron moving at speed v_F to complete a revolution around the rim of the particle (*Figure. 8-1*). The inverse of this quantity, namely $v_F/\pi D$, is therefore nothing other than the *circulation frequency* of these most energetically orbiting electrons. Hence it is proposed that such a transition be referred to CF resonance, to distinguish it from the plasmon (GD) resonance.[153,154] (It may also circulate, see Mason et al.[155], but only when excited by circularly polarized light.) The emphasis on this resonance is justified because it is dipole-allowed, it has a large statistical weight (assuming a filled shell), and is lowest in frequency, by virtue of the circumference being the longest path.

8.4.2. Coupling to radiation.

A fundamental principle of electrodynamics stipulates that absorption or emission of electromagnetic radiation requires the acceleration of a charged particle. In the case described, this is the centripetal acceleration of a single energetic 'free' electron as it circulates the rim of the particle, and the classical frequency is related to the photon energy by the usual relation $\Delta E = h\nu$. If each electron orbits independently of the others, in the usual sense of a self-consistent field, then the coupling is very strong, i.e. the CF may exhaust that electron's contribution to the integrated (sum-rule) absorption strength.

However, as is well known, the motion of conduction electrons in metals is highly correlated, so as to screen an external field, and thereby to cancel the oscillating-dipole associated with single-particle motion. This effect transfers most, but not all, of the coupling strength to the plasma modes, i.e. to the GD resonance in the case of small metal spheres. The relative intensity of the CF resonance is thus a sensitive measure of the incompleteness of the plasma screening. One consequence is a great lengthening of the purely radiative lifetime of the CF emission band.

8.4.3. Scattering (damping) rates and lifetimes.

The quantity v_F/D has long appeared as part of expressions for the broadening (additional width) of the GD band. Specifically, it has been interpreted as a (mean) scattering rate, in the expression, $\omega_{scatter} = A\ v_F/R$. The meaning of the dimensionless pre-factor *A* is not without controversy. *A* is said to take on various values — vanishing (0) if the scattering is elastic, unity (1) if isotropic, (3/4) if diffusive — and it may also be enhanced by "chemical interface effects". If $A = 1$, then the scattering frequency equals that of the CF resonance, but this coincidence does not mean they describe the same phenomenon. It is plausible that the CF excitation remains sharply defined at its low frequency (low photon energy), with a long lifetime (~μs), while at higher energy the GD excitation (plasmon) is severely broadened, to a width of 1-*eV* or more, corresponding to a (mean) lifetime equaling the circulation period of single electrons at the Fermi level.

8.4.4. Contrast to size-dependence of the absorption edge (band-gap) in semiconductors.

The CF resonance in *nm*-scale metal particles lies at an energy so much greater than the mean level-spacing energy that the absorption (and luminescence) bands may seem more like the well-known exciton transitions in semiconductor particles. However, they are easily distinguished, as illustrated in *Figure.8-1* for a small band-gap semiconductor,[156] both by the curvature in the plot of transition energy vs. 1/D and also by the intercept (bulk limit), which is vanishes for a metal but is the bulk band-gap for semiconductors.

8.4.5. Extension to even smaller sizes.

Equation (6) predicts that the CF resonance (absorption edge) will move above 2 eV (*Figure. 8-2*), i.e. into the visible region, as the metal particle diameter is decreased to below 0.9 nm (for Au or Ag, < 20 atoms). Some recent results, e.g. from Dickson et al. on Au_8[157] or Tsukuda et al. with Au_{13},[158] both with efficient visible photoluminescence, would agree with this. These results are too new to say whether the same phenomenon is applicable.

	ρ (nm^{-3})	V_F ($x10^8$cm/s)	ω_p (eV)	$\frac{å_{core}}{å_o}$	ω_{GD} (eV)	ω_{CF}·D (eV·nm)	N_{Atoms} (D=1nm)
Na	26.6 [a]	1.07 [b]	6.0 [c]	1.07[d]	3.5 [e]	1.41	14 [g]
K	14.0	0.86	4.4	1.2	2.5	1.13	7
Cu	84.7	1.11	10.8	18	2.4	1.45	44
Ag	58.5	1.34	9.0	4	4.1	1.78	31
Au	59.1	1.39	9.0	9	2.7	1.83	31

Table1.

a. Electron density see Ref.[159] pg. 150, assuming a neutral cluster and ignoring spill-out.
b. Fermi Velocity taken from Ref. [159] for Na and K. For Cu, Ag, and Au, $V_F \Big/ \sqrt{m_{e(eff)}}$, where $m_{e(eff)}$ is the effective mass of the electron taken from Ref [159] and [149].
c. Plasma frequency as calculated from eq.1.40 Ref. [160] pg.18.
d. Dielectric function of the core electrons as calculated from bulk dielectric functions
e. Giant Dipole Resonance as calculated using Eq. 3 with ε_m=1.
f. Circulation Frequency Resonance as calculated using Eq. 6
g. Number of atoms for a spherical particle with a diameter of 1nm using $N = \left(\frac{D}{2\, r_S} \right)^3$.

Table 2

Metal	Energy(eV)	Ref.
Au_{21}	2.19	1
Au_{28}	1.83	1
Au_{38}	1.23	1
Au_{20}	1.90	2
Au_{254}	0.90	2
Au_{75}	1.18	3
Au_{145}	0.90	3
Au_{330}	0.79	3
Ag_{58}^{+}	1.45	4
Ag_{139}^{+}	1.34	4
Na_{20}	1.38	5
Na_{98}	0.96	5
Na_{198}	0.66	5
Na_{20}	1.20	6
Na_{19}^{-}	0.90	6
Na_{40}	0.90	6

References

1. Schaaff, T.G.[152] 3. Khoury, J.T.[151] 5. Eckardt[143]

2. Palpant,B.[144] 4. Serra, L[145] 6.Rubio,A[148]

CHAPTER IX

NANOCRYSTAL SIZE DETERMINATION BY MASS SPECTROMETRY AND SCANNING TUNNELING MICROSCOPY

Scanning tunneling spectroscopy (STS) and microscopy (STM) have been used to study the electronic structure of small (<2 nm diameter) alkanethiol-passivated gold nanocrystals. The nanocrystals were prepared via chemical methods, and their mass distribution was characterized by time-of-flight mass spectrometry. STM/STS measurements were done at room temperature, 77 K, and 8 K, with isolated nanocrystals immobilized on Au(111) surfaces by a xylenedithiol self-assembled monolayer (SAM). A histogram of nanocrystal heights measured by STM shows several peaks. These correlate well with distinct peaks in the mass spectrum. STS dI/dV spectra vary with nanocrystal size, and show prominent features due to their quantized density-of-states. Spectra acquired repeatedly over a single nanocrystal evolve in time slowly, possibly due to configurational changes of the nanocrystal or its passivation layer.

9.1 Introduction

Metallic (gold) nanocrystals (NXLs) of diameter ≤ 3 nm fall into a critical regime for nanoscience and engineering[161,162]. In this size range, the single-electron Coulomb charging energy is large enough (~0.1–1 eV) that useful electronic devices (e.g. the "single-electron transistor") might be constructed, and the spacing between discrete molecular-like energy states is comparable to *kT* at room temperature. Gold particles in this size range have also shown remarkable catalytic activity.[163] Perhaps most importantly in the long run, nanocrystal molecular solids may form a basis for the *design* of functional materials.[135]

9.2 Results and Discussion

Hexanethiol-encapsulated gold nanocrystals were prepared chemically using established techniques.[162] For this work, the gold nanocrystals were not separated by Au-core size. The mixture of nanocrystal products, which are formed by reducing an Au(I)SR polymer, were characterized by laser desorption ionization mass spectrometry (LDI-MS). Films for LDI-MS were prepared by drying concentrated solutions of nanocrystals on a stainless steel plate. Mass spectra (such as that in Figure 9-1) were generated by irradiating neat films on stainless steel with frequency tripled Nd:YAG laser (355nm).

Distinct, broad peaks are observed in the mass spectrum, corresponding to a family of stable nanocrystal sizes that have been studied extensively (after mass separation).[164] From comparison of mass spectra and other independent measures of the nanocrystal core size and mass[165], it has been determined that the low-mass onset of the

peak provides a good approximation for the core mass (i.e. the number of gold atoms) for each of the nanocrystals. For example, the spectra in Figure 9-1 is indicative of a mixture containing nanocrystals produced via the reduction method discussed above. In addition, from gravimetric analyses of separated fractions, the amplitude of the peaks in the mass spectrum is roughly proportional to the relative abundance of each nanocrystal in the mixture [?].

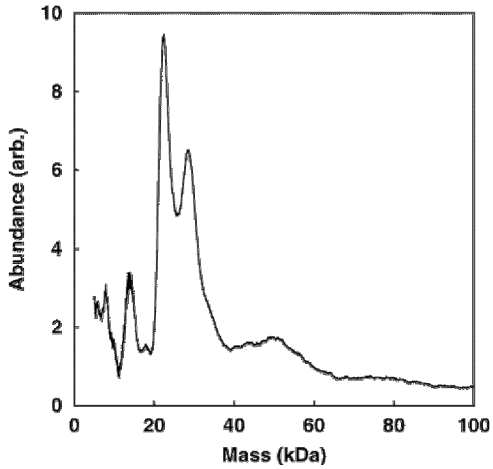

Figure 9-1. Laser desorption ionization mass spectrum obtained from a preparation of hexanethiol-capped gold nanocrystals formed by reduction of a Au(I)SR polymer. Note that the high mass peaks (over ~40k) include contributions from laser-induced coalescence of the more abundant low-mass nanocrystals.

Nanocrystal samples for STM measurement were prepared as described by Harrell et al.[166] Briefly, Au(111) films were grown on heated mica substrates by vapor deposition with subsequent sputter cleaning and annealing. [[With minimal exposure to atmosphere, substrates were then transferred into a solution of dithiol molecules [1 mM 1,4-benzenedimethanethiol (BDMT) in tetrahydrofuran (THF)] and allowed to soak for 1

hour. A THF rinse removed excess thiols, after which the substrates were allowed to dry.] STM topographs of the resulting SAM show many depressions, 0.1-0.2 nm deep. Previous surface-enhanced Raman measurements of BDMT/Au(111) SAMs have shown that the BDMT molecules align along the surface normal at room temperature, but near their desorption temperature (423 K) it is believed that another phase is present where both thiol groups bind to the substrate, so that the molecule is roughly parallel to the surface plane.[167,168] It is possible that the depressions found by STM are due to small regions where the BDMT has bound parallel to the surface, even at room temperature. The parallel orientation is known to occur at room temperature for BDMT/Ag(111).[167,168]

After formation of the SAM, nanocrystals from a mass-characterized preparation were dissolved in toluene (typically 1 μM) and deposited using a micropipette (typically 5 μL). Deposition was followed by a rinse in flowing toluene solvent to remove the most loosely-bound nanocrystals. Samples were imaged under high vacuum or ultrahigh vacuum conditions (10^{-8} –10^{-10} mbar) in a room temperature STM system[169] or a cryogenic.[166] No further treatment or surface cleaning was done once the samples were under vacuum.

Figure 9-2 shows a room-temperature STM topograph of gold nanocrystals on Au(111) acquired at a constant current of 100 pA using a tip potential of -1.00 V with respect to the substrate. Several different nanocrystal sizes are apparent in the image. The nanocrystal coverage shown in the image was fairly typical of this sample, although some regions were found where large monolayer islands of nanocrystals had formed. These seemed to deplete the surface coverage in much of the surrounding area, although many single nanocrystals could be found close to the islands.

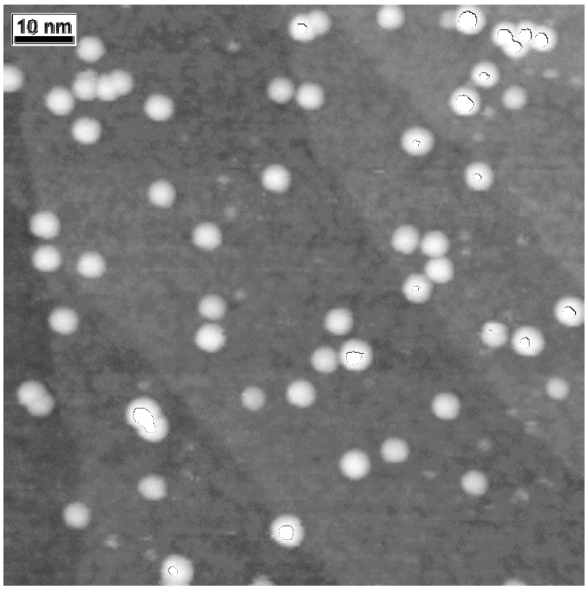

Figure 9-2. Room-temperature topographic image of mixed-size nanocrystals, 100 nm x 100 nm. Size differences are seen in both the apparent diameters and the heights. Surface height is displayed on a grey scale that spans 2.5 nm. (Tip voltage = -1.00 V, tunnel current = 100 pA.)

In order to quantify the size distribution of nanocrystals on the surface, heights were determined from profiles across the nanocrystal centers. The maximum height should be a better measure of nanocrystal diameter than the perceived width, since it is unaffected by details of the tip shape. Only regions similar to that pictured in figure 9-2 were used for the analysis (i.e. no nanocrystal islands) since it was necessary to image the substrate nearby the nanocrystal for accurate measurement. Heights were always referenced to the lowest point on the SAM adjacent to the nanocrystal. Figure 9-3 shows a histogram of the observed abundance of different heights for 221 measured nanocrystals. Remarkably, the histogram shows distinct peaks in the height distribution, which would remain even considering $\sqrt{N}$ statistical fluctuations.

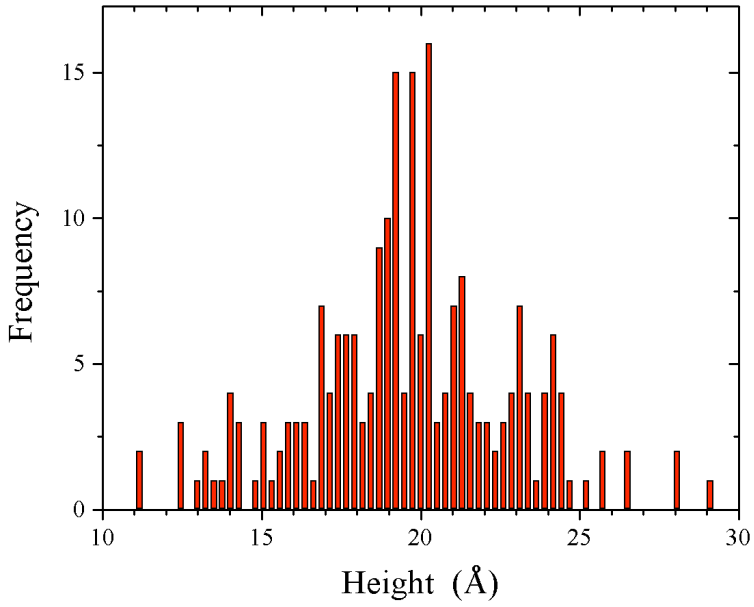

Figure 9-3. Histogram of heights measured from STM profiles across 221 individual nanocrystals. A bin width of 0.028 nm was used.

We can associate these peaks with the stable nanocrystal masses seen in the LDI-MS spectrum of Figure 9-1. The correlation between measured STM heights and nanocrystal masses is made clear in Figure 9-4.

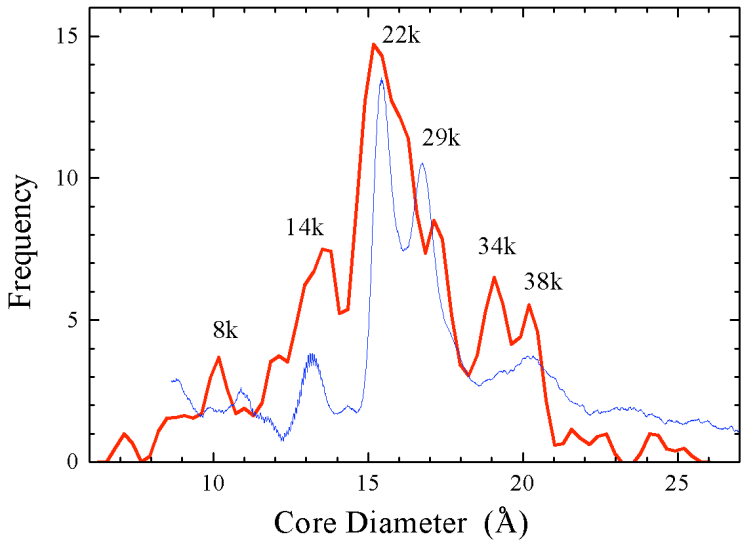

Figure 9-4. Blue line: Time-of-flight mass spectrum of a "raw" NXL preparation. Abundance is plotted versus effective core diameter, derived from the measured masses assuming a spherical particle. Preparation and mass spectrometry were done at Oak Ridge National Lab. Red line: Histogram of measured STM heights from the same NXL preparation. The histogram (represented by a continuous line) has been shifted by approximately +0.4 nm in order to align it with the mass spectrum.

Here the LDI-MS spectrum has been plotted versus effective nanocrystal diameter, using a spherical approximation and bulk density for the gold particles ($D[nm]=5.48\text{x}10^{-2}(M[kDa])^{1/3}$). At the onset of each mass peak, this should provide a fairly accurate measure of the gold core diameter.[162] The STM height histogram has been shifted -0.360 nm so as to align the major peaks in the two spectra. After shifting, the correspondence of peak positions is very good, and the relative abundances are seen to be similar in both measurements. This is an encouraging result with several implications: 1) The nanocrystal cores must have been essentially un-deformed from their prepared state. 2) The adsorption of nanocrystals was not size-dependent for masses from 8 k to

55 k. 3) Under the chosen measurement conditions, the hexanethiol passivation was not deformed by the STM (or the deformation was similar for different nanocrystals). 4) The measurement method sufficiently accounted for intrinsic 0.1-nm depressions in the SAM. 5) Height variations due to different adsorption geometries or various nanocrystal orientations were relatively small. Undoubtedly, each of these effects still contributes to the detailed shapes of the histogram peaks, but better counting statistics will be required to determine the possible influence of each.

In Figure 9-4, the height histogram was shifted to best represent the correlation with relative abundance peaks in the mass spectrum. However, the nanocrystal core mass (and mass-derived core diameter) should be obtained from the leading edge of the LDI-MS peak.[164] Making this association gives a difference of 0.385 nm between the most abundant nanocrystal height measured by STM and its mass-derived core diameter. The STM heights clearly should be larger than the LDI-MS core diameter due to the adsorbed passivation layer, but the observed difference is smaller than would be expected if the hexane chains were in the vertical alignment normally found for hexanethiol SAMs on the Au(111) surface.[170,171] The difference could be a consequence of at least three likely effects: interpenetration of the nanocrystal passivation layer and the BDMT SAM, preferential binding of the nanocrystals within depressions in the SAM (obscuring the depressed area), and the formation of a disordered but compact configuration of the hexanethiol passivation layer.[172]

Besides the physical implications listed above, the height-mass correlation shown here will be very valuable for STM experiments. It will now be possible to study size-dependent electronic properties without changing the tunneling conditions (as would

typically occur if one had to switch samples entirely), while maintaining the ability to label each nanocrystal with a size known to within a few atoms. In Figure 9-4 the abundance peaks are labeled with several stable masses that have been isolated in other work .[162,164]

Tunneling spectra taken over individual nanocrystals displays size dependent behavior as well and may assist in size determination. As an example of this ability, Figure 9-5 shows a room-temperature image and accompanying spectra that were acquired over nanocrystals of varying masses. In these spectra, the voltage gap is observed to increase with decreasing nanocrystal size, as one would expect for both single-electron charging and quantum confinement effects.

Analysis of preliminary measurements shows that the size-dependence of the gap is proportional to at least $N^{-2/3}$ (i.e. radius^{-2} or higher power), much stronger than the $N^{-1/3}$ scaling of an isolated classical metallic sphere. Deviations from this simple model can be attributed partly to the geometry of the experiment, but this alone is inadequate to explain the observed scaling.

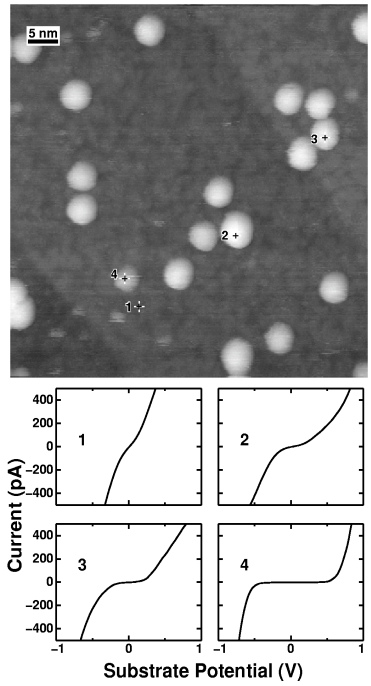

Figure 9-5. Room-temperature image (color represents surface gradient) and simultaneously-acquired tunneling spectra over nanocrystals of various sizes. Spectrum 1 is over the SAM, while spectra 2–4 are from nanocrystals of mass 38 k, 26 k, and 6 k, respectively, as determined from the measured height-mass correlation.

In Figure 9-5, the NXL sizes are labeled by *mass*. This identification was made possible by correlating heights measured in the STM with NXL mean core diameters as determined by time-of-flight mass spectroscopy (core diameter μ mass$^{1/3}$) on the same raw NXL preparation. Figure 9-4 shows that both distributions have distinct peaks (stable or "magic" sizes) that are well-correlated after the STM height distribution is shifted by ~0.4 nm. This shift results from some interpenetration of the NXL monolayer and the SAM binding layer.[173]

9.3 Conclusion

We have shown that gold nanocrystals of different masses can be positively identified in scanning tunneling microscopy experiments by comparing the height distribution measured by STM with the core size distribution measured directly by mass spectrometry. A histogram of nanocrystal heights revealed several peaks that correlate well with distinct peaks in the mass spectrum. This establishes a mapping between STM height and nanocrystal core diameter or core mass. The map will enable the compilation of single molecule spectra for each nanocrystal species and will facilitate comparisons to ensemble measurements.

REFERENCES

(1) Somorjai, G. A. *Journal of Physical Chemistry* **1990**, *94*, 1013-23.

(2) Campbell, I. M. *Catalysis of Surfaces*, 1988.

(3) Ertl, G.; Knoezinger, H.; Editors *Handbook of Heterogeneous Catalysis, 5 Volume Set*, 1997.

(4) Kaldor, A.; Cox, D. M.; Trevor, D. J.; Zakin, M. R. *Zeitschrift fuer Physik D: Atoms, Molecules and Clusters* **1986**, *3*, 195-204.

(5) Boreskov, G. K.; Polyakova, G. M.; Ivanov, A. A.; Mastikhin, V. M. *Doklady Akademii Nauk SSSR* **1973**, *210*, 626-9 [Phys Chem].

(6) Boreskov, G. K.; Ivanov, A. A.; Balzhinimaev, B. S.; Karnatovskaya, L. M. *Reaction Kinetics and Catalysis Letters* **1980**, *14*, 25-9.

(7) Doering, F. J.; Berkel, D. A. *Journal of Catalysis* **1987**, *103*, 126-39.

(8) Lapina, O. B.; Bal'zhinimaev, B. S.; Boghosian, S.; Eriksen, K. M.; Fehrmann, R. *Catalysis Today* **1999**, *51*, 469-479.

(9) In *Chemical & Engineering News*, 2004; Vol. 82.

(10) Rasmussen, S. B., Technical University of Denmark, 2001.

(11) Schlogl, R. *Handbook of Heterogenous Catalysis, Vol. 1*; VCH: Weinheim, 1997.

(12) Eriksen, K. M.; Karydis, D. A.; Boghosian, S.; Fehrmann, R. *Journal of Catalysis* **1995**, *155*, 32-42.

(13) Rasmussen, S. B.; Boghosian, S.; Nielsen, K.; Eriksen, K. M.; Fehrmann, R. *Inorganic Chemistry*, ACS ASAP.

(14) Wachs, I. E.; Briand, L. E.; Jehng, J. M.; Burcham, L.; Gao, X. *Catalysis Today* **2000**, *57*, 323-330.

(15) Cox, D. M.; Brickman, R.; Creegan, K.; Kaldor, A. *Zeitschrift fuer Physik D: Atoms, Molecules and Clusters* **1991**, *19*, 353-5.

(16) Somorjai, G. A. *Introduction to Surface Chemistry and Catalysis*; John Wiley and Sons: New York, 1994.

(17) Witko, M. *Catalysis Today* **1996**, *32*, 89-95.

(18) Zemski, K. A.; Justes, D. R.; Castleman, A. W., Jr. *Journal of Physical Chemistry B* **2002**, *106*, 6136-6148.

(19) Zemski, K. A.; Bell, R. C.; Castleman, A. W., Jr. *Clusters and Nanostructure Interfaces, [Proceedings of the International Symposium on Clusters and Nanostructure Interfaces], Richmond, VA, United States, Oct. 25-28, 1999* **2000**, 535-544.

(20) Zemski, K. A.; Bell, R. C.; Justes, D. R.; Castleman, A. W., Jr. *Physics and Chemistry of Clusters, Proceedings of Nobel Symposium, 117th, Visby, Sweden, June 27-July 2, 2000* **2001**, 290-291.

(21) Rudnyi, E. B.; Kaibicheva, E. A.; Sidorov, L. N. *Journal of Chemical Thermodynamics* **1993**, *25*, 929-47.

(22) Dinca, A.; Davis, T. P.; Fisher, K. J.; Smith, D. R.; Willett, G. D. *International Journal of Mass Spectrometry* **1999**, *182/183*, 73-84.

(23) Foltin, M.; Stueber, G. J.; Bernstein, E. R. *Journal of Chemical Physics* **1999**, *111*, 9577-9586.

(24) Zhai, H.-J.; Wang, L.-S. *Journal of Chemical Physics* **2002**, *117*, 7882-7888.

(25) Wu, H.; Wang, L.-S. *Journal of Chemical Physics* **1998**, *108*, 5310-5318.

(26) Wu, H.; Wang, L.-S. *Journal of Chemical Physics* **1997**, *107*, 16-21.

(27) Wu, H.; Wang, L.-S. *Journal of Chemical Physics* **1997**, *107*, 8221-8228.

(28) Chertihin, G. V.; Bare, W. D.; Andrews, L. *Journal of Physical Chemistry A* **1997**, *101*, 5090-5096.

(29) Hou, D.; Hagen, K. S.; Hill, C. L. *Journal of the American Chemical Society* **1992**, *114*, 5864-6.

(30) Hou, D.; Hagen, K. S.; Hill, C. L. *Journal of the Chemical Society, Chemical Communications* **1993**, 426-8.

(31) Hou, D.; Kim, G.-S.; Hagen, K. S.; Hill, C. L. *Inorganica Chimica Acta* **1993**, *211*, 127-30.

(32) Weinstock, I. A. *Chemical Reviews (Washington, D. C.)* **1998**, *98*, 113-170.

(33) Walanda, D. K.; Burns, R. C.; Lawrance, G. A.; von Nagy-Felsobuki, E. I. *Inorganica Chimica Acta* **2000**, *305*, 118-126.

(34) Walanda, D. K.; Burns, R. C.; Lawrance, G. A.; Von Nagy-Felsobuki, E. I. *Inorganic Chemistry Communications* **1999**, *2*, 487-489.

(35) Hamilton, E. E.; Fanwick, P. E.; Wilker, J. J. *Journal of the American Chemical Society* **2002**, *124*, 78-82.

(36) Day, V. W.; Klemperer, W. G.; Yaghi, O. M. *Journal of the American Chemical Society* **1989**, *111*, 4518-19.

(37) Day, V. W.; Klemperer, W. G.; Yaghi, O. M. *Journal of the American Chemical Society* **1989**, *111*, 5959-61.

(38) Day, V. W.; Klemperer, W. G.; Yagasaki, A. *Chemistry Letters* **1990**, 1267-70.

(39) Vyboishchikov, S. F.; Sauer, J. *Journal of Physical Chemistry A* **2001**, *105*, 8588-8598.

(40) Vyboishchikov, S. F.; Sauer, J. *Journal of Physical Chemistry A* **2000**, *104*, 10913-10922.

(41) Parks, E. K.; Nieman, G. C.; Kerns, K. P.; Riley, S. J. *J. Chem. Phys.* **1998**, *108*, 3731-3739.

(42) Finlayson-Pitts, B. J.; Pitts, J. N. *Chemistry of the upper and lower atmosphere*; Academic Press: New York, 2000.

(43) Whetten, R. L.; Schriver, K. E. In *Gas Phase Inorganic Chemistry*; Russell, D. H., Ed.; Plenum Press: New York, 1989.

(44) Jarrold, M. F. In *Gas Phase Inorganic Chemistry*; Russell, D. H., Ed.; Plenum Press: New York, 1989.

(45) Kaldor, A.; Cox, D. M.; Zakin, M. R. In *Part 2 Advances in Chemical Dynamics*; Prigogine, I., Rice, S. A., Eds.; John Wiley and Sons: New York, 1988; Vol. LXX.

(46) Mark, T. D.; Castleman, A. W., Jr. *Advanced Atomic Molecular Physics* **1985**, *20*, 65.

(47) Riley, S. J.; Parks, E. K. *NATO ASI Series, Series B: Physics* **1987**, *158*, 727-39.

(48) Dietz, T. G.; Duncan, M. A.; Powers, D. E.; Smalley, R. E. *Journal of Chemical Physics* **1981**, *74*, 6511-12.

(49) Bell, R. C.; Zemski, K. A.; Justes, D. R.; Castleman, A. W., Jr. *Journal of Chemical Physics* **2001**, *114*, 798-811.

(50) Woenckhaus, J.; Becker, J. A. *Review of Scientific Instruments* **1994**, *65*, 2019-22.

(51) Wiley, W. C.; McLaren, I. H. *Rev. Sci. Instr.* **1955**, *26*, 1150-1159.

(52) Cotter, R. J. *Time-of-Flight Mass Spectrometry: Instrumentation and Applications in Biological Research*, 1997.

(53) Cotter, R. J.; Editor *Time-of-Flight Mass Spectrometry: Instrumentation and Applications in Biological Research*, 1997.

(54) Justes, D. R.; Castleman, A. W., Jr.; Mitric, R.; Bonacic-Koutecky, V. *European Physical Journal D: Atomic, Molecular and Optical Physics* **2003**, *24*, 331-334.

(55) Whetten, R. L. *Materials Science & Engineering, B: Solid-State Materials for Advanced Technology* **1993**, *B19*, 8-13.

(56) Tenne, R.; Homyonfer, M.; Feldman, Y. *Chemistry of Materials* **1998**, *10*, 3225-3238.

(57) Guo, B. C.; Kerns, K. P.; Castleman, A. W., Jr. *Science (Washington, DC, United States)* **1992**, *255*, 1411-13.

(58) Adams, G. B.; Sankey, O. F.; Page, J. B.; O'Keeffe, M.; Drabold, D. A. *Science (Washington, DC, United States)* **1992**, *256*, 1792-5.

(59) Beckhaus, H. D.; Ruechardt, C.; Kao, M.; Diederich, F.; Foote, C. S. *Angewandte Chemie* **1992**, *104*, 69-70 (See also Angew Chem , Int Ed Engl , 1992, 31(1), 63-4).

(60) Stanton, R. E. *Journal of Physical Chemistry* **1992**, *96*, 111-18.

(61) Zhang, B. L.; Wang, C. Z.; Ho, K. M. *Chemical Physics Letters* **1992**, *193*, 225-30.

(62) St.John, P. M.; Yeretzian, C.; Whetten, R. L. *J. Phys. Chem.* **1992**, *96*, 9100-9104.

(63) Boldyrev, A. I.; Simons, J. *Journal of the American Chemical Society* **1997**, *119*, 4618-4621.

(64) Klemperer, W. G.; Marquart, T. A.; Yaghi, O. M. *Angewandte Chemie* **1992**, *104*, 51-3 (See also Angew Chem , Int Ed Engl , 1992, 31(1), 49-51).

(65) Cai, T.; Chen, Z.; Wang, X.; Li, L.; Lu, J. *Progress in Natural Science* **1997**, *7*, 554-561.

(66) Hill, C. L.; White, G. C. *Chemical Reviews (Washington, D. C.)* **1998**, *98*, 1-2.

(67) Salisbury, B. E.; Wallace, W. T.; Whetten, R. L. *Chem. Phys.* **2000**, *262*, 131-141.

(68) Johnson, J. R. T.; Panas, I. *Inorganic Chemistry* **2000**, *39*, 3181-3191.

(69) Lee, T. H.; Ervin, K. M. *Journal of Physical Chemistry* **1994**, *98*, 10023-31.

(70) Cox, D. M.; Reichmann, K. C.; Trevor, D. J.; Kaldor, A. *Journal of Chemical Physics* **1988**, *88*, 111-19.

(71) Crans, D. C.; Smee, J. J.; Gaidamauskas, E.; Yang, L. *Chemical Reviews (Washington, DC, United States)* **2004**, *104*, 849-902.

(72) Calatayud, M.; Silvi, B.; Andres, J.; Beltran, A. *Chemical Physics Letters* **2001**, *333*, 493-503.

(73) Calatayud, M.; Andres, J.; Beltran, A.; Silvi, B. *Theoretical Chemistry Accounts* **2001**, *105*, 299-308.

(74) Broclawik, E.; Haber, J.; Piskorz, W. *Chemical Physics Letters* **2001**, *333*, 332-336.

(75) Bakalbassis, E. G.; Stiakaki, M.-A. D.; Tsipis, A. C.; Tsipis, C. A. *Chemical Physics* **1996**, *205*, 389-399.

(76) Gutsev, G. L.; Rao, B. K.; Jena, P. *Journal of Physical Chemistry A* **2000**, *104*, 11961-11971.

(77) Gutsev, G. L.; Rao, B. K.; Jena, P. *Journal of Physical Chemistry A* **2000**, *104*, 5374-5379.

(78) Knight, L. B., Jr.; Babb, R.; Ray, M.; Banisaukas, T. J., III; Russon, L.; Dailey, R. S.; Davidson, E. R. *Journal of Chemical Physics* **1996**, *105*, 10237-10250.

(79) Fielicke, A.; Rademann, K. *Physical Chemistry Chemical Physics* **2002**, *4*, 2621-2628.

(80) Bell, R. C.; Zemski, K. A.; Kerns, K. P.; Deng, H. T.; Castleman, A. W., Jr. *Journal of Physical Chemistry A* **1998**, *102*, 1733-1742.

(81) Kong, J.; White, C. A.; Krylov, A. I.; Sherrill, D.; Adamson, R. D.; Furlani, T. R.; Lee, M. S.; Lee, A. M.; Gwaltney, S. R.; Adams, T. R.; Ochsenfeld, C.; Gilbert, A. T. B.; Kedziora, G. S.; Rassolov, V. A.; Maurice, D. R.; Nair, N.; Shao, Y.; Besley, N. A.; Maslen, P. E.; Dombroski, J. P.; Daschel, H.; Zhang, W.; Korambath, P. P.; Baker, J.; Byrd, E. F. C.; Van Voorhis, T.; Oumi, M.; Hirata, S.; Hsu, C.-P.; Ishikawa, N.; Florian, J.; Warshel, A.; Johnson, B. G.; Gill, P. M. W.; Head-Gordon, M.; Pople, J. A. *Journal of Computational Chemistry* **2000**, *21*, 1532-1548.

(82) Becke, A. D. *Physical Review A: Atomic, Molecular, and Optical Physics* **1988**, *38*, 3098-100.

(83) Becke, A. D. *J. Chem. Phys.* **1993**, *98*, 5648.

(84) Lee, C.; Yang, W.; Parr, R. G. *Physical Review B: Condensed Matter and Materials Physics* **1988**, *37*, 785-9.

(85) Schaefer, A.; Huber, C.; Ahlrichs, R. *Journal of Chemical Physics* **1994**, *100*, 5829-35.

(86) Bell, R. C.; Zemski, K. A.; Castleman, A. W., Jr. *Journal of Cluster Science* **1999**, *10*, 509-524.

(87) Froeberg, T.; Johansen, H. *Acta Chemica Scandinavica* **1996**, *50*, 961-966.

(88) Nielsen, K.; Fehrmann, R.; Eriksen, K. M. *Inorganic Chemistry* **1993**, *32*, 4825-8.

(89) Rustad, J. R.; Dixon, D. A.; Kubicki, J. D.; Felmy, A. R. *Journal of Physical Chemistry A* **2000**, *104*, 4051-4057.

(90) Chughtai, A. R.; Atteya, M. M. O.; Kim, J.; Konowalchuk, B. K.; Smith, D. M. *Carbon* **1998**, *36*, 1573-1589.

(91) Grassian, V. H. *Journal of Physical Chemistry A* **2002**, *106*, 860-877.

(92) Pope, C. A., III; Burnett, R. T.; Thun, M. J.; Calle, E. E.; Krewski, D.; Ito, K.; Thurston, G. D. *JAMA, the Journal of the American Medical Association* **2002**, *287*, 1132-1141.

(93) Posfai, M.; Anderson, J. R.; Buseck, P. R.; Sievering, H. *Journal of Geophysical Research, [Atmospheres]* **1999**, *104*, 21685-21693.

(94) Novakov, T.; Chang, S. G.; Harker, A. B. *Science (Washington, DC, United States)* **1974**, *186*, 259-61.

(95) Fahey, D. W.; Keim, E. R.; Boering, K. A.; Brock, C. A.; Wilson, J. C.; Jonsson, H. H.; Anthony, S.; Hanisco, T. F.; Wennberg, P. O.; et al. *Science (Washington, D. C.)* **1995**, *270*, 70-4.

(96) Schumann, U.; Stroem, J.; Busen, R.; Baumann, R.; Gierens, K.; Krautstrunk, M.; Schroeder, F. P.; Stingl, J. *Journal of Geophysical Research, [Atmospheres]* **1996**, *101*, 6853-6869.

(97) Koehler, B. G.; Nicholson, V. T.; Roe, H. G.; Whitney, E. S. *Jounal of Geophysical Research* **1999**, *104*, 5507.

(98) Hayes, A. J.; Wine, P. H. *Gas-Phase Combustion Chemistry*; Springer-Verlag: New York, 2000.

(99) Humeres, E.; Peruch, M. d. G. B.; Moreira, R. F. P. M.; Schreiner, W. *Journal of Physical Organic Chemistry* **2003**, *16*, 824-830.

(100) Gerhardt, P.; Loeffler, S.; Homann, K. H. *Chemical Physics Letters* **1987**, *137*, 306-10.

(101) Higgins, K. J.; Jung, H.; Kittelson, D. B.; Roberts, J. T.; Zachariah, M. R. *Journal of Physical Chemistry A* **2002**, *106*, 96-103.

(102) Dugourd, P.; Hudgins, R. R.; Tenenbaum, J. M.; Jarrold, M. F. *Physical Review Letters* **1998**, *80*, 4197-4200.

(103) Maier, J. P. *Journal of Physical Chemistry A* **1998**, *102*, 3462-3469.

(104) Kohno, M.; Suzuki, S.; Shiromaru, H.; Moriwaki, T.; Achiba, Y. *Chemical Physics Letters* **1998**, *282*, 330-334.

(105) Zhang, Q. L.; O'Brien, S. C.; Heath, J. R.; Liu, Y.; Curl, R. F.; Kroto, H. W.; Smalley, R. E. *Journal of Physical Chemistry* **1986**, *90*, 525-8.

(106) Zimmerman, J. A.; Eyler, J. R.; Bach, S. B. H.; McElvany, S. W. *Journal of Chemical Physics* **1991**, *94*, 3556-62.

(107) McElvany, S. W.; Dunlap, B. I.; O'Keefe, A. *Journal of Chemical Physics* **1987**, *86*, 715-25.

(108) Fisher, K.; Hopwood, F.; Dance, I.; Willett, G. *New Journal of Chemistry* **1999**, *23*, 609-616.

(109) Knickelbein, M. B. *Annual Review of Physical Chemistry* **1999**, *50*, 79-115.

(110) Wallace, W. T.; Whetten, R. L. *European Physical Journal D: Atomic, Molecular and Optical Physics* **2001**, *16*, 123-126.

(111) Gotts, N. G.; von Helden, G.; Bowers, M. T. *International Journal of Mass Spectrometry and Ion Processes* **1995**, *149/150*, 217-29.

(112) Moehler, O.; Reiner, T.; Arnold, F. *Journal of Chemical Physics* **1992**, *97*, 8233-9.

(113) Wang, X.-B.; Nicholas, J. B.; Wang, L.-S. *Journal of Physical Chemistry A* **2000**, *104*, 504-508.

(114) Zemski, K. A.; Justes, D. R.; Castleman, A. W., Jr. *Journal of Physical Chemistry A* **2001**, *105*, 10237-10245.

(115) Justes, D. R.; Moore, N. A.; Castleman, A. W., Jr. *Journal of Physical Chemistry B* **2004**, *108*, 3855-3862.

(116) Bell, R. C.; Zemski, K. A.; Castleman, A. W., Jr. *Journal of Physical Chemistry A* **1999**, *103*, 1585-1591.

(117) Bell, R. C.; Zemski, K. A.; Castleman, A. W., Jr. *Journal of Physical Chemistry A* **1999**, *103*, 2992-2998.

(118) Bell, R. C.; Zemski, K. A.; Castleman, A. W., Jr. *Journal of Physical Chemistry A* **1998**, *102*, 8293-8299.

(119) Bell, R. C.; Castleman, A. W., Jr.; Thorn, D. L. *Inorganic Chemistry* **1999**, *38*, 5709-5715.

(120) Bell, R. C.; Castleman, A. W., Jr. *Journal of Physical Chemistry A* **2002**, *106*, 9893-9899.

(121) Kerns, K. P.; Guo, B. C.; Deng, H. T.; Castleman, A. W., Jr. *Journal of Chemical Physics* **1994**, *101*, 8529-34.

(122) Sun, Q.; Rao, B. K.; Jena, P.; Stolcic, D.; Kim, Y. D.; Gantefoer, G.; Castleman, A. W., Jr. *Journal of Chemical Physics* **2004**, *accepted*.

(123) Zemski, K. A.; Justes, D. R.; Bell, R. C.; Castleman, A. W., Jr. *Journal of Physical Chemistry A* **2001**, *105*, 4410-4417.

(124) Zemski, K. A.; Bell, R. C.; Castleman, A. W., Jr. *Journal of Physical Chemistry A* **2000**, *104*, 5732-5741.

(125) Zemski, K. A.; Bell, R. C.; Castleman, A. W., Jr. *Journal of Physical Chemistry A* **2000**, *104*, 7408.

(126) Salisbury, B. E. Ph.D. Thesis, Georgia Institute of Technology, 1999.

(127) Livingston, F. E. Ph.D., University of California, 1995.

(128) Keesee, R. G.; Castleman, A. W., Jr. *Chemical Physics Letters* **1980**, *74*, 139-42.

(129) Faraday, M. *Proc. Royal Chem. Soc.* **1856-1857**, *8*, 356-361.

(130) Goodman, D. W. *Journal of Catalysis* **2003**, *216*, 213-222.

(131) Hainfeld, J. F.; Furuya, F. R. *J. Histochem. Cytochem.* **1992**, *40*, 177-184.

(132) Elghanian, R.; Storhoff, J. J.; Mucic, R. C.; Letsinger, R. L.; Mirkin, C. A. *Science (Washington, D. C.)* **1997**, *277*, 1078-1080.

(133) Landman, U.; Luedtke, W. D.; Salisbury, B. E.; Whetten, R. L. *Physical Review Letters* **1996**, *77*, 1362-1365.

(134) Gittins, D. I.; Bethell, D.; Schiffrin, D. J.; Nichols, R. J. *Nature* **2000**, *408*, 67-9.

(135) Alivisatos, A. P. *Science (Washington, D. C.)* **1996**, *271*, 933-7.

(136) Lezec, H. J.; Degiron, A.; Devaux, E.; Linke, R. A.; Martin-Moreno, L.; Garcia-Vidal, F. J.; Ebbesen, T. W. *Science* **2002**, *297*, 820-2.

(137) Dickson, R. M.; Lyon, L. A. *Journal of Physical Chemistry B* **2000**, *104*, 6095-6098.

(138) Michaels, A. M.; Jiang, J.; Brus, L. *Journal of Physical Chemistry B* **2000**, *104*, 11965-11971.

(139) Bigioni, T. P.; Whetten, R. L.; Dag, O. *Journal of Physical Chemistry B* **2000**, *104*, 6983-6986.

(140) Link, S.; Beeby, A.; FitzGerald, S.; El-Sayed, M. A.; Schaaff, T. G.; Whetten, R. L. *Journal of Physical Chemistry B* **2002**, *106*, 3410-3415.

(141) Mie, G. *Annalen der Physik (Weinheim, Germany)* **1908**, *25*, 377-445.

(142) Kreibig, U.; Vollmer, M. *Optical properties of metal clusters*; Springer: Berlin, 1995.

(143) Ekardt, W. *Physical Review B: Condensed Matter and Materials Physics* **1985**, *31*, 6360-70.

(144) Lerme, J.; Palpant, B.; Prevel, B.; Cottancin, E.; Pellarin, M.; Treilleux, M.; Vialle, J. L.; Perez, A.; Broyer, M. *European Physical Journal D: Atomic, Molecular and Optical Physics* **1998**, *4*, 95-108.

(145) Lerme, J.; Palpant, B.; Prevel, B.; Pellarin, M.; Treilleux, M.; Vialle, J. L.; Perez, A.; Broyer, M. *Physical Review Letters* **1998**, *80*, 5105-5108.

(146) Moskovitz, M. Proc. Internat. School Phys. "Enrico Fermi", The Chemical Physics of Atomic and Molecular Clusters, 1990; p 397.

(147) Paggel, J.; Miller, T.; Chiang, T. C. *Science (Washington, D. C.)* **1999**, *283*, 1709-1711.

(148) Rubio, A.; Balbas, L. C.; Alonso, J. A. *Physical Review B: Condensed Matter and Materials Physics* **1992**, *46*, 4891-8.

(149) deHeer, W. A. *Rev. Mod. Phys.* **1993**, *65*, 611-676.

(150) Alvarez, M. M.; Khoury, J. T.; Schaaff, T. G.; Shafigullin, M. N.; Vezmar, I.; Whetten, R. L. *J. Phys. Chem. B* **1997**, *101*, 3706-3712.

(151) Khoury, J. T. Ph.D., University of California, LA, 1998.

(152) Schaaff, T. G. Ph.D. Thesis, Georgia Institute of Technology, 1998.

(153) Innes, R. A.; Sambles, J. R. *Journal of Physics F: Metal Physics* **1987**, *17*, 277-87.

(154) Ehrenreich, H.; Philipp, H. R. *Physical Review* **1962**, *128*, 1622-9.

(155) Zaitoun, M. A.; Mason, W. R.; Lin, C. T. *Journal of Physical Chemistry B* **2001**, *105*, 6780-6784.

(156) Wang, Y.; Herron, N. *Research on Chemical Intermediates* **1991**, *15*, 17-29.

(157) Zheng, J.; Petty, J. T.; Dickson, R. M. *Journal of the American Chemical Society* **2003**, *125*, 7780-7781.

(158) Negishi, Y.; Takasugi, Y.; Sato, S.; Yao, H.; Kimura, K.; Tsukuda, T. *Journal of the American Chemical Society* **2004**, *126*, 6518-6519.

(159) Kittel, C. *Introduction to Solid State Physics*; Wiley: New York, 1996.

(160) Ashcroft, N. W.; Mermin, N. D. *Solid State Physics*; Saunders College: Philadelphia, 1976.

(161) Whetten, R. L.; Khoury, J. T.; Alvarez, M. M.; Murthy, S.; Vezmar, I.; Wang, Z. L.; Stephens, P. W.; Cleveland, C. L.; Luedtke, W. D.; Landman, U. *Advanced Materials (Weinheim, Germany)* **1996**, *8*, 428-33.

(162) Schaaff, T. G.; Shafigullin, M. N.; Khoury, J. T.; Vezmar, I.; Whetten, R. L.; Cullen, W. G.; First, P. N.; Wing, C.; Ascensio, J.; Yacaman, M. J. *Journal of Physical Chemistry B* **1997**, *101*, 7885-7891.

(163) Haruta, M.; Kobayashi, T.; Sano, H.; Yamada, N. *Chem. Lett.* **1987**, 405-408.

(164) Vezmar, I.; Alvarez, M. M.; Khoury, J. T.; Salisbury, B. E.; Shafigullin, M. N.; Whetten, R. L. *Zeitschrift fuer Physik D: Atoms, Molecules and Clusters* **1997**, *40*, 147-151.

(165) Schaaff, T. G. *Analytical Chemistry* **2004**, *76*, 6187-6196.

(166) Harrell, L. E.; Bigioni, T. P.; Cullen, W. G.; Whetten, R. L.; First, P. N. *Journal of Vacuum Science & Technology, B: Microelectronics and Nanometer Structures* **1999**, *17*, 2411-2416.

(167) Murty, K. V. G. K.; Venkataramanan, M.; Pradeep, T. *Langmuir* **1998**, *14*, 5446-5456.

(168) Venkataramanan, M.; Pradeep, T. *Analytical Chemistry* **2000**, *72*, 5852-5856.

(169) Quesenberry, P. E.; First, P. N. *Physical Review B: Condensed Matter* **1996**, *54*, 8218-8230.

(170) Poirier, G. E.; Tarlov, M. J. *Langmuir* **1994**, *10*, 2853-6.

(171) Poirier, G. E.; Pylant, E. D. *Science (Washington, D. C.)* **1996**, *272*, 1145-1148.

(172) Luedtke, W. D.; Landman, U. *Journal of Physical Chemistry* **1996**, *100*, 13323-13329.

(173) Bigioni, T. P.; Harrell, L. E.; Gullen, W. G.; Guthrie, D. K.; Whetten, R. L.; First, P. N. *European Physical Journal D: Atomic, Molecular and Optical Physics* **1999**, *6*, 355-364.